https://doi.org/10.15388/vu.thesis.807
https://orcid.org/0000-0002-4015-3517

VILNIUS UNIVERSITY
CENTER FOR PHYSICAL SCIENCES AND TECHNOLOGY

Aliona Klimovich

Surface-Enhanced Raman Spectroscopic Study of Adsorbed Biomolecules at Metal Surfaces

DOCTORAL DISSERTATION

Natural Sciences,
Chemistry (N 003)

VILNIUS 2025

The dissertation was prepared between 2020 and 2024 (State Research Institute Center for Physical Sciences and Technology). The research was supported by the Research Council of Lithuania.

Academic Supervisor – Dr. Ieva Matulaitienė (Center for Physical Sciences and Technology, Natural Sciences, Chemistry – N 003).

This doctoral dissertation will be defended in a public meeting of the Dissertation Defence Panel:

Chairman – **Prof. Dr. Justinas Čeponkus** (Vilnius University, Natural Sciences, Physics – N 002).

Members:
Assoc. Prof. Dr. Renata Butkutė (Center for Physical Sciences and Technology, Vilnius University, Natural Sciences, Physics – N 002),
Dr. Lina Mikoliūnaitė (Center for Physical Sciences and Technology, Natural Sciences, Chemistry – N 003),
Dr. Simonas Ramanavičius (Center for Physical Sciences and Technology, Natural Sciences, Physics – N 002),
Dr. Cordelia Zimmerer (Leibniz Institute of Polymer Research Dresden, Natural Sciences, Chemistry – N 003).

The dissertation shall be defended at a public meeting of the Dissertation Defence Panel at 15 h on the 15th of September 2025 in meeting room D401 of the Center for Physical Sciences and Technology.
Address: Sauletekio av. 3, Room D401, Vilnius, Lithuania
Tel. +370 52649211; e-mail:office@ftmc.lt

The text of this dissertation can be accessed at the libraries of Vilnius University, as well as on the website of Vilnius University: *www.vu.lt/lt/naujienos/ivykiu-kalendorius*

https://doi.org/10.15388/vu.thesis.807
https://orcid.org/0000-0002-4015-3517

VILNIAUS UNIVERSITETAS
FIZINIŲ IR TECHNOLOGIJOS MOKSLŲ CENTRAS

Aliona Klimovich

Adsorbuotų ant metalo paviršiaus biomolekulių tyrimai paviršiaus sustiprinta Ramano spektroskopija

DAKTARO DISERTACIJA

Gamtos mokslai,
Chemija (N 003)

VILNIUS 2025

Disertacija rengta 2020–2024 metais Fizinių ir technologijos mokslų centras. Mokslinius tyrimus rėmė Lietuvos mokslo taryba.

Mokslinė vadovė – dr. Ieva Matulaitienė (Valstybinis mokslinių tyrimų institutas Fizinių ir technologijos mokslų centras, gamtos mokslai, chemija – N 003).

Gynimo taryba:

Pirmininkas – prof. dr. Justinas Čeponkus (Vilniaus universitetas, gamtos mokslai, fizika – N 002).

Nariai:
Assoc. prof. dr. Renata Butkutė (Fizinių ir technologijos mokslų centras, gamtos mokslai, fizika –N 002),
Dr. Lina Mikoliūnaitė (Fizinių ir technologijos mokslų centras, gamtos mokslai, chemija – N 003),
Dr. Simonas Ramanavičius (Fizinių ir technologijos mokslų centras, gamtos mokslai, fizika –N 002),
Prof. dr. Cordelia Zimmerer (Leibnizo Polimerų tyrimų institutas Drezdenas, gamtos mokslai, chemija – N 003).

Disertacija ginama viešame Gynimo tarybos posėdyje 2025 m. rugsėjo mėn. 15 d. 15 val. Nacionalinio fizinių ir technologijos mokslų centro D401.
Adresas: Saulėtekio al. 3, Vilnius, Lietuva,
tel. +370 52649211; el. paštas office@ftmc.lt

Disertaciją galima peržiūrėti Vilniaus universiteto bibliotekoje ir VU interneto svetainėje adresu: *https://www.vu.lt/naujienos/ivykiu-kalendorius*

ABBREVIATIONS

AA – amino acids;
Ag NPs – argentum nano-particles;
bSi – nanostructured black silicone substrate;
bSi/Au – nanostructured black silicone substrate covered by gold;
diEG – diethylene glycol;
DOX – Doxorubicin;
EC-SERS – electrochemical SERS technique;
EF – enhancement factor;
    EM – electromagnetic mechanism;
    CE – chemical mechanism;
HOMO – the highest occupied molecular orbital;
LOD – limit of detection;
LSPR – localized surface plasmon resonance;
LUMO – the lowest unoccupied molecular orbital;
OCP – open circle potential of the system;
    (WE) – working electrode;
    (CE) – counter electrode;
    (RE) – reference electrode;
SERS – Surface-enhanced Raman scattering;
U-II – Urotensin II;
URP – Urotensin-related peptide;
UT – Urotensin receptor;
ZCP – zero-charge potential;
4-MBA – 4-mercaptobenzoic acid.

ν – stretching vibration;
δ – bending vibration;
d – deformation;
w – wagging;
ν_s – symmetric stretching vibration;
ν_{as} – asymmetric stretching vibration;
oop – out-of-plane movement;
sh – shoulder of band.

TABLE OF CONTENT

INTRODUCTION 7
1. THEORETICAL OVERVIEW 11
1.1 Biomolecules 11
1.2 Urotensin II peptide 13
1.3 Raman spectroscopy 16
1.4 Surface-Enhanced Raman Spectroscopy 20
1.5 The main types of SERS-active substrates 24
1.6 Raman/SERS technique for investigation of peptide 28
2. MATERIALS AND METHODS 31
3. RESULTS AND DISCUSSION 37
3.1 Raman spectra of Urotensin II peptide 37
3.2 SERS research of U-II using silver nanoparticles 38
3.3 EC-SERS research of U-II using Ag electrode 47
3.3.1 EC-SERS measurements performed in a buffer containing Na_2SO_4 ... 47
3.3.2 EC-SERS Measurements performed in a buffer containing $NaClO_4$ ... 55
3.4 Comparison of adsorption U-II peptide on Ag and Au substrate 65
3.5 Black silicone nanostructured SERS substrate 70
3.6 EC-SERS research of 4-MBA using bSi/Au substrate 73
CONCLUSIONS 82
BIBLIOGRAPHY 83
SANTRAUKA 100
LIST OF CONFERENCES AND PUBLICATIONS 112
Brief information about the author 114
ACKNOWLEDGEMENTS 115

INTRODUCTION

The diversity of biological molecules – proteins, nucleic acids, carbohydrates, lipids – is the fundamental basis of living organisms. These molecules perform a wide range of functions, from providing energy and structural support to encoding genetic information and facilitating chemical reactions. With the development of chemical, physical, and biotechnologies, it has become possible to collect detailed information about different substances at the molecular level. The study of biomolecules allows researchers to determine both the individual parameters of the molecule and the mechanism of their interaction, contributing to a more complete understanding of many processes occurring in the whole body. At the same time, a large number of molecules that have potential in terms of drug development require more careful research as individual substances. One of these molecules is the Urotensin II peptide, which has vasoconstrictor activity similar to that of endothelin-1 [1].

Human Urotensin II peptide (U-II) is a cyclic neuropeptide that was first isolated from the teleost fish *Gillichthys mirabilis* [2] and was long thought to be produced only by the urophysis of fish. U-II isopeptides with some divergence in the amino acid sequence from the N-terminal region and the conserved disulfide-linked cyclic hexapeptide sequence c–[Cys–Phe–Trp–Lys–Tyr–Cys] in the C-terminal region [3], have been shown to occur in several species (rat, pig, goby, monkey), including humans [4]. The U-II peptide and its signaling system have recently attracted attention due to their neurotransmitter and neuromodulator activities, inhibition of glucose-induced insulin secretion, and the possibility of using it as a target for the drug treatment of various inflammatory diseases [5–9]. To date, there is a large amount of knowledge about the biological activity of the peptide; however, there is a critical lack of information about the physical properties of the molecule itself. The conformation of human U-II peptide in aqueous solutions was determined only by ^{1}H-NMR spectroscopy and molecular dynamic studies [3,10,11]. However, the complexity of the U-II molecule limits the analysis of its structure and the mechanisms of interactions between U-II and its receptors (orphan receptor GPR-14 or UT receptor), which considerably complicates the development of synthetic analogs of U-II for pharmaceutical and medical applications [12].

Raman spectroscopy is a very valuable technique that enables the study different types of molecules on a qualitative and quantitative levels [13,14]. Each substance has a unique Raman spectrum, which is a "fingerprint" of the molecule [15,16]. Information such as the secondary structure of peptides and

proteins, bonding within the molecule, the condition of functional groups, interactions between molecules, etc., can be obtained using Raman spectroscopy [17–19]. The discovery that Raman signals can be amplified by exciting localized surface plasmon resonances (LSPR) of adsorbed molecules on the roughened metal surface led to the development of surface-enhanced Raman spectroscopy – SERS – which enables the detection of analytes at extremely low concentrations, even in solution [20]. The investigation of biomolecules such as peptides and proteins using the Raman and SERS methods is widely applied in many scientific and industrial fields, including analytical chemistry, biochemistry, and biotechnology.

The Raman spectrum of a pure substance makes it possible to study the molecule in its native state. When compared with the Raman spectrum obtained after a chemical reaction, it is possible to trace structural changes in the molecule under investigation. The additional use of electrochemistry in the SERS measurements allows for an increased concentration of molecules on the surface and helps determine the influence of electrical potential on molecular behavior. SERS measurements used to study the adsorption of the investigated molecules on metal surfaces can serve as models for understanding the interaction of a molecule with its receptor. The chemical identification of the adsorbed species, their protonation/deprotonation states, molecular structure, and the orientation of the adsorbates on the surfaces can all be described *in situ* using SERS methods on different types of metal surfaces.

Goal of the research work

The main goal of this work is to investigate the structure of the human Urotensin-II cyclic peptide at the molecular level, to determine its adsorption peculiarities on metal surfaces of different nature and structure, and to examine its interaction with anions of various natures.

To achieve this goal, **the following five tasks were set**:

1. To record and assign Raman and SERS spectra of cyclic peptide human Urotensin II;
2. To study the adsorption mechanism of the U-II peptide on silver nanoparticles (Ag NPs) and to evaluate the effect of an additional washing process;
3. To determine the influence of electrochemical potential, anion type and metal nature on the adsorption mechanism of the U-II peptide;
4. To assess the suitability of black silicon/gold (bSi/Au) substrates for repeated use in SERS measurements;

5. Using quantum chemical calculations, to evaluate the feasibility of employing the bSi/Au substrate as a working electrode for alternative to classical gold electrode.

Novelty and relevance

In this work, the Raman and SERS measurements of the U-II peptide have been performed experimentally for the first time. The Raman spectrum of U-II molecule provides the main vibrational bands from the functional groups of Phenylalanine, Tryptophane, Tyrosine amino acids located in the cyclic moiety of peptide, and the disulfide (S–S) bridge between the two Cysteine residues. The position of bands from S–S bridge can indicate the main presence of P_C–T conformers of –CSSC– bonds in U-II peptide in solid state.

The SERS spectra of U-II using silver nanoparticles (Ag NPs) and silver (Ag) electrode were obtained. The main enhanced bands were assigned to the aromatic amino acids located in the cyclic part of the peptide. The presence of a band at 509 cm^{-1} (S–S) confirms that the disulfide bridge between two Cys amino acid residues in the U-II peptide does not break during adsorption process. The presence of Amide I and Amide III vibrations confirms the peptide's cyclic structure.

Additional EC-SERS study of U-II peptide on Ag electrode at applied potentials ranging from – 1.0 V to 0.0 V and the changes in the position of the molecule on the surface under the influence of the applied potential can be used as a model for studying the mechanism of the interaction between the U-II molecule and its receptor.

The use of a black silicon/gold (bSi/Au) substrate to obtain the SERS spectra of the Urotensin II molecule showed that metal-type replacement on SERS surface – from Ag to Au – leads to a slight change in the adsorption mechanism of the peptide molecule, which involves greater adsorption of Tryptophan and the alkyl chain of the molecule, particularly Lysine.

It has been shown that bSi/Au substrates are suitable for repeated use and can be applied to model objects. It has been found that these substrates can detect Doxorubicin (DOX) in a concentration range of 10^{-9}–10^{-4} M, and the high amplification of SERS signals from the substrates persists for up to 20 months. The possibility of using this type of substrate for EC-SERS measurements was demonstrated by density functional theory (DFT) modeling. An experimental proof-of-concept study with the test molecule – 4-mercaptobenzoic acid (4-MBA) – showed changes in the molecule's SERS spectra as a function of the applied potential.

The description of the Urotensin II peptide by Raman and SERS spectroscopy makes it possible to explore the changes taking place in the molecule during adsorption on metal surfaces, and to propose possible mechanisms for adsorption and interaction with the receptor. This information can ultimately be used to produce synthetic analogues of molecules with comparable properties.

Statements of the thesis

1. During the adsorption of the Urotensin II peptide on the metal surface, the disulfide bridge between the two Cysteines remains intact, and the interaction with the metal surface occurs via aromatic amino acid residues located in the cyclic part of the molecule;
2. During adsorption on Ag NPs, U-II displaces citrate anions from the silver surface, and during washing process, it fully replaces the washed-out citrate anions by interacting through the Asp and Glu residues;
3. As the system potential changes, the molecule reorients with respect to the electrode, and additional adsorption occurs via the Lys residue. When the potential of the Ag electrode becomes more negative, the distance between the U-II peptide and the electrode surface decreases. The replacement of anions in the system (from Na_2SO_4 to $NaClO_4$) does not significantly affect the U-II peptide adsorption mechanism;
4. The nature of the metal does not have a significant influence on U-II peptide adsorption; on a gold surface, the molecule shows a stronger tendency to adsorb via Trp and Lys residues;
5. Nanostructured silicon coated by gold can be used as reusable SERS platforms, exhibiting high sensitivity and long-term stability, with potential for practical use as a working electrode for EC-SERS measurements.

1. THEORETICAL OVERVIEW

1.1 Biomolecules

Biomolecules – organic compounds produced in the cells of living organisms during vital processes. The main chemical elements of biomolecules are carbon, hydrogen, oxygen and nitrogen, as well as phosphorus and sulfur. Biomolecules are the basis of all living organisms and, due to their variety of shapes and sizes, fulfill many functions such as regulation, protection, transport, energy, structure, and apoptosis. The most important classes of biomolecules are nucleic acids (DNA and RNA), amino acids, peptides and proteins, lipids, carbohydrates, vitamins, hormones and various types of metabolites [21–23].

Nucleic acids (DNA and RNA) are consecutive chains of nucleotides, which are the most important molecules in a cell and are stored in the chromosomes. Nucleotides, the building blocks of DNA/RNA, consist of a nitrogenous base, a monosaccharide, and phosphoric acid, and form phosphodiester bonds between them. DNA stores the genetic information of a cell and determines the sequence of amino acid residues in peptide formation. RNA has both messenger and transfer functions in the cellular process.

Lipids are a diverse group of compounds whose common property is the ability to dissolve in nonpolar organic solvents. In a cell, lipids perform structural (form cell membranes), signaling, and barrier functions. Lipids also perform energy storage (1 g = 9 kcal) and protective functions in the body [23].

Carbohydrates are aldehyde or keto polyhydroxy alcohols and their polymers divided into several groups – monosaccharides, disaccharides, oligosaccharides and polysaccharides. The main function of carbohydrates is energy production, as carbohydrates are the body's main source of energy. Receptor, structural and protective functions of carbohydrates are also important. This class of compounds is the main (by weight) organic matter on Earth [23].

Amino acids are the main building blocks of peptides (up to 5.000 Da) and proteins (over 5.000 Da) and consist of a positively charged amino group $–NH_2$ and a negatively charged carboxyl group –COOH. A characteristic feature in the structure of α-amino acids is the presence of a chiral carbon atom, which is the reason for the existence of enantiomers (the exception being glycine). In total, more than 500 types of amino acids are known, but only 21 of them are essential. During the formation of peptides and proteins, amino acids are sequentially connected in a certain order by forming a peptide bond

–C(=O)–NH– between the amino group of one residue and the carboxyl group of the next residue. The theoretical number of peptides that can be constructed from n=20 natural amino acids: 400 dipeptides, 8000 tripeptides, etc. shows that combinatorically, at n = 62, the number of possible peptides exceeds the number of atoms in the Universe (10^{80}).

The structure of the polypeptide chain in proteins is usually characterized by four levels of organization (Fig. 1). The sequence of amino acids in the polypeptide chain is called the primary structure and determines the chemical properties and further spatial structure of the molecule. The polypeptide chain is linear in only a few proteins. In most protein molecules, the polypeptide chain is folded in a specific way in space.

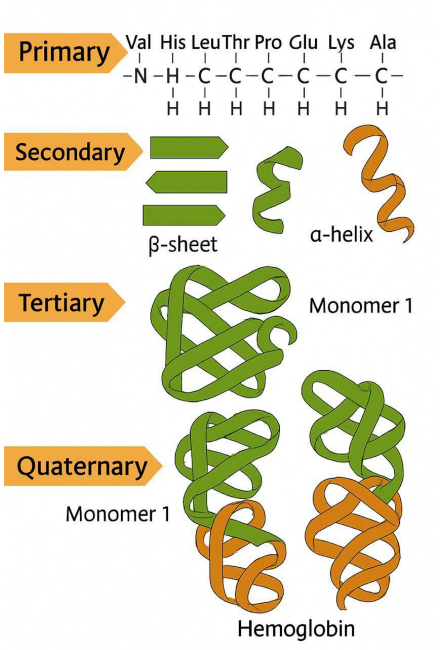

Figure 1. Summary of protein structure (primary, secondary, tertiary, quaternary). Adapted from [24].

The secondary structure – α-helices and β-sheets – is determined by the conformation (folding) of the polypeptide chain due to the formation of hydrogen bonds between the –NH and –CO groups of different amino acids. The α-helix is characterized by the 3,6 amino acid residues per turn, and all lateral substituents are located outside the α-helix. The β-sheets structure is characterized by the formation of hydrogen bonds between relatively distant amino acid residues (approximately 0.347 nm) and its multidirectional

alignment. Any secondary protein structure contains both α-helices and β-sheets, as well as irregular secondary structures - turns and transitions [22,25].

The three-dimensional configuration of protein called the tertiary structure and is formed by disulfide bridge between cysteine residues, ionic interaction between –NH and –CO charged groups and hydrophobic interactions among side chain residues. During the formation of the tertiary structure, the size of the molecule decreases significantly (by up to tenfold), and for most of the proteins, this is the final level of spatial organization.

Some proteins with a large molecular weight are characterized by a quaternary structure that unites several autonomous regions of the molecule into a larger complex.

Peptides and proteins are important components of living organisms and perform a variety of functions. Most proteins, such as collagen, keratin and elastin, perform structural or mechanical functions in the cell and form hard or filamentous structures such as hair, nails, and feathers [25]. The regulatory and signaling functions of proteins are among the most important for cellular and systemic processes. Proteins regulate transcription, translation, and splicing within the cell, as well as the activity of other proteins, and many other processes. Protein kinases and protein phosphatases activate or inhibit the activity of other proteins by attaching or cleaving phosphate groups, while insulin regulates the concentration of glucose in the blood. Some proteins are stored in the body as an energy source (1 g of protein = 4.1 kcal) or as a source of amino acids. The transport function is exemplified by the transfer of oxygen by hemoglobin [26]. Proteins also form antibodies and hormones, and influence gene activity.

This great diversity of biomolecules enables this class of substances to carry out numerous functions in a living organism. The study of individual molecules using different methods makes it possible to understand the mechanisms of the processes taking place in the body and to develop more effective methods for combating diseases, designing promising materials with specific properties, and creating new drugs, etc. in the future [27].

1.2 Urotensin II peptide

Human Urotensin II (U-II, NH–Glu–Thr–Pro–Asp–Cys–Phe–Trp–Lys–Tyr–Cys–Val–OH) is a cyclic peptide molecule with neurohormone-like activity that was first discovered in 1969 in Goby fish (*Gillichthys mirabilis*) [4,28]. The Urotensin II peptide molecule has variable amino acid sequence lengths (from 11 to 17) in different animal species [4,29]. Human Urotensin II has 11 amino acid residues and there is a covalent disulfide bridge between

two Cys residues at the C-terminus of the molecule. As a result, the molecule has a stable cyclic conserved hexapeptide moiety – [Cys–Phe–Trp–Lys–Tyr–Cys]. The structure of the U-II peptide is presented in Figure 2. The first sequencing of this peptide was performed in 1992 by Michael Conlon et al. and this sequence was confirmed by chemical synthesis [30]. The U-II system consists of three molecules: Urotensin II, Urotensin-related peptide (URP) and Urotensin II receptor (UT) [31]. The U-II receptor is an orphan G-protein-coupled receptor, named GPR14, originally discovered and cloned by Tal et al. in 1995 [32] and renamed UT in 1999 after initial work by Ames et al. [33].

The main physicochemical parameters of human U-II are: Mr 1,388.6, pI 4.37. It is freely soluble in water, ethanol and 20% acetonitrile/water. The structural and functional features explained in detail in the paper by Castel H. et al [34]. First structural studies of U-II by nuclear magnetic resonance spectroscopy (NMR) showed that the peptide did not adopt any classical secondary structures in aqueou solution [35]. Moreover, NMR studies performed by Haensele and al. [3] revealed that cyclic part of the U-II molecule, c–[Cys–Phe–Trp–Lys–Tyr–Cys], adopts several conformations – the *unfolded open* and *saddle-like* folded ring conformations, which are further classified into a total of 11 subtypes – that differ in the type of intramolecular hydrogen bonds.

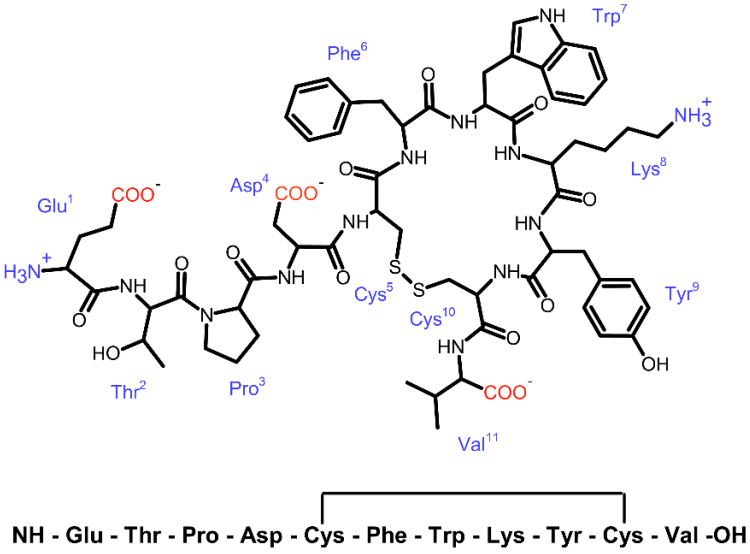

Figure 2. Structure of the Human Urotensin-II peptide.

In aqueous solution U-II exhibits the open and folded confirmations in the ratio of 72%:28%. Turns of different kinds centered at Lys–Tyr or Phe–Trp are defined as the *unfolded open* ring conformers; they tend to have few or no transannular hydrogen bonds. The folded (*saddle-like*) conformations are characterized by turns of various types centered at Phe–Trp–Lys or Trp–Lys–Tyr and stabilized by densely packed transannular hydrogen bonds [3]. Because of the turn centers, each subtype has characteristic secondary structure motifs such as α-helix, β-hairpin motif, β-turn. The amino terminus also has extended or folded conformations with respect to the ring and can be chemically modified without significant loss of activity (U-II and URP) [36]. On the opposite side, the breakage of the S–S bond reduces the immunoreactivity of U-II [37].

Compared to endothelin-1, the U-II peptide has recently attracted attention for being a strong vasoconstrictor [38]. In recent years, high plasma levels of U-II have been reported in some human diseases such as heart failure [5,6], especially hypertension [7], diabetes [39] and kidney disease [8,40]. The U-II peptide may also act as a neurotransmitter and/or neuromodulator to regulate various neurobiological activities. The review by Do Rego J-C et al. [41] provides a detailed list of works that show experimentally (in mice) that injection of U-II into the central nervous system prolongs the duration of REM sleep, induces anxiety- and depressive-like states and increases feeding activity.

In addition, U-II inhibits glucose-induced insulin secretion in the isolated rat pancreas [9]. In the kidney, U-II affects sodium transport, lipid and glucose metabolism, and exerts vasodilatory and natriuretic effects [42,43].

In recent years, U-II and its signaling system have been used as targets for the drug treatment of various inflammatory diseases. In animal studies, U-II receptor antagonists are used to block signal transduction of the U-II/UT system, leading to satisfactory anti-inflammatory results. However, the research and development of drugs for the treatment of human diseases has not yet begun. Given the broad spectrum of diseases related to inflammation, breakthroughs in inflammation therapy research will bring revolutionary advances in the clinical treatment of diseases in the future.

With the growing interest and discovery of the direct involvement of U-II in important physiological processes, it is clear that a rapid, accurate method with minimal sample preparation will become a necessary tool for further research into U-II and URP molecules.

With the development of Raman spectroscopy and the growing understanding of its advantages for the study of biological molecules, the potential application of this method for the characterization of the human

Urotensin II peptide has become increasingly apparent. Raman spectroscopy provides additional insight into the physical properties of molecules and facilitates the study of inter- and intramolecular hydrogen bonding. Furthermore, by using SERS, it is possible to study the interactions of the molecule with various types of metal surfaces as well as its behavior under varying potential of the system. These findings could further contribute to the understanding of the interaction between the U-II peptide and the UT receptor.

Therefore, the primary objective of this dissertation is to explore the human Urotensin II peptide using Raman and SERS spectroscopy techniques. It is important to note that these methods are being applied to study this molecule for the first time.

1.3 Raman spectroscopy

Vibrational spectroscopy is a powerful method of studying substances, based on the process of interaction of light with the studied molecules. Through the absorption or scattering of light, it becomes possible to analyze the chemical structure and determine the chemical composition of the sample. Various methods, such as infrared (IR) spectroscopy (including Near-Infrared (NIR) and Mid/Far-IR spectroscopy, often implemented via Fourier-transform (FTIR)), as well as Raman spectroscopy (including SERS and Resonance Raman spectroscopy), allow for the study of samples in various aggregation states across a wide range of wavelengths relevant to vibrational transitions [44].

The vibrational motions of molecules are determined by their vibrational, degrees of freedom. The number of vibrational degrees of freedom and their corresponding normal oscillations is (3n – 5) for linear molecules and (3n – 6) for nonlinear molecules, where **n** is the number of atoms in the molecule. For example, the disulfide oxide molecule SO_2 is nonlinear and has 3 vibrational degrees of freedom, while the linear acetylene molecule C_2H_2 has 7 vibrational degrees.

Vibrations of molecules can involve changes in bond lengths (valence/stretching vibrations, ν) or angles between bonds (deformation/bending vibrations, δ). Stretching vibrations can be symmetric and antisymmetric, and deformation vibrations are divided into scissoring, rocking, wagging and twisting (Fig. 3). For more complex molecules, in which one of the deformational oscillating parts is much more massive than the other, deformation vibrations are more often described as planar and out-of-plane.

The oscillations, which consist of the simultaneous change of several bond lengths or valence angles, are called skeletal.

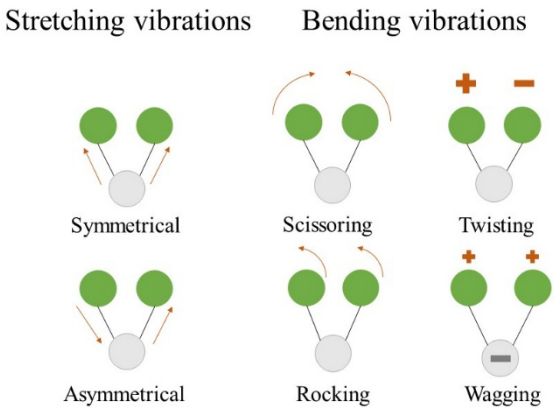

Figure 3. Common vibrational modes of chemical bonds [44].

Subset of vibrational spectroscopy – Raman spectroscopy – one of the methods used for investigation of compounds with great sensitivity based on unique vibrational properties of molecules. In the process of inelastic scattering of photons, a characteristic Raman spectrum of the substance is formed, which allows to estimate the nature of the vibrations that are activated during the absorption of light by the molecules.

Raman scattering as a phenomenon involving the presence of bands with shifted frequencies in the scattered light of samples was first theoretically predicted by the Austrian scientist Adolf Smekal in 1923 [45] and practically discovered by Indian physicist Chandrasekhara Venkata Raman in 1928 [46].

The Raman effect has the following characteristics. During the irradiation of the sample, the photon stream with energy $h\nu_0$ can be reflected, absorbed or scattered, as a result of which the molecule can switch to a different energy state than the original one. During the scattering process, most collisions are elastic, so the energy of the scattered photons remains unchanged (Rayleigh scattering). If inelastic scattering occurs (Raman scattering), the energy states of the molecule changes and can be descripted by equation (1):

$$h\nu_0 + E = h\nu' + E'$$
$$\Delta E = h(\nu' - \nu_0) \quad (1)$$

where ν_0 and ν' are the incident and scattered frequencies respectively. Similarly, E and E' are the initial and final energy of a molecule.

The essence of the phenomenon of Raman scattering is that in the spectrum of scattered light additional lines are located on the long-wavelength (Stokes components) and short-wavelength (anti-Stokes components) sides of the Rayleigh line (Fig. 4). Based on the equation (1), the scattered radiation can be classified as follows:

$$\Delta E = 0 \text{ if } \nu_0 = \nu' \text{ – Rayleigh scattering}$$
$$\Delta E < 0, \text{ when } \nu_0 > \nu' \text{ – Stokes scattering}$$
$$\Delta E > 0 \text{ if } \nu_0 < \nu' \text{ – Anti-Stokes scattering}$$

The schematic energy level diagram for Rayleigh, Stokes and Anti-Stokes scattering is shown in Figure 4.

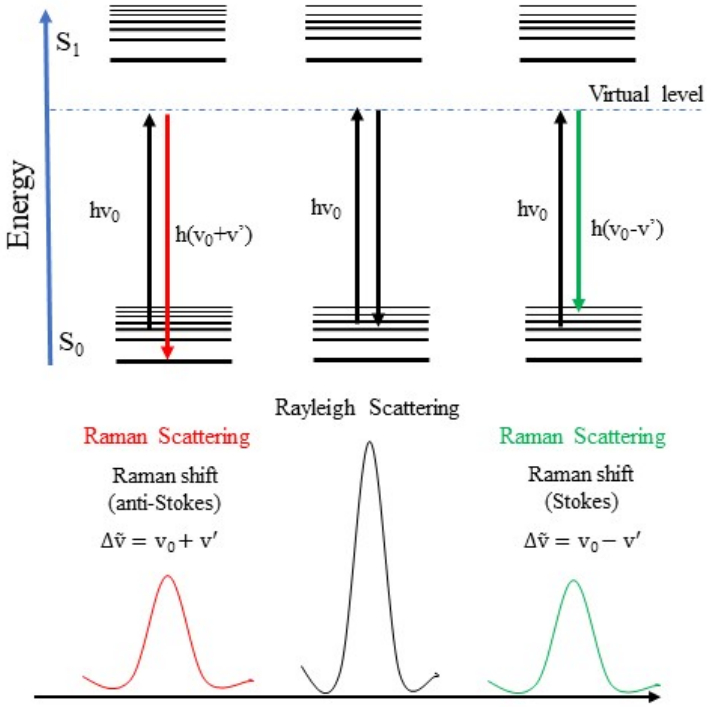

Figure 4. Scheme of the Rayleigh and Raman scattering of light. S_0 – ground electronic state, S_1 – first exited electronic state, $h\nu_0$ – incident light energy [44].

The frequency, intensity, degree of polarization, width and other parameters of these additional lines are clearly determined by the internal structure of the investigated system – its intramolecular or intermolecular vibrations. The selection rules for Raman spectroscopy consist of a stronger amplification of the signals of symmetrical vibrations and vibrations of non-

polar groups and a lower amplification of asymmetrical vibrations and polar groups [44]. The mechanism of Raman scattering, according to the classical theory of electromagnetic radiation, is related to the polarizability of molecules. The dipole moment (μ) is proportional to the electric field strength (E):

$$\mu = a\,E = \alpha E_0 \cos(2\pi v_0 t) \tag{2}$$

where α – the polarizability of the molecule, ν_0 – frequency of incident light.

It is to be expected that the polarizability will be a function of the nuclear coordinates and at the moment when the molecular system is interacting with the harmonically oscillating electric field at the frequency ν_o, the variation of components in the polarizability tensor with vibrational coordinates is expressed in a Taylor series (3):

$$\alpha = a_0 + \left(\frac{da}{dx}\right)_e x + \frac{1}{2}\left(\frac{d^2a}{dx^2}\right)_e x^2 + \cdots \tag{3}$$

where x – oscillation.

The deviation of nuclei from the equilibrium position and the distance between the nuclei time dependence is a periodic function of oscillation:

$$x = x_0 \cos[2\pi v' t + \varphi_0] \tag{4}$$

where x_o – amplitude, φ_o – initial phase, ν' – frequency of scattered light.

In the moment, when all parameters are inserted into the equation (2), the induced dipole moment module can be characterized as:

$$\mu = \left[a_0 + \left(\frac{da}{dx}\right)_e x_0 \cos[2\pi v' t + \varphi_0]\right] E_0 \cos(2\pi v_0 t) \tag{5}$$

Rayleigh scattering comes from the dipole oscillating at ν_o induced in the molecule by the electric field of the incident radiation at frequency ν_o. Raman scattering arises from the dipole moment oscillating at $\nu_o \pm \nu'$ produced by the modulation of the dipole oscillating at ν_o with molecular vibration at frequency ν' [47].

Full description of the process characterized in equation (6):

$$\mu = a_0 E_0 \cos(2\pi v_0 t) + \left(\frac{da}{dx}\right)_e x_0 E_0 \cos[2\pi(v_0 - v')t + \varphi_0] + \\ + \left(\frac{da}{dx}\right)_e x_0 E_0 \cos[2\pi(v_0 + v')t + \varphi_0] \quad (6)$$

Due to the development of technology and the discovery of the laser in the 1960s [48], Raman spectroscopy has become the routine analytical method. Due to its advantages such as a compound's fingerprint, very fast identification and real-time monitoring, lack of sample preparation and its non-destructive technique allowing the analysis of very complex mixtures [15,16,49–54]. An additional important feature such as the ability to obtain a Raman spectrum of the substrate without opening the packages makes this method the most promising in the field of analytical science [55–57], forensic science [58], the study of biological systems [59], especially *in vivo* process studies [60].

Nevertheless, Raman spectroscopy has some significant disadvantages. The Raman effect is a relatively weak process and requires high concentration of molecules (C_{min}=0.01 M) [61]. High laser powers can damage samples due to overheating and burning, and fluorescence from impurities or the sample itself can obscure the Raman spectrum [62,63]. Another important factor, limited penetration depth, can also limit the use of Raman spectroscopy for the study of multilayered samples [14].

However, an accidentally discovered effect – surface-enhanced Raman spectroscopy – allows one to eliminate most of the disadvantages of the method and make it more accessible for wider application.

1.4 Surface-Enhanced Raman Spectroscopy

The surface-enhanced Raman spectroscopy – SERS – an ultra-sensitive vibrational spectroscopic technique for detecting molecules on or near the surface of metallic nanostructures. This effect was first observed in 1974 by Martin Fleischmann, Patrick J. Hendra and A. James McQuillan during the experiment on the Raman scattering of pyridine on roughened silver electrodes [20]. Following this discovery, subsequent research demonstrated that SERS represents a giant enhancement of regular Raman scattering, and in the beginning of 1980s the plasmon theory of SERS mechanism was presented [64–66]. The enhancement of Raman signals from molecules absorbed on nanostructured metal surfaces can reach magnitudes from 10^6 to 10^{10} [67]. In

1997, considerable interest in SERS was revived with the publication of one of the first articles on single molecule detection [68,69].

The enhancement mechanism in SERS is well understood within the classical plasmonic theory. This theory states that the incident light can excite collective oscillations of the free electrons on the surface of substrate and the concentration of electromagnetic energy in the vicinity of a metal nanoparticle increases to enhance the radiation efficiency of the oscillating dipoles from the molecules [70]. A necessary condition for efficient SERS is close contact between the analyte and the substrate, and the SERS effect is strongest at the junctions between the individual nanoparticles.

In the aqueous phase, the surface chemistry controls the interaction between analyte and substrate. This often limits SERS applications to a limited number of analytes that strongly adsorb to colloidal metal substrates [71]. There are currently at least two amplification mechanisms: short-range chemical enhancement – CE, and long-range electromagnetic enhancement – EM. In theory, CE is probe-dependent and requires some kind of chemical interaction of the analyte with the metal surface, whereas EM enhancement is independent of the type of adsorbed molecule.

Chemical enhancement mechanism

Chemical (or charge transfer) enhancement is the mechanism that involves the binding of molecules to the surface of the SERS substrate. Chemical enhancement should occur only for molecules that are directly bound to the surface and therefore should only increase up to monolayer coverage. The chemical effect has been studied and described in important papers by J. Lombardi [72], A. Campion [73], and A. Otto [74].

The theory of the chemical enhancement mechanism includes several different transitions/processes. The direct covalent binding of the adsorbate to the metal surface (chemisorption) creates new electronic states that act as resonant intermediate states: HOMO – the highest occupied molecular orbital and LUMO – the lowest unoccupied molecular orbital (Fig. 5).

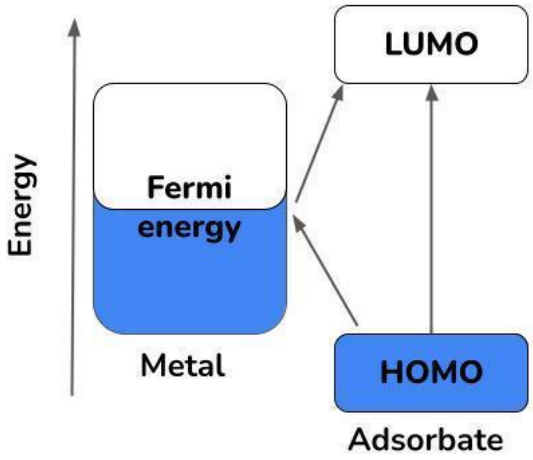

Figure 5. The energy level diagram of the metal–molecule system [75].

When the metal−molecule bond is formed, the target molecules are able to transfer electrons to/from the metal surface in both ground and excited states, and the scattering cross-section of scattering of the molecules increases, which also increases the final intensity of Raman scattering [72]. The mechanism of chemical enhancement leads to a maximum enhancement of the order of 10^2. Even though the chemical enhancement is small in magnitude, this mechanism determines the important spectral patterns such as the Raman shifts and the band intensity ratios in the SERS spectra of the measured molecules.

Compared to the other type of amplification – electromagnetic enhancement (EM) – CE seems quite insignificant, but in fact the chemical interaction makes it possible to study how the investigated substance interacts with the SERS surface.

Electromagnetic mechanism

The second type of SERS amplification – electromagnetic – is related to the nature and the possibility of the SERS surfaces for signal amplification through the ability of nanostructures to concentrate electromagnetic energy, known as localized surface plasmon resonance (LSPR) [76]. In the areas where the distances between the nanoparticle and molecule are smallest, the electric field lines are maximally compressed, and these areas are referred as “hot spots”. There is a possibility that the intensity of Raman scattering increases significantly, assuming that the incident and scattered fields are enhanced [77].

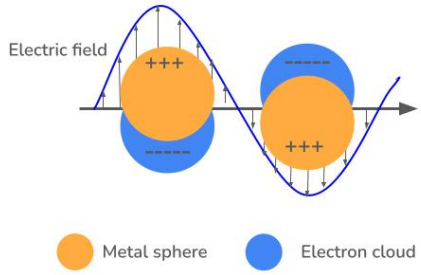

Figure 6. Scheme of localized surface plasmon resonance (LSPR) effect [76].

When the incident beam interacts with the nanoparticle, a local signal amplification occurs, which is described as:

$$E_{lok} = E_0 \lambda_0 M_{lok} \quad (7)$$

$\lambda_0 M_{lok}$ - local enhancement factor.

Next, this amplified signal interact with the molecule and the first amplification of the molecule's scattered Raman signal occurs (E_{scat}). The gain is described by the equation (8):

$$E_{scat} = \alpha E_{lok} = \alpha E_0 \lambda_0 M_{lok} \quad (8)$$

Since the molecule is in a close proximity to the nanoparticle, the enhanced Raman signal (E_{scat}) from the molecule radiated on particles again and a second amplification of the Raman signal (E_{rad}) occurs, which is described by the equation (9):

$$E_{rad} = E_{scat} \lambda_R M_{scat} = \alpha E_0 \lambda_0 M_{lok} \lambda_R M_{scat} \quad (9)$$

Signal intensity gain can also be described as:

$$I_{SERS} = M_{lok}^2 \lambda_0 M_{scat}^2 \lambda_R I_{Raman} = G_{SERS} I_{Raman} \quad (10)$$

where I_0 - the Raman signal intensity scattered by the molecule without the proximity of any metallic nanoparticle and without any enhancement.

As a result, the signal is amplified twice and allows to obtain a stable, enhanced Raman spectrum from the molecule under study, even at relatively low concentrations [76].

The necessary condition for the localized surface plasmon resonance is the presence of free electrons, which create the necessary signal amplification

(Fig.6) [77]. The location of the plasmon resonance (ω_p) is a function of the free carrier density (N) of the substrate, where m^+ is the effective mass of the charge carriers (electrons or holes):

$$\omega_p = \left(\frac{4\pi N e^2}{e_0 e_\infty m^+}\right)^{1/2} \quad (11)$$

Metals such as Au, Ag and Cu have the highest free charge carrier densities and show accessibility to plasmon resonance in the visible range of the light spectrum (400–800 nm). Therefore, they are often used as plasmonic substrates for SERS [78].

However, although EM is a long-range effect, the electromagnetic gain decreases with $1/r^3$ with distance from the surface. Therefore, most of the electromagnetic enhancement will also come from adsorbates present up to a monolayer on the surface as for chemical enhancement. The vast majority of evidence suggests that both effects play a role, although electromagnetic enhancement is generally thought to play a larger role than chemical enhancement and it is almost impossible to separate the CE effects from a system that supports EM enhancement. The equation (12) can formally illustrate the relationship between Raman and SERS (P_{Raman} and P_{SERS}) scattered powers:

$$P_{SERS} = G_{SERS} P_{Raman} = G_{SERS}^{EM} G_{SERS}^{CM} P_{Raman} \quad (12)$$

where G_{SERS}^{EM} and G_{SERS}^{CM} are contributions of electromagnetic enhancement and chemical enhancement mechanisms of SERS [75].

1.5 The main types of SERS-active substrates

The type of surface or nanostructures and the material of the substrate play an important role in the fabrication of SERS substrates. The following additional parameters can also be highlighted and must be taken into account in the production of SERS substrates:

1. High amplification capacity. The substrate should significantly enhance the Raman signal (through hot spots or strong plasmon resonances);
2. Reproducibility. The substrate with uniform nanostructures and their precise geometry must provide a stable and reproducible signal;
3. Chemical/ mechanical stability in the environment;

4. Low background signal. Minimal Raman scattering or fluorescence signal from the substrate itself;

5. Low cost and ease of production of substrates;

6. Biocompatibility (for biomedical applications). Analysis of biomolecules requires non-toxic and inert substrates without negative biological reactions [17,75,79].

With the development of SERS technologies and the discovery of various materials capable of amplifying the Raman signal, noble metals remain the most used materials for the production of SERS substrates [75]. Noble metals such as Ag and Au can produce intense electromagnetic field enhancements and significantly enhanced Raman signal in the visible and near infrared wavelength range [80]. However, it is worth noting that each metal has its own characteristics, which may impose limitations in practical use. Both Ag and Au materials have shown antimicrobial and antibacterial activities, good EM enhancements and stability. However, the EM in Ag is about three orders of magnitude stronger than in Au and allows the cost of producing the substrate to be significantly reduced due to its low price. Nevertheless, the main advantage of Au is its low chemical activity and low oxidation threshold compared to Ag, which is a more important criterion in practical applications [81]. Copper and aluminum are used less frequently due to their tendency to form a native oxide layer in air [82].

Some other types of metals – Li, Na, Fe, Co, Ni, Rh, Pd, Pt – can also be used for SERS measurements [83]. ZnO and TiO_2 nanostructures are often utilized as SERS substrates due to their photocatalytic activity, high uniformity and high refractive index. The first SERS spectra from the metal oxide-based substrates were obtained in 1982 [84]. Since that time, materials such as VO_2, Cu_2O, ZnO, Fe_3O_4, and WO_3 have been used as SERS materials because of the large number of free electrons, which can lead to the generation of the LSPR effect [85–87]. In 2014, Ling et al. [88] proposed the transition metal dichalcogenides (TMDs) as a non-noble metal SERS substrate. TMDs are based on a transition metal atom (group IIIB – VIIIB) and a chalcogen atom (S, Se, Te) as anion. Materials such as MoS_2 and WS_2 have unique electronic properties that can provide significant chemical enhancement mechanisms for SERS detection [89,90]. Also, one of the new developments is MXenes – Transition metal carbides and nitrides. The 2D titanium carbide $Ti_3C_2T_X$ [91] was first presented by Sarycheva et al. in 2017. They are emerging as potential SERS substrates due to their tunable surface chemistry and excellent electrical conductivity. In addition, hybrid organic-inorganic porous materials such as metal-organic frameworks (MOFs) enable the controlled trapping of analytes, which can be advantageous in combination

with plasmonic nanoparticles for the amplification of Raman signals [92]. Classic carbon nanomaterials such as graphene and carbon nanotubes are widely used due to their excellent chemical stability and their ability to support charge-transfer mechanisms [93]. Graphene oxide (GO) [94], nitrogen-doped graphene [95] and graphitic carbon nitride (g-C_3N_4) [96] are being explored due to their potential to provide effective Raman signal enhancement, often combined with metal nanoparticles to improve overall SERS performance.

But as practice shows, not only the type of metal determines the enhancement factor of the substrate, also the shape or structure of the substrate used for the SERS measurement. Many different roughened surfaces such as aggregated colloidal suspensions [97], composite colloids, nanostructures deposited on a solid surface, e.g. gold island films over a nanosphere [79], are often used as substrates to enhance the Raman signal by creating random hot spots on the surface. These structures are often created by chemical synthesis or self-assembly techniques [98], micropipetting, soaking, the Langmuir-Blodgett technique [99] and electron beam lithography [100]. However, several drawbacks such as instability in time, lack of uniformity and low reproducibility limit the use of these substrates for SERS [101]. Gold and silver nanoparticles are widely used due to their excellent plasmonic properties, ease of production and cost-effectiveness. Different shapes such as nanostars [102], nanocubes [103], nanospheres and nanotriangles [104] can significantly affect the enhancement factor by generating "hot spots" where the electromagnetic field is intensified. In addition, Shell-Isolated Nanoparticle-Enhanced Raman Spectroscopy (SHINERS) – Au and Ag nanoparticles covered by a thin SiO_2 layer (Au@SiO_2, Ag@SiO_2) – was introduced for the first time in 2010 [105]. The inert silicon dioxide shell protects the nanoparticles from agglomeration and oxidation and makes it possible to dispense with stabilizers during the synthesis of the NPs. The use of fewer substances in the synthesis of nanoparticles avoids the appearance of additional bands in the SERS spectrum of the molecule under investigation.

Nanorods and Nanowires with an elongated structure provide a large surface area and can form dense arrays that are ideal for generating uniform and repeatable SERS signals. Nanorods are particularly useful in array formats for better control over the enhancement effect [106–108].

Another type of SERS surface is an electrochemically prepared electrode surface. Electrodes made of gold, silver or copper metals are most commonly used for this purpose. The use of electrodes as SERS surfaces is one of the methods that makes it possible to obtain a stable and repeatable SERS surface that can be updated before each experiment without the need for tedious prior synthesis. The methods for preparing different types of electrodes differ

depending on the type of metal used. Due to the use of the electrode as a SERS substrate, the experiments were subsequently performed using the electrochemical SERS (EC-SERS) technique. By varying the potential of the electrode surface, it is possible to increase the number of molecules near the SERS surface and amplify the Raman signal [109]. In addition, EC-SERS is a surface analysis technique for *in-situ* analysis of the adsorption behavior of simple organic/inorganic molecules [110,111].

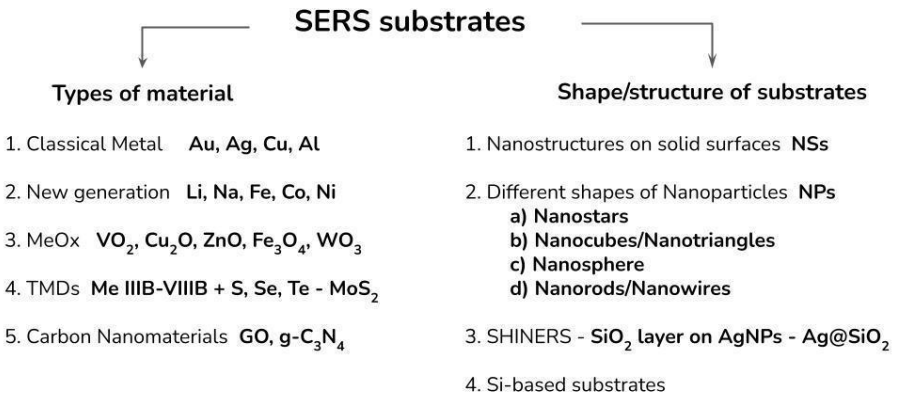

Figure 7. Classification of substrates for SERS spectroscopy.

Surface-enhanced Raman spectroscopy techniques generally use a metallic nanostructured substrate to achieve an enhancement factor around 10^6 – 10^8. At the same time, the progress in the development of science and technology enables the fabrication of substrates of different materials, structures and shapes. However, undoubtedly, factors for generating plasmon resonance are primarily considered, which is the most important selection criterion for SERS substrates. Recently, the development of silicon-based SERS surfaces has attracted the attention of researchers. Silicon-based materials exhibit highly efficient electrical conductivity, photocatalytic activity, and excellent optoelectrical properties in the visible region and have been widely explored for the fabrication of silicon-based optoelectronic devices [112,113]. Numerous techniques such as conventional electron beam lithography [114,115], photolithography [116], metal-assisted chemical etching [117] etc. are now available to fabricate various shapes (especially NPs) for their next use as SERS substrates. Currently, the possibility of mass-production large areas of low-cost nanostructured SERS substrates with a large number of hot spots and thus suitable Raman enhancement is one of the main goals in the industry for SERS substrates. Developments in this area will

reduce the cost of SERS research and enable a broad application of this method in routine research.

One of the new developments is nanostructured silicon coated with a noble metal as a SERS substrate. Initially, nanostructured Si surfaces were used as a material for solar panels, but in 2009 Talian et al. [118] used the bSi substrate covered with an Au layer (without an adhesive layer) for SERS detection of Rhodamine 6G (R6G) molecules. The results showed that this development makes it possible to produce cost-effective and stable substrates for SERS research. In 2020, a protocol for cleaning this type of substrate was developed [119], and this practice allows researchers to avoid single use and to reduce the cost of research.

1.6 Raman/SERS technique for investigation of peptide

The discovery of the Raman effect and advances in the development of the technical component have led to Raman spectroscopy becoming one of the most sought-after methods for the study of various classes of molecules, including complex biological molecules such as nucleic acids, proteins, lipids, carbohydrates, etc. [44]. The possibility of studying substances without carrying out long-term and specific sample preparation makes it possible to use this method to study the selected class of substances – peptides – under their natural conditions. The main characteristics of peptides such as the amino acid sequence, the secondary/tertiary structures, the conformation of the molecule, the state of the charged groups, etc. are unique for each individual peptide, and therefore each molecule generates its own unique (signature) Raman spectrum. Despite the complexity of Raman spectra, several unique marker regions of bands can be identified for peptides, the most important of which are presented below.

An essential feature of any peptide is the formation of an amide bond (CO–NH) between different amino acid residues when a sequence is created. And the most characteristic bands are associated with the CO–NH group, which are called the Amide I and Amide III regions, and their position in the spectrum can be used to determine the secondary structure of the peptide. The Amide I region is located in the range of 1580–1700 cm^{-1} and is mainly associated with the C=O stretching vibration [120,121]. It is not affected by the side chains and is extremely sensitive to the conformation of the backbone and the types of secondary structures. For example, when the backbone has a main α-helix conformation, the Amide I band is located at 1640–1655 cm^{-1} [122], if the main is β-sheet, Amide I appears at 1630–1635 cm^{-1} or 1660–

1670 cm^{-1}, and in the case of random coil conformation the characteristic vibrational feature is located in the range of 1670–1680 cm^{-1} [123]. The Amide III region (1230–1400 cm^{-1}) is characterized by –CN stretching vibrations coupled with –NH bending vibrations of the amino chain, and it is also very sensitive to the backbone conformation. The Amide III region is very sensitive to H-bonding and can be used to study changes in the strength of hydrogen bonding of the backbone. In the process of replacing hydrogen atoms with deuterium, the peak shift in the Amide III region is used to determine the state of the hydrogen bonds in the chain [120].

In addition to the secondary structure, different Raman bands were also identified for different side chains and disulfide region. One of the important amino acid residues is Cysteine, which is characterized by the presence of a free S–H group. This group exhibits a characteristic peak in the region of 2550 cm^{-1} (S–H stretching vibration) and 940 cm^{-1} (–SH bending vibration), which is an indicator of the state of this part of the molecule. Upon formation of a disulfide bridge, a characteristic peak appears in the range of 507–520 cm^{-1}, which describes the S–S stretching vibrations [124]. Additionally, the position of the above band can describe the conformation of the –CCSSCC– moiety in peptides. The classical gauche-gauche-gauche (GGG) conformations have an S–S stretching band at 508 cm^{-1}, while with a different gauche-gauche-trans (GGT) conformation, the band shifts and appears at 520 cm^{-1} [124,125].

When studying the spectra of peptides, special attention should be paid to the amino acid residues that contain aromatic parts – Tryptophan (Trp), Tyrosine (Tyr), and Phenylalanine (Phe). These amino acids have quite characteristic peaks which describe the vibrations of the benzene, phenyl and indole rings. The most important are: 621 cm^{-1} Phe (ν_{6b}) [in-plane ring deformation vibrations], 758 cm^{-1} Trp (ν_{18}) [phenyl/pyrrole in-phase ring breathing], 1012 cm^{-1} Phe/ Trp (ν_{16}) [phenyl and pyrrole rings oop-breathing], 1117 cm^{-1} Tyr (ν_{15}) [indole ring bending], 1205 cm^{-1} Phe (ν_{7a}) [ν (C–C)] and/or Tyr [δ (C–H)], [$\nu(C_6H_5–C)$], 1582 cm^{-1} Phe (ν_{8b}) and/or Trp (ν_2) [ν(C–C)]. Additionally, the position of the peaks in the 1340–1360 cm^{-1} region is characterized by the Fermi resonance between a fundamental band of in-plane N_1=C_8 vibration of the indole ring of Trp. The ratio of the intensity of Trp doublet ($I_{1360/1340}$) changes with the polarity of the solvent and can be used in the description of the tertiary structure of the peptide [126]. The Miura research group has shown that the $I_{1360/1340}$ ratio is 0.65–0.93 for hydrophilic solvents (methanol, dimethyl sulfoxide, acetonitrile, etc.) and that increasing of ratio associated with more hydrophobic solutions (1.1 for benzene and toluene and 1.23–1.32 for hexane and cyclohexane) [127]. The specific peak position of the hydroxyl group of Tyrosine makes it possible to determine the

state of the –OH group, which can indicate the environment of the molecule, the formation of hydrogen bonds and the charge of the hydroxyl group. Exposure to hydrophobic/hydrophilic environments of Tyrosine side chains can be determined by the characteristic Tyr doublet, the ratio of peaks in the region of 830–850 cm^{-1}. At a certain ratio of $I_{851/830}$, it can be assumed whether this group is located in a hydrophilic or hydrophobic environment [123,128].

2. MATERIALS AND METHODS

Materials

Human Urotensin II (U-II, $C_{64}H_{85}N_{13}O_{18}S_2$, Mr = 1388.57), 4-mercaptobenzoic acid (4-MBA, $HSC_6H_4CO_2H$, Mr = 154.19), silver nitrate ($AgNO_3$, > 99%), sodium citrate (Na_3Cit, $C_6H_5Na_3O_7 \cdot 2H_2O$, > 99%), diethylene glycol (diEG, $C_4H_{10}O_3$, > 99%), C_2H_5OH, NaCl, KCl, NaH_2PO_4, Na_2SO_4, $NaClO_4$, NaOH were purchased from Sigma-Aldrich GmbH (Germany) – Merck. The Millipore purified water (18 MΩ cm) was used in all procedures. The stock solution of U-II is 10^{-3} M (H_2O), 4-MBA is 10^{-3} M (C_2H_5OH). The stock solution of U-II was stored at –20 °C for no longer than 3 months. For the EC-SERS measurements, the stock solution of U-II was diluted either with a solution containing 0.01 M NaH_2PO_4 and 0.1 M Na_2SO_4 or with a solution containing 0.01 M NaH_2PO_4 and 0.1 M $NaClO_4$. The pH of the solutions was adjusted to pH 7 with NaOH.

Methods of fabrication of SERS surfaces

a) silver nanoparticles (Ag NPs)

First, a 50 mL solution containing 1 mM $AgNO_3$ was boiled for 10 min. Next, 1 mL of 1% Na_3Cit and 2.5 mL of diEG were added. The mixture was refluxed using an IKA RCT Basic magnetic stirrer for 40 min. Then it was cooled to room temperature in a cold-water bath (about 1 hour), and a green-yellowish suspension of silver nanoparticles (Ag NPs) occurred. For characterization of Ag NPs, HR-TEM microscopy was utilized to analyze the morphology of the produced nanoparticles. For the analysis, a Tecnai F20 X-TWIN microscope equipped with an EDX spectrometer and a Gatan Orius CCD camera was used. UV absorption measurements were performed on the Peak Instruments UV-Vis spectrophotometer C-7200S in the 200–1300 nm range. Synthesized Ag NPs were held at low temperatures (8–10°C) and centrifuged (20 min, 3500 rpm) before being used in experiments. The Ag nanoparticles are suitable for use for 2 weeks from the date of manufacture.

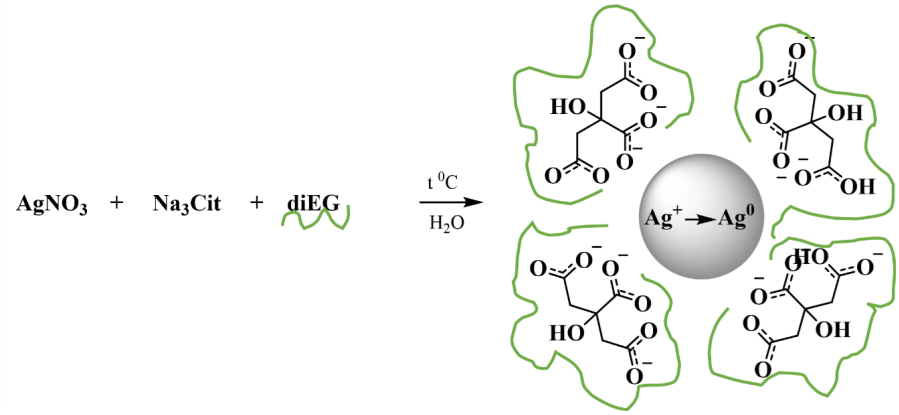

Figure 8. Scheme of the syntheses of Ag NPs [129].

b) silver electrode for EC-SERS

First, the Ag electrode was polished with soft sandpapers (P1000 and P2500 respectively) and a 0.05 μm alumina slurry (Stuers, Denmark) to refresh the surface. After that electrode was sonicated in a water/ethanol mixture (1:1) for 10 minutes and then immersed in an acetone solution for 5 minutes. Next, the Ag electrode was roughened in 0.1 M NaCl solution, initially pre-reduced for 3 min at –1.0 V, where by five oxidation-reduction cycles were carried out in the potential range between 0.44 V and –0.44 V with a 100 mV/s scan rate with pauses of 30 s for the positive and 30 s for the negative potentials. Finally, the electrode was rinsed with Millipore purified water and transferred to the electrochemical cell, where (WE) – Ag electrode; (CE) – Pt wire; (RE) – Ag/AgCl filled with 3M KCl. Volume of the cell – 1 mL. The measurements were carried out in an electrochemical cell in backscatter mode.

c) Black silicon substrate (bSi)

The single-side polished 2-inch silicon wafers (p-doped, <100>) with a thickness of 275 ± 25 μm and a bulk resistivity of 1–30 Ohm·cm were used to create the black silicon substrate. Prior to manufacture, the wafer surface was pre-cleaned using acetone and isopropyl alcohol in an ultrasonic bath set at 60 W/20° C for 10 and 5 minutes, respectively, to remove any impurities. On the next step, wafers were treated with oxygen plasma for 2 min at 20 sccm flow rate and at a radio frequency (RF) power of 150 W with Plasma-Etch setup (PE-50, Plasma Etch Inc.; Carson City, NV, USA). The bSi surfaces were fabricated through the cyclic Bosch process according to method described in

[130] with some modifications: the step of C_4F_8:SF_6 deposition (masking) was excluded, the etching was done with SF_6:O_2 ratio of 10:9 with a gradual decrease of SF_6 (10, 9, 8, 7, 5 sccm) after each 5 min. The surface structures of bare bSi wafers were analyzed using a Zeiss LEO 1550 scanning electron microscope (InLens detector, acceleration voltage 5 kV).

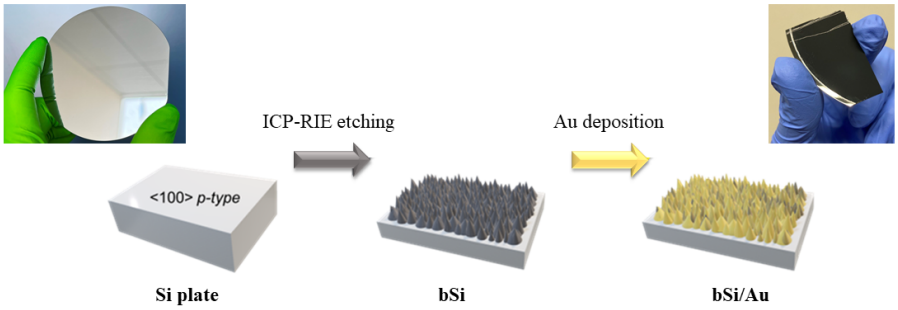

Figure 9. Scheme of the syntheses of bSi/Au substrate.

Before gold layer deposition, the bSi substrates were rinsed with ethanol for 10 min, cleaned in deionized water, and dried in a N_2 flow. For the gold deposition a physical vapor deposition (PVD) system was used (Leybold Inficon Vacuum system, GmbH). Dual vacuum pumps were used: Trivac 16/25 B oil sealed vacuum pump (medium vacuum), Turbotronik NT 151/361 turbo pump (high vacuum). Vacuum monitoring was provided by Combivac CM 31 (INFICON, Germany). A 150 nm gold layer was deposited directly on the bSi structures in a high vacuum environment ($8*10^{-6}$ Torr) with 0.2 nm/s evaporation rate. For deposited mass monitoring Quadruvac PGA 100 mass spectrometer (INFICON, Germany) was used. The morphological analysis of the obtained structures was done using a Helios NanoLab 650 model microscope (FEI. Netherlands) with a nominal beam voltage of 3 kV. ImageJ software 24 was used to estimate the dimensions of bSi structures.

These substrates were provided for research by colleagues from the University of Eastern Finland (Joensuu, Finland) under the guidance of Prof. Polina Kuzhir.

Raman/SERS measurements

The Raman and SERS measurements were carried out on a RamanFlex 400 spectrometer (Perkin-Elmer, USA) equipped with a thermoelectrically cooled (–50° C) charge-coupled device (CCD) detector and fiber optic cable for excitation and collection of the spectra (excitation wavelength 785 nm).

The laser beam was focused on a 200 μm diameter spot. Laser power at the sample was 100 mW for Raman measurements, and 30 mW – for SERS, 60 mW– for EC-SERS, 16,8 mW – for SERS measurements on bSi/Au substrate; integration time was 500 s for Raman, 300 s – for SERS and 300 s – for EC-SERS measurements.

Raman spectra were recorded from the powder of human U-II peptide. Raman wavenumbers were calibrated according to the polystyrene sample standard spectrum.

For the SERS measurement, 2 μl of U-II solution (10^{-3} M in H_2O) was mixed with 2 μl of Ag NPs in the test tube. Next, 2 μl of the new suspension was dropped onto a Tienta steel substrate and allowed to dry completely at room temperature. The SERS spectra of the U-II with Ag NPs was obtained. To demonstrate the washing effect, the dry sample of U-II/Ag NPs was washed in the steam of Millipore purified water for 5 s, dried under a stream of N_2 and an additional SERS spectra were recorded.

The SERS measurements U-II on bSi/Au substrate were recorded from the solution of human U-II peptide with electrolyte − 0.1 M Na_2SO_4 and 0.01 M NaH_2PO_4 at physiological pH values (pH 7). The final concentration of U-II peptide molecules is 10^{-5} M.

The EC-SERS measurements U-II on Ag electrode were recorded in the range of potentials from –1.0 to 0.0 V in the anodic direction with 0.2 V increments. After the preparation of the EC-cell an open circuit potential (OCP) spectrum of U-II peptide solutions was measured to ensure that the U-II peptide molecules reach the electrode surface, and the SERS signal can be detected in the absence of an applied potential in the system. Next, prior to the EC-SERS measurements, the potential of the Ag electrode was changed twice in the potential range from 0.1 V to –1.0 V with pauses of 5 min for the positive and 5 min for the negative potentials. After that the EC-SERS measurements started immediately. All measurements provided in the solutions of electrolyte − 0.1 M Na_2SO_4 or 0.1 M $NaClO_4$ and 0.01 M NaH_2PO_4 at physiological pH values (pH 7). The final concentration of U-II peptide molecules is 10^{-5} M.

Electrochemical measurements of system bSi/Au − 4-MBA were carried out in a constructed cell with a quartz circular window, arranged with a working electrode (bSi/Au), placed in a specially produced Teflon construction (Fig.10). Pt wire was used as counter electrode, and 3M Ag/AgCl/KCl electrodes were used as reference electrodes. Cell volume is 400 μl. Before experiment, the bSi/Au substrate was rinsed by Milipore water and ethanol and additionally treated with air plasma (PDC-002, Harrick Plasma Inc.; Ithaca, NY, USA) at the 30W power for 5 min. After plasma,

bSi/Au substrate was cleaned electrochemically in 0.1 M Na_2SO_4 (H_2O), stable potential was kept at −0.9 V for 10 min.

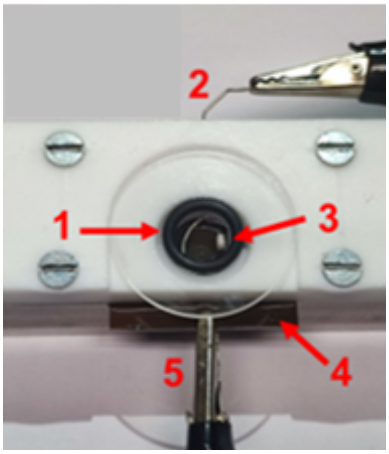

Figure 10. The photo-scheme of the EC-SERS cell. 1. bSi-Au plate (WE); 2. Platinum wire (CE); 3. 3M KCl-saturated Ag/AgCl (RE); 4. Outer part of bSi/Au for contact; 5. Contact bSi/Au.

For the EC-SERS measurements, the self-assembled monolayer (SAM) of 4-MBA was deposited by mounting the bSi/Au substrate in 4-MBA stock solution ($C=10^{-3}$ M) for 18 h. The EC-SERS measurements of 4-MBA SAM were performed in aqueous solution containing 0.1 M Na_2SO_4.

Data processing

Spectral analysis was performed by using Origin software. Raman spectra were corrected by polynomial function background subtraction. The spike removal was done as described in [131]. Background Raman spectrum of 0.1 M Na_2SO_4 or 0.1 M $NaClO_4$ containing 0.01 M NaH_2PO_4 was subtracted from SERS spectra of U-II on Ag electrodes and SERS spectra of U-II on bSi/Au substrate. The smoothing procedures were performed by Savitzky-Golay method by applying the third order polynomial function in the eleven-point window.

DFT simulations

Computational analysis was performed using the Gaussian 09 program for Windows [132]. The structure was optimized, and vibrational frequencies were determined using the DFT/B3LYP approach. The 6-311++G (2d, p)

basis set was set for C, H, S, and O atoms, and LANL2DZ with ECP basis set was applied for the Au_4 atomic cluster (Fig. 11). The obtained vibrational frequencies and intensities were adjusted using a scaling method detailed in previous studies [133].

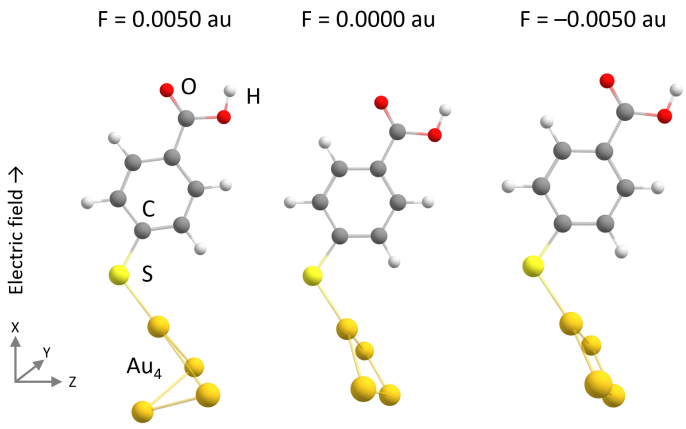

Figure 11. Optimized geometry of Au_4-4-MBA complex calculated at DFT/B3LYP theory level using 6-311++(2 d,p) basis set for C, H, O, and S atoms and LanL2DZ basis set or Au. The complex is oriented so that the Au–S bond is tilted by approximately 30° from the X-axis.

No imaginary frequencies were found. We utilize a consistent, bipolar external electric field aligned along (positive) and in opposite (negative) directions to the x-axis as shown in Figure 11. Field strength is expressed in atomic units (a.u.), where 1 a.u. equals to 51.42 V/Å.

3. RESULTS AND DISCUSSION

3.1 Raman spectra of Urotensin II peptide

At the first stage of research of the U-II molecule, the Raman spectrum of a pure substance was obtained [134]. The U-II peptide molecule consists of 11 amino acids (AA): Glu, Thr, Pro and Asp at the N-terminus, the cyclic part formed by c–[Cys–Phe–Trp–Lys–Tyr–Cys], which is bridged by a disulfide bond between Cys^5 and Cys^{10}, and Val, at the C–terminal end. Since the molecule is most often in a closed conformation due to a strong S−S bond between two Cysteine AA residues, the aromatic AA residues such Phe, Trp, Tyr are localized towards the environment, which may contribute to the dominance of the signal from these residues in the Raman spectrum. The Raman spectrum of the powder of U-II peptide in the fingerprint spectral regions of 400–1800 cm^{-1} is shown in Figure 12. According to past research on the vasopressin/Neuromedin B superfamily peptides and other small proteins [111,135–137], the assignment of the bands occurring in these spectra to their normal coordinates proposed in the Table 1.

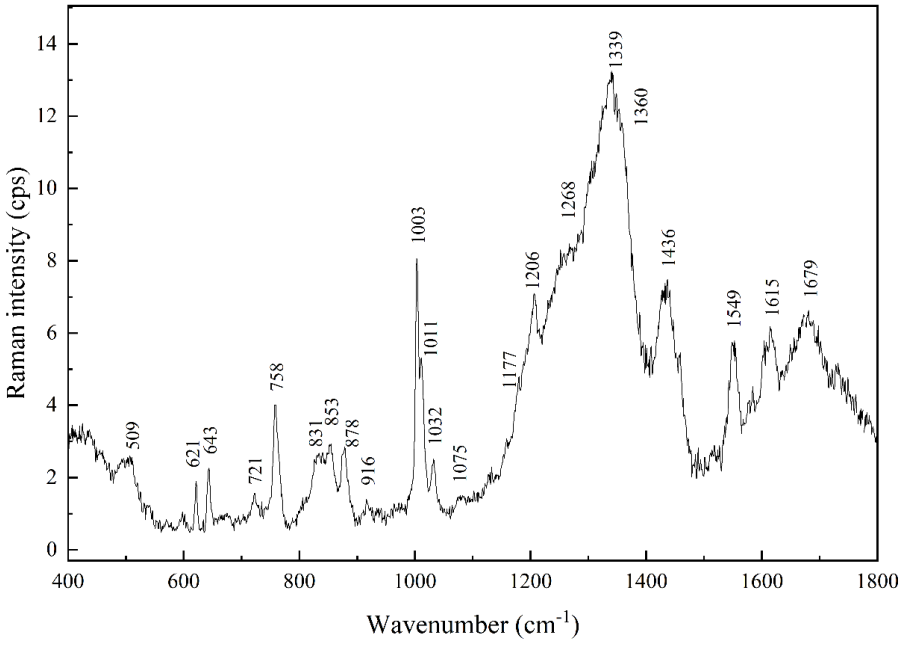

Figure 12. Raman spectrum of U-II peptide in the solid state. Excitation wavelength 785 nm, laser power 100 mW, integration time 500 s.

As expected, the Raman spectrum of the U-II molecule is dominated by characteristic bands of the vibrations of the aromatic AA from the cyclic part of the peptide. The characteristic bands of other amino acids are less observed in the Raman spectrum. The main bands at 1003 cm^{-1} (ν_{12}), 1032 cm^{-1} (ν_{18a}), 1206 cm^{-1} (ν_{7a}) assigned to the Phe residue [111]. The Trp characteristic bands located at 758 cm^{-1} (ν_{18}), 1011 cm^{-1} (the phenyl/pyrrole rings oop breathing modes), 1436 cm^{-1}, 1549 cm^{-1} (ν(C=C)), 1615 cm^{-1} (stretching of benzene and indole rings) [136]. Also, a band at 1339 cm^{-1} and an adjected shoulder at 1360 cm^{-1} suggests the Trp doublet. The characteristic vibrations of Tyr are doublet at 831 cm^{-1} and 853 cm^{-1} (Fermi resonance) [137,138], and ring vibrations at 1206 cm^{-1} (which overlap with Phe (ν_{7a})) [139].

The spectrum consists of the characteristic band of the stretching vibration ν(S–S) of the disulfide bond (509 cm^{-1}) which confirms the fact that the molecule is in a closed conformation. According to the [140–142] the position of this band in the spectrum is associated with the gauche-gauche-gauche (GGG) conformation of the S–S bond.

The important characteristic bands of Amide I with a maximum at 1679 cm^{-1} and Amide III in the range of 1230–1270 cm^{-1} are presented in the Raman spectrum of the U-II peptide [137,143]. The position of the Amide I and Amide III bands is normally used as an indicator of the secondary structure of the peptide [144]. According to Haensele [3], conformational studies using ^{1}H-NMR have not shown a secondary structure of U-II in aqueous solutions. In the membrane-mimetic sodium dodecyl sulfate micelles, the cyclic region was hypothesized to exhibit a canonical type II'β-turn from Phe to Tyr [11].

At the same time, the location of the Amide I maximum at 1679 cm^{-1} and the Amide III at 1268 cm^{-1} suggests that the U-II peptide in the powder is in a disordered state. We speculate that this is due to the mixture of conformers of the U-II peptide in the powder.

3.2 SERS research of U-II using silver nanoparticles

The first SERS investigation of Urotensin II peptide was performed using silver nanoparticles (Ag NPs), synthesized by reflux method described above [129]. This type of synthesis allows obtaining particles of a sufficiently large size, which subsequently contributes to the enhancement of the Raman signal. The main reducing components as citrate, borohydride or polyol can be used in the synthesis, and additional surface stabilizers (oleylamine, polyethylene glycol) or capping agents (cetrimonium bromide (CTAB),

polyvinylpyrrolidone (PVP)) propose the size- and shape-controlled synthesis of nanoparticles.

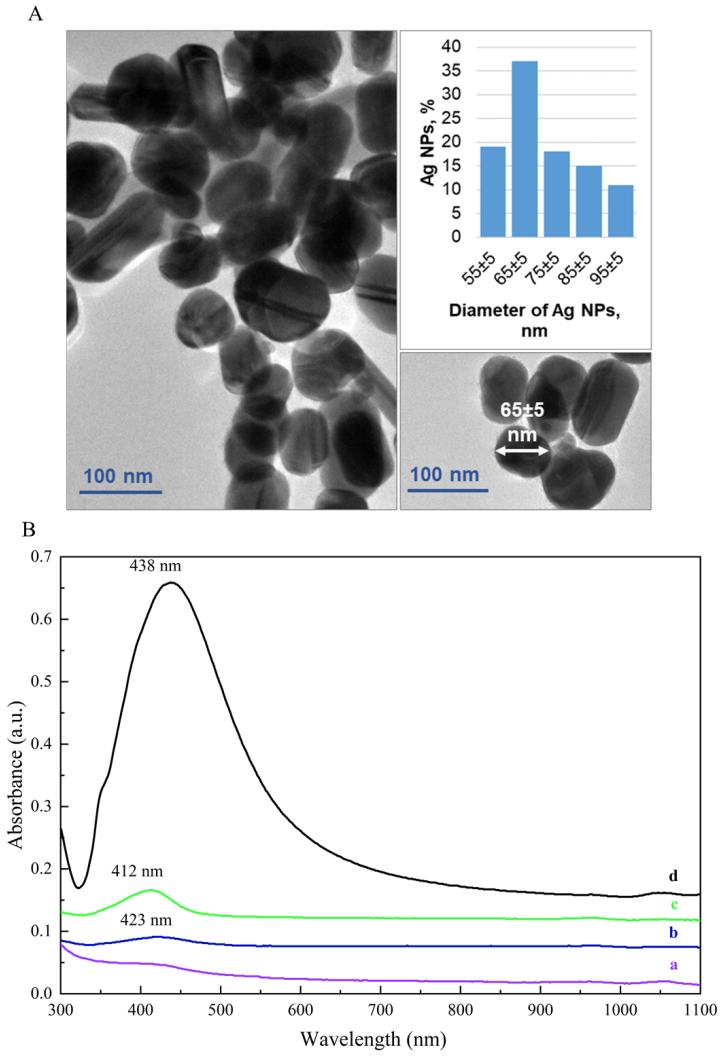

Figure 13. (A) HR-TEM data of Ag NPs, (B) UV-Vis spectra of Ag NPs synthesized with polyols: polyEG (a), pentaEG (b), tetraEG (c) and diEG (d).

Such a variety of agents makes it possible to obtain particles with the desired properties and some differences in physical parameters. Polyols as glycerol (GLY), ethylene glycol (EG), polyethylene glycol (poly-EG), propanediol (PDO) are widely used in the synthesis of nanoparticles and allow synthesis in an aqueous medium and propose additional stabilization of particles. Various stabilizing agents allow control over the shape of particles,

allowing them to grow to the required size, but large quantities of molecules of stabilizers can create difficulties in obtaining the SERS spectrum of the studied molecules.

In the synthesis of Ag nanoparticles, a large particle size and a minimal signal in the Raman spectrum from the components of nanoparticle synthesis were selected as the main necessary parameters for further SERS studies of Urotensin II. For this purpose, polyols with a minimum size were selected – diEG, tetraEG, pentaEG and polyEG200 for comparison. During the synthesis of particles in various stabilizers, the particle size was estimated using the UV-Vis method, and the average particle size can be estimated by signal amplification and peak position. Figure 13 shows HR-TEM data with particle size distribution (A) for synthesis using diEG and the absorption of particles (B) when using various stabilizers. A comparison of various ethylene glycol derivatives showed that the use of diEG allows obtaining the largest particles with the least amount of polyols (Fig. 13B) and this agent was used in the futured synthesis of Ag NPs.

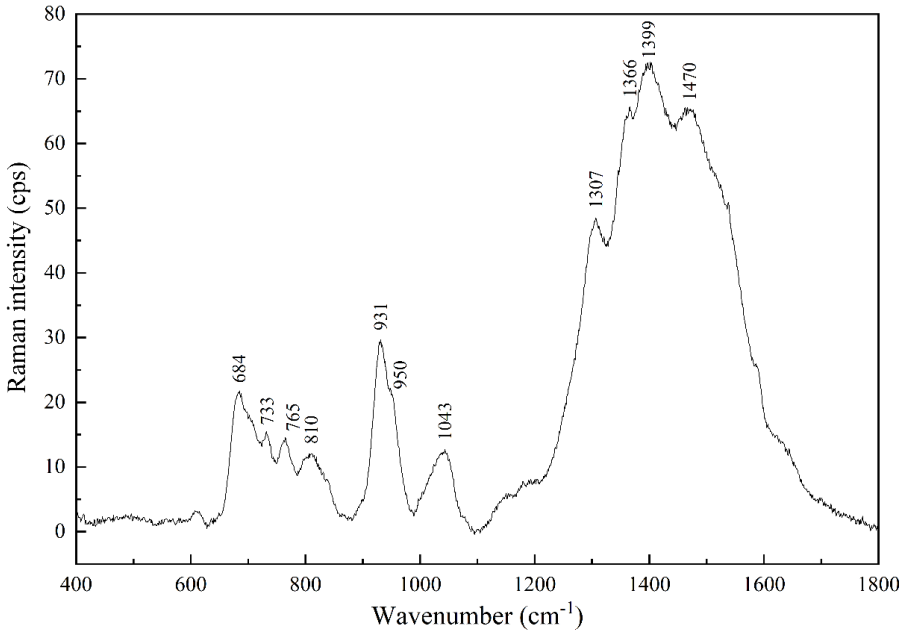

Figure 14. SERS spectrum of Ag NPs. Excitation wavelength 785 nm, laser power 30 mW, integration time 300 s.

Silver nanoparticles without any additional layer (shell) had approximately size 65 ± 5 nm and sodium citrate and diethylene glycol were used as reducing and capping agents, respectively. Silver nanoparticles have

their own SERS spectrum, which is characterized by vibrational bands mostly belonging to necessary chemical components (reducing and capping agents). The SERS spectrum of the pure Ag nanoparticles is shown in Figure 14.

The SERS spectrum of Ag NPs present the main vibrations assigned to the diEG and Na_3Cit. The two vibrational bands at 1043 cm^{-1} and 1470 cm^{-1} attributed to C–O stretching [145,146] and $–CH_2$ bending vibrations [145] mainly assigned to the diEG molecules. The vibrational bands at 931 and 950 cm^{-1} attributed to C–COO stretching and band at 1399 cm^{-1} characterized the symmetric stretching of the –COO group of adsorbed citrate anion on Ag NPs [147,148]. The band at 810 cm^{-1} with the slight shoulder at 840 cm^{-1} was assigned to all molecule complex vibration where C–C and C–O bonds are involved. The characteristic bands of Ag NPs assignment are presented in Table 2.

The SERS research of Human U-II using silver nanoparticles can be divided into 2 parts: first, the suspension of U-II/Ag NPs was applied on a Tienta surface and dried, after the SERS spectrum was recorded (Fig. 15A). In the second part, the dried sample was gently washed with a flow of Millipore purified water and dried anew. The SERS spectrum of cleaned samples presented in Figure 15B. Following washing, there are noticeable differences in the spectra, as well as changes in the intensity and the disappearance/shifting of some vibrational bands. The peak assignment of the main characteristic bands of U-II peptide on Ag NPs presented in Table 1.

Table 1. Peak assignment of the main characteristic bands of Raman and SERS of U-II peptide on Ag NPs [136,139,143,144,149–152].

Wavenumber, cm^{-1} **Raman**	Wavenumber, cm^{-1} **SERS**	Assignments
509	509	ν (S–S)
621	621	Phe [in-plane ring deformation vibrations]
643	642	Tyr [δ (CCC)]
—	680	ν (C–S), P_C–G
721	721 sh	ν (C–S), P_C–T
758	757	Trp [phenyl/pyrrole in-phase ring breathing]
831 sh	835	Tyr doublet [ν (C–C)]
853	850 sh	

878	878	Trp [δ (N–H) and Fermi resonance between phenyl ring breathing and out of plane ring bend overtone]
—	896	—
916	924 sh	ν (C–C)
—	951	ν (C–COOH), d (C–C) of Asp/Glu
1003	1003	Phe [ring breathing vibration]
1011 sh	1011 sh	Trp [phenyl and pyrrole ring out-of-phase breathing]
1032	1032	Phe [in-phase motion of ν (C–C)]
1075	1075	ν (C–C) alkyl chain
—	1125	Trp/Phe, ν (C–C) alkyl chain
1177 sh	1177	Tyr and/or Phe
1206	1195	Phe [side chain ν (C–C) vibration]
1268 sh	1233	Amide III
—	1297	—
1339	1346 sh	Trp doublet [pyrrole ring ν (N–C); Fermi resonance] w (CH_2)
1360 sh	1369 sh	
—	1394	Asp/Glu [ν (–COO)]
1436	—	Trp [pyrrole ν (N–C–C); δ (N–H)]
1549	1539	Trp [pyrrole ν (C=C)]
—	1591	Phe [phenyl ring bond-stretching vibrations]
1615	1615 sh	Trp [pyrrole ν (N–C)]
1679	1695	Amide I [mostly ν (C=O), small contribution from δ (N–H)] β-sheet

Abbreviations: ν – stretching; δ – bending; d – deformation; w – wagging.

The bands at 684, 733, 765, 810, 1307 cm^{-1} (Fig. 15A) assigned to the citrate anion (Table 2) are practically no longer visible in the SERS spectrum after washing (Fig. 15B), what can be said is that during adsorption, the

peptide replaces citrate on the surface of nanoparticles. Also, the wavenumbers of the bands at 924 cm^{-1} and 1394 cm^{-1} assigned to the C–COO and –COO stretching vibrations [149] also changed and shifted to lower wavenumbers, compared to the Ag NP spectrum (Fig. 14) and can be now more assigned to the vibration of Asp and Glu amino acid side chains. The rest of the bands of the uncleaned sample (Fig. 15A) located at 528, 894 and 1276 cm^{-1} may be explained as the contaminants or the unstable clusters of adsorbed peptides on Ag NPs that later have been washed out.

Table 2. Peak assignment of the main characteristic bands of Ag NPs [18,146,147].

Wavenumber, cm^{-1} **Raman**	Assignments of **NaCit**	Assignments of **diEG**
684	β (CO_2)	—
733	r (CH_2)	—
765	—	—
810	ν (C–C) or ν (C–O) all molecule complex vibr.	ν (C–C) or ν (C–O) all molecule complex vibr.
931	ν (C–COO)	—
950	ν (C–COO)	—
1043	ν (C–O)	ν (C–O)
1307	ν (C–C–O)	ν (C–C–O)
1366	ν (CO_2), s + β (CH_2) + w (CH_2)	—
1399	ν (–COO)	—
1470	—	β (CH_2)

Abbreviations: ν – stretching; β - in-plane deformation; w - wagging; r - rocking; s - symmetric.

The most intense vibrational bands observed in the SERS spectrum of U-II at 509, 621, 643, 757, 830–850, 878, 1003, 1011, 1032, 1075, 1125, 1177, 1195, 1539, 1591, 1615 cm^{-1}. The assignments of the band vibrations of the SERS spectra can be found in Table 1. The presence of Amide I and Amide III in the spectrum indicates the presence of protein, and according to their

wavenumbers and intensities, the secondary structure of protein after adsorption can be predicted.

Two low intensity bands of Amide III at 1297 and 1233 cm^{-1} and position of Amide I at 1695 cm^{-1} in the SERS spectra of adsorbed peptide (Fig. 15) could be identified as α-helix and β-turn or β-hair pin structure motifs that are present in U-II peptide [3]. Unfortunately, due to the wide gap between these two frequencies and position of Amide I at 1695 cm^{-1} of adsorbed peptide, we suggest several conformers with different secondary structure are adsorbed on the silver surface.

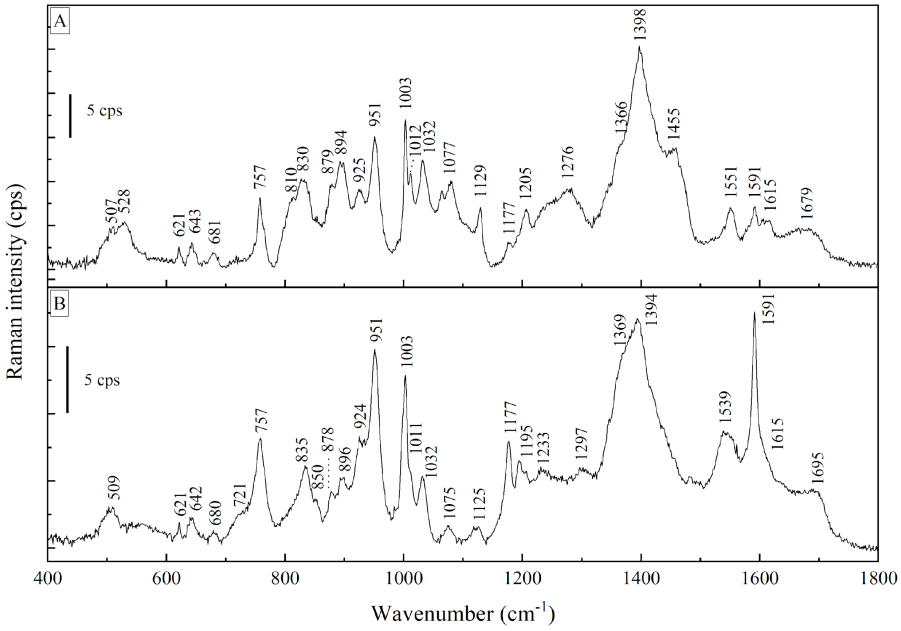

Figure 15. SERS spectra of U-II and Ag NPs suspension: before (A) and after (B) washing. Excitation wavelength 785 nm, laser power 30 mW, integration time 300 s.

In the process of describing the SERS spectrum of the U-II peptide, it becomes obvious that most of the bands belong to aromatic amino acids of the peptide (Phe, Trp, Tyr) and, in comparison with the Raman spectrum, in SERS case some changes in the position or intensities of defined bands can indicate the process of interaction cyclic part of the U-II molecule with the metal. In the Figure 15B, the appearance of an intense sharp band at 1591 cm^{-1}, assigned to the in-plane ring stretching vibration of Phe [137,141,142,152], characterizes the interaction of the phenyl ring with the Ag NPs. Compared with the Raman spectrum, intensity of the band at 1075 cm^{-1}, assigned to the

C–C stretching vibration of the alkyl chain, increases. Also, the band at 1206 cm^{-1} shifted by 11 cm^{-1}, which is assigned to ν(C–C) of the Phe side chain. Other characteristic band for Phe located at 621 cm^{-1} (in-plane ring deformation), 1003 cm^{-1} (symmetric ring breathing mode), 1032 cm^{-1} (in-plane ν(C–C) vibrations) are stable in both Raman and SERS spectra [139,143,150].

There are several vibrational bands of the Trp. Most of them, associated with the breathing vibrations of Trp rings, are observed at 757 cm^{-1} (phenyl/pyrrole in-phase ring breathing), 878 cm^{-1} (indole + δ(NH)), and 1011 cm^{-1} (phenyl and pyrrole rings oop-breathing), and their positions and relative intensities stable in Raman and SERS spectra (Fig. 12, 15) [139,143,150,153]. The N–C stretching of the pyrrole ring at 1615 cm^{-1} presents as the weak shoulder of the intense band at 1591 cm^{-1} in the SERS spectra (Fig. 15B). Also, the bands at 1339 cm^{-1} and 1360 cm^{-1}, associated as Trp doublet, present as a shoulder at 1369 cm^{-1}, and overlap with a strong band at 1394 cm^{-1} of adsorbed carboxylic groups of Asp and Glu.

A new band at 1125 cm^{-1} appeared in the SERS spectrum, which can be attributed to both Phe and Trp ν(C–C) of the alkyl chain. Compared to the Raman spectrum (Fig. 12), the most significant change associated with Trp is the red shift of the band at 1539 cm^{-1} by 10 cm^{-1} and the broadening of the 757 cm^{-1} band [153]. The recent changes may indicate that the U-II molecule interacts with the metal by adsorption of the pyrrole core of the indole ring of Trp.

The characteristic Tyr band at 642 cm^{-1}, (δ (CCC)), 830–850 cm^{-1} (Tyr doublet (Fermi resonance)), 1177 cm^{-1} (in-plane δ(C–H), overlapping with Phe) is shown in the SERS of U-II. According to [138], the ratio of the intensity of the Tyr doublet at 830 cm^{-1} and 850 cm^{-1} is the spectral marker for the protonation of the –OH group. The intensity ratios I_{853}/I_{831} = 1.08 for Raman and I_{850}/I_{835} = 0.63 for SERS. For both cases, its values are between 0.3 and 1.25, so that it can act as both a proton donor and an acceptor [18,154]. The changes in the ratio of Tyr double indicate that the state of the –OH group has changed during adsorption on Ag NPs and the adsorbed phenolic oxygen acts as a proton donor. This assumption is proved by the increased intensity of the vibrational band at 1177 cm^{-1} [143,155,156].

One of the important issues during the experiment was the question of the conformation of the U-II molecule and possible significant changes during the adsorption process. In both Raman and SERS spectra, the presence of the band at 509 cm^{-1} (ν (S–S)), confirms that U-II peptide retains its cyclic structure during adsorption process. And as was presented in [155], the position of this bond is associated with gauche conformation of the –

CCSSCC– fragment of the disulfide bridge. The same conformation also dominates in the powder of the peptide.

Additional information about conformation of the C–C bonds located near the disulfide bridge can be provided by the bands located in the range of 600–800 cm^{-1}. The different forms of the C–S bond are caused by internal rotation along the C–C axis of Cys (X—CH_2—CH_2—S, where X = C, H or N atom) [151]. Well established possible rotations isomers can be named as P_C–G, P_C–T, P_H–G, P_H–T, P_N–G, P_N–T, where G – gaushe and T – trans conformation of X atom (C – carbon, H – hydrogen, N – nitrogen) with respect to the sulfur atom. According to the [149,151], the bands at 680 cm^{-1} and 721 cm^{-1} in the SERS spectrum are assigned with the P_C–G and P_C–T conformations, respectively. In the Raman spectrum, only the band at 721 cm^{-1} is observed and associated with the P_C–T conformer.

The present study shows the SERS spectra of U-II molecules adsorbed on the surface of the Ag NPs. Due to the interaction, the S–S bond in the molecule does not break and the molecule retains its closed conformation. Compared to the Raman spectrum, the increased intensity of the band at 757 cm^{-1} (phenyl/pyrrole in-phase ring breathing), 1032 cm^{-1} (in-phase ring motion of ν (C–C)), 1075 cm^{-1} (ν (C–C) of the alkyl chain), 1125 cm^{-1} (ν (C–C) alkyl chain), and the appearance of an intense sharp band at 1591 cm^{-1}, which is assigned to in-plane ring stretching prove the interaction of the Phe and Trp with the metal.

This was summarized in the **first and second** statements of the thesis:

During the adsorption of the Urotensin II peptide on the metal surface, the disulfide bridge between the two Cysteines remains intact, and the interaction with the metal surface occurs via aromatic amino acid residues located in the cyclic part of the molecule;

During adsorption on Ag NPs, U-II displaces citrate anions from the silver surface, and during washing process, it fully replaces the washed-out citrate anions by interacting through the Asp and Glu residues.

The results presented in the Section 3.2 are summarized in 2 scientific articles: E.Daublytė, M.Kalnaitytė, **A.Klimovich**, A. Drabavičius, T. Charkova. Synthesis of silver nanoparticles with polyols under reflux and microwave irradiation conditions**.** *Chemija, 2023, 34, 3, 113–122*. DOI: 10.6001/chemija.2023.34.3.1.

A.Klimovich, T.Charkova, I.Matulaitienė. Characterization of the Urotensin II peptide by SERS using silver nanoparticles. *Journal of Raman Spectroscopy, 2025,* DOI: 10.1002/jrs.6800.

3.3 EC-SERS research of U-II using Ag electrode

3.3.1 EC-SERS measurements performed in a buffer containing Na_2SO_4

Figure 16 shows the SERS-spectra of U-II peptide molecule (C = 10^{-5} M) adsorbed on the Ag electrode surface, measured in a solution containing 0.1 M Na_2SO_4 and 0.01 M NaH_2PO_4 at physiological pH values (pH 7.0). The composition of the solution was selected based on the previous work of our colleagues [139,143,150] and corresponds to the classical composition of the physiological phosphate buffer solution. The SERS spectra were recorded in the range of potentials from –1.0 to 0.0 V in the anodic direction with 0.2 V increments. Prior to the EC-SERS measurements, an open circuit potential (OCP) spectrum of U-II peptide solutions was measured to ensure that the U-II peptide molecules reach the Ag electrode surface, and the SERS signal can be detected in the absence of an applied potential in the system.

The band assignment of the OCP and EC-SERS spectra was based on the data of EC-SERS measurements of small peptides with similar structure (peptides of the bradykinin and bombesin subfamily containing Phe-, Tyr-, Trp- AAs) adsorbed on silver, gold and copper electrodes or measured with silver nanoparticles [111,137,153,157,158]. The wavenumbers of all the enhanced bands in EC-SERS spectra and their assignments based on prior studies are listed in Table 3.

All SERS spectra are characterized by bands originating mainly from Phe, Trp and Tyr – three of four AA residues that form a hydrophobic site of the U-II peptide, although at negative potentials peptide reorientation occurs and Lys also reaches the Ag electrode surface (discussed below).

Under the conditions of applied potential of –1.0 V, the following characteristic bands of Phe are present in the U-II SERS spectrum: a weak in-plane bending mode at 621 cm^{-1} (ν_{6b}) and strong bands at 1002 cm^{-1} (ν_{12}, symmetric ring breathing), 1030 cm^{-1} (ν_{18a}, in-plane C–H bending), 1205 cm^{-1} (ν_{7a}), quadric stretching modes at 1582 cm^{-1} (ν_{8b}) and 1605 cm^{-1} (ν_{8a}). Except for the weak band at 621 cm^{-1}, the intensities of practically all characteristic vibrations of Phe are significantly enhanced at the negative potential of the Ag electrode and decrease monotonically with the change of the applied potential from –1.0 V to 0.0 V (see Fig. 17A).

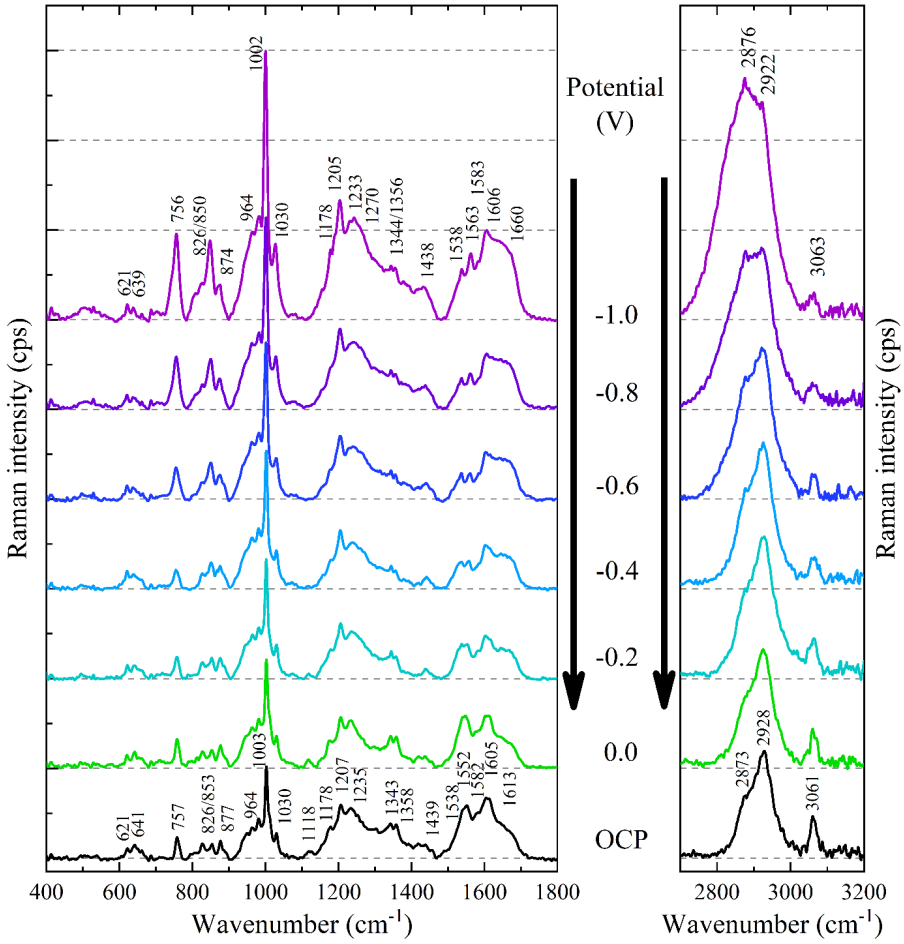

Figure 16. The dependence of the SERS spectra of the U-II solution on the Ag electrode potential, shown in the spectral ranges (A) 400–1800 cm^{-1} and (B) 2700–3200 cm^{-1}. The solution contains 0.1 M Na_2SO_4, 0.01 M NaH_2PO_4 (pH 7.0) and 10^{-5} M U-II peptide. Excitation wavelength 785 nm, laser power 60 mW, integration time 300 s.

A monotonic decrease in the intensity of the bands at 1582 cm^{-1} (ν_{8b}) and 1605 cm^{-1} (ν_{8a}) is observed when the applied potential is shifted from –1.0 V to –0.4 V. Moreover, the band ν_{12} undergo a shift from 1003 cm^{-1} under OCP to 1002 cm^{-1} at –1.0 V. The latter may indicate physical interaction of the Phe ring with the Ag surface and a generally vertical orientation of the ring relative to the electrode surface. Significant enhancement of the main Phe modes (ν_{12}, ν_{18a}, ν_{7a}, ν_{8a}, ν_{8b}) likely support this hypothesis. The non-monotonic behavior of the normalized intensity of the band at 621 cm^{-1} is probably due to poor

signal-to-noise ratio as the intensity of this band is low and thus this trend is not statistically significant.

Strong characteristic bands of the Tyr residue are also enhanced under the conditions of the applied potential (Fig. 16), which is in agreement with other SERS studies showing a strong interaction of the Tyr residue with the surface of Ag electrode [159]. The spectra contain the bands of the deformation vibrations δ(CCC) at 641 cm^{-1} (ν_{6b}), a doublet 826/850 cm^{-1}, which arises from Fermi resonance of the overtone of the out-of-plane bending mode $2\nu_{16a}$ and the symmetric ring-breathing fundamental mode ν_1, respectively, and the in-plane C–H bending at 1178 cm^{-1} (ν_{9a}). The band at 1207 cm^{-1}, which is often assigned to the C_6H_5–C stretching vibration [160], overlaps with the ν_{7a} vibration of Phe at 1205 cm^{-1}, and the in-plane ring stretching modes $\nu_{8a,b}$ of Tyr at 1615 cm^{-1} also overlap with the ring vibrations of Phe [159], which complicates the unambiguous assignment. The normalized intensity of ν_{6b} at 641 cm^{-1} increases with the stepwise change in applied potential from –1.0 V to 0.0 V, while other bands undergo a significant decrease in intensity (Fig. 17B). The change in the intensity ratio of the Tyr doublet I_{850}/I_{826} reflects the state of the phenolic hydroxyl group of the Tyr residue in the U-II molecule [138]. At negative potentials as compared to 0.0 V and OCP conditions, the Tyr doublet is characterized by significantly enhanced intensities of both ν_1 (850 cm^{-1}) and overtone $2\nu_{16a}$ (826 cm^{-1}). The high intensities of the doublet at –1.0 V indicate that Tyr approaches the electrode surface and likely reaches it while at 0.0 V and under OCP conditions the Tyr residue reorients and the interaction of Tyr with the electrode is weaker (Fig. 17B). The I_{850}/I_{826} ratio changes from 2.22 at negative potentials to 0.98 at 0.0 V and under OCP (Fig. 18, green curve). According to [138], this suggests that at negative potentials the phenolic hydroxyl group acts as an acceptor of strong H-bonds. The Lys residue ($–NH_2$) may likely serve as a donor of these bonds as it also approaches the electrode surface (discussed below). However, the bonding of the phenolic hydroxyl group of the Tyr to the electrode surface (O–H···Ag) could not be excluded [149]. Under OCP conditions the intensity of $2\nu_{16a}$ is increased as compared to ν_1 which indicates deprotonation or, at least, the partial negative charge on the phenolic oxygen atom (i.e. the phenolic hydroxyl group is ‘ionized’), and the group acts as a hydrogen donor [138]. It can be hypothesized that the U-II peptide binds to the Ag surface under OCP and at 0.0 V via the phenolic oxygen of Tyr after losing the hydrogen atom, as shown in [139]. Although the pK_R of Tyr is 10.07 and deprotonation of the hydroxyl group seems unlikely under the measurement conditions (pH 7.0), the pK_R decreases when the interaction with metals occurs [159]. Furthermore, the potential of –0.9 V

under our experimental conditions corresponds to a zero-charge potential (ZCP) of the Ag electrode, indicating that at more positive potentials (e.g. 0.0 V or OCP) the charge of the Ag electrode is positive and an electrostatic interaction of the deprotonated phenolic hydroxyl group with the electrode surface is quite likely [143,159].

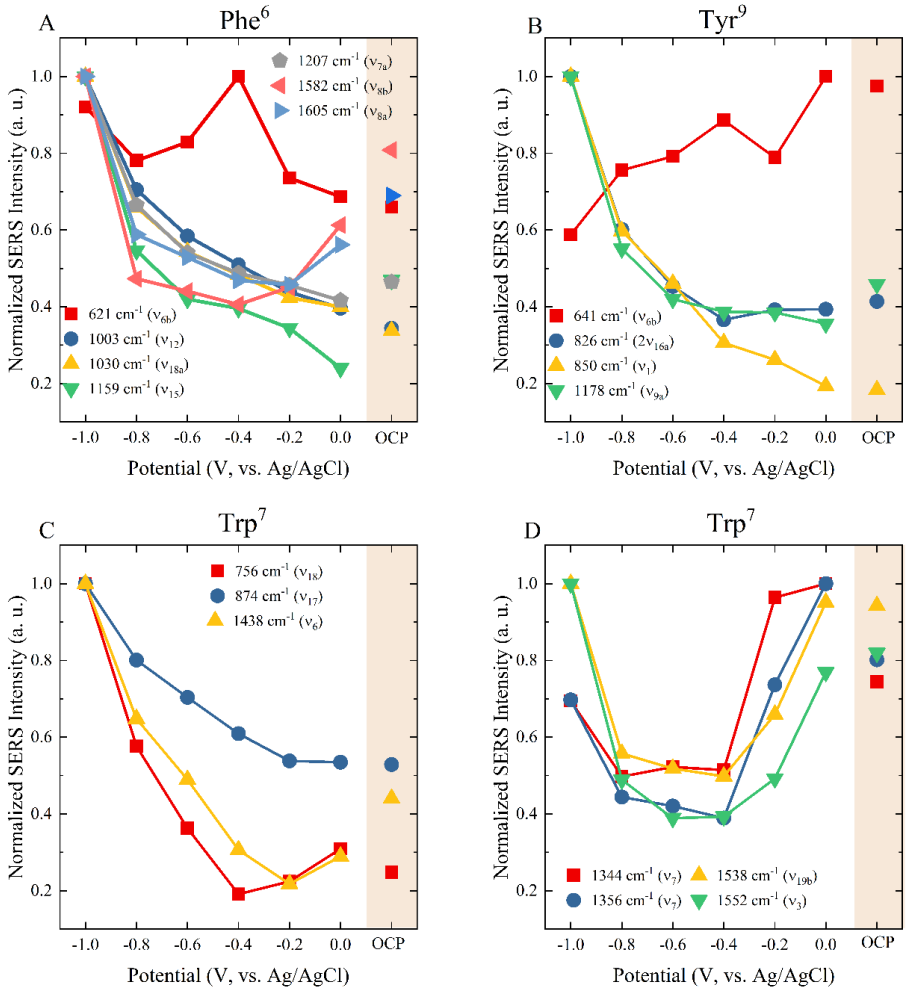

Figure 17. The dependencies of the normalized intensities of characteristic bands of (A) Phe, (B) Tyr and (C, D) Trp residues of U-II on the applied potential in the solution containing 0.1 M Na_2SO_4 and 0.01 M NaH_2PO_4 (pH 7.0).

The vibrations of the Trp residue contribute significantly to the SERS spectra of U-II, both under the conditions of negative applied potentials and

under OCP. It is worth noting that the normalized intensities of virtually all bands exhibit a U-shaped trend when the applied potential changes from –1.0 V to 0.0 V (Fig. 17 C, D). The coincidence of the intensities at 0.0 V and under OCP indicates that the spacing and orientation of the Trp of the U-II peptide do not change under these conditions. The indole ring-breathing mode at 756 cm^{-1} (ν_{18}), the band assigned to Fermi resonance between phenyl ring breathing and out-of-plane ring bending overtone at 874 cm^{-1} (ν_{17}), the Trp doublet at 1344/1356 cm^{-1} (Fermi resonance), 1438 cm^{-1} (ν_6), 1538 cm^{-1} (ν_{19b}) and 1552 cm^{-1} are significantly enhanced at negative potentials, and undergo decrease when the potential changes in the anodic direction (Fig. 17 C, D). Under 0.0 V or OCP, the intensities of ν_7, ν_{19b} and ν_3 are restored back to the intensities observed at –1.0 V (Fig. 17D). The significant drop in the intensities of these bands at the potentials (–0.8; –0.4) V indicates that the rearrangement of the indole ring relative to the Ag electrode surface occurs. The entire process of reorientation of Trp relative to the Ag surface can thus be described in the following phases: (i) under OCP, the high relative intensity of ν_3 (1552 cm^{-1}) and the low relative intensity of ν_{18} (757 cm^{-1}) indicate that the interaction between Trp and Ag is mainly through pyrrole (C_2=C_3) but not through phenyl ring; (ii) at the potentials of (–0.8; –0.4) V, a weakening of pyrrole ring coring to the surface occurs and the distance between indole and Ag surface increases; (iii) at –1.0 V, the indole reaches the Ag surface and interacts more strongly with Ag through both pyrrole and phenyl rings (ν_3 band shifts to 1563 cm^{-1} at –1.0 V).

In contrast to OCP, where the pyrrole–Ag interaction occurs mainly via (C_2=C_3), the pyrrole–Ag interaction at –1.0 V is enhanced by (N_1–H). The band ν_{17} ($\delta(N_1–H)$) at 874 cm^{-1} is an indicator of the strength of the H-bond of the side chain of Trp [127]. It was shown [127] that the shift down to 871–872 cm^{-1} indicates that the Trp side chain is involved in very strong H-bonding, while the shift to 877 cm^{-1} serves as a signature of moderate H-bonding to the solvent molecules. Under OCP and at the applied potential of 0.0 V, the low intensity of ν_{17} and its position at 876–877 cm^{-1} suggests the solvation of the (N_1–H) with water molecules and the absence of the strong interaction with the Ag electrode surface.

At negative potentials, the increase in intensity and the downward shift to 874 cm^{-1} indicate the pyrrole ring coring through [N_1–H] to the Ag surface. Such an anchoring may result from the electrostatic interaction of N_1–H with the Ag surface, since the applied potential of –1.0 V is below the ZCP, which determines the negative charge of the electrode surface under the current experimental conditions and the attraction of N_1–H to the surface [83].

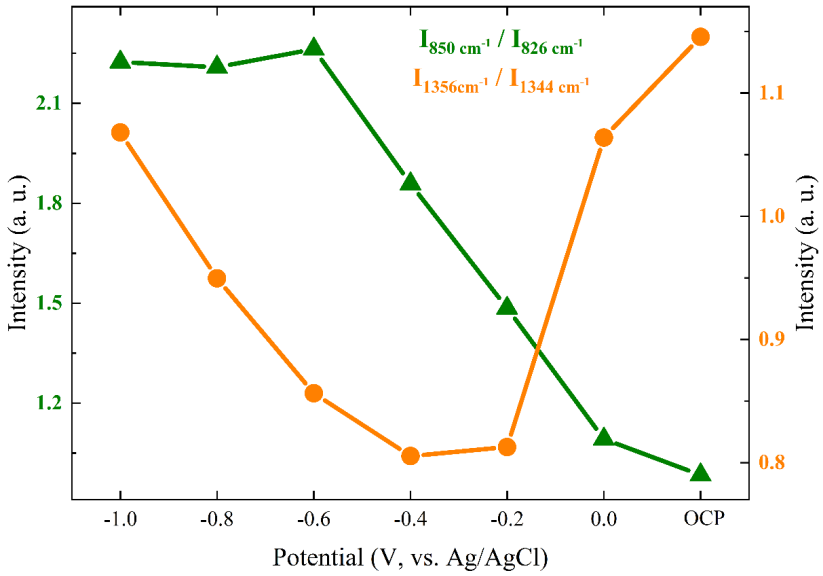

Figure 18. The dependence of the intensity ratios of Tyr (green) and Trp (orange) doubles on the applied potential in the solution containing 0.1 M Na_2SO_4 and 0.01 M NaH_2PO_4 (pH 7.0).

The characteristic doublet at 1344 cm^{-1} and 1356 cm^{-1}, which originates from Trp, can be recognized at all applied potentials of the Ag electrode (Fig. 17D). However, the maximum intensity values of both bands are observed at an applied potential of 0.0 V, indicating the smallest spacing between the indole and the Ag surface. The intensities of both bands almost coincide at –1.0 V and under OCP conditions but are significantly reduced in the range of (–0.8; –0.4) V, which confirms the rearrangement of the indole and the weakening of the interaction with the Ag surface. The change in the intensity ratio of this doublet is a marker for the hydrophobicity [152] of the environment (solvent) and can indicate the conformational changes of the U-II molecule during the change of the potential of the Ag electrode. In a hydrophilic environment, the I_{1356}/I_{1344} ratio does not exceed 0.93, while values above 1.1 indicate a hydrophobic environment [127,161]. At the potentials (–0.8; –0.2) V, the ratio I_{1356}/I_{1344} is below 0.95 meaning that the indole ring is exposed to aqueous medium [149] (Fig. 18, orange curve). This confirms the assumption that the interaction of Trp and the electrode is weakened in this range of the applied potentials, the Trp residue moves away from the electrode surface and is exposed to the buffer solution. At –1.0 V and under OCP/0.0V (Fig. 18, orange curve), the ratio I_{1356}/I_{1344} exceeds 1.06 indicating that the Trp residue is exposed to the hydrophobic environment, e.g.

it is in contact with aliphatic side chains of the peptide. The latter is confirmed by the enhancement of the band intensities in the frequency range 2800–3200 cm^{-1} associated with the ($CH/CH_2/CH_3$) vibrations of the aliphatic side chains (Fig. 16, Table 3). At –1.0 V, there are bands at 2820–2830 cm^{-1} which are attributed to the ν(CH) of the methylene groups (–CH_2–), 2870–2890 cm^{-1} assigned to $\nu_s(CH_2)$, and 2922 cm^{-1} (ν(CH_3) end chain and/or $\nu_{as}(CH_3)$). Significant increase of the ν(CH) at negative potentials indicates the direct contact of these groups with the electrode surface and more likely originate from the Lys side chain which approaches the Ag electrode surface through the NH_3^+ group. The positively charged NH_3^+ end chain of Lys is electrostatically attracted to the negatively charged Ag surface under the applied potential of –1.0 V, which is below the ZCP. At 0.0 V or under OCP the band around 2820–2830 cm^{-1} disappears, indicating that the methylene –CH_2– groups are detached, and the spectrum is dominated by the bands around 2920–2930 cm^{-1} and 2870 cm^{-1}, which can be attributed both to Phe/Trp and to Val. Taken together, these changes indicate that the aliphatic side chain of Lys creates a hydrophobic environment around Trp at more negative potentials, whereas at 0.0 V and OCP this environment arises from the proximity of Phe and probably Val, which explains high values of the I_{1356}/I_{1344} ratio.

It is worth noting that the band at 3061 cm^{-1} attributed to (=C–H) of Phe, Trp and Tyr is absent at negative potentials and increases at more positive potentials and under OCP (Fig. 16). The small intensity of the =C–H vibrations at 3063 cm^{-1} and a significant increase of the ring breathing vibrations indicate a generally vertical orientation of Phe, Trp and Tyr with respect to the electrode surface. The change of the electrode potential to less negative values causes the reorientation of the moieties and their angle orientation.

The empirical estimation of the secondary structure of the U-II peptide can be made based on the position and intensity of Amide I (approx. 1670 cm^{-1}) and Amide III (approx. 1265 cm^{-1}) bands. In contrast to OCP spectra, which show weak not resolved bands (shoulders) of Amide III and Amide I, both Amide I and Amide III are enhanced at negative applied potentials (Fig. 16). Appearance of Amide I band's vibrations indicate that the cyclic part of the peptide approaches closer to the Ag surface. The band of Amide I appears as a shoulder at 1670 cm^{-1} and shifts to 1660 cm^{-1}, and the band of Amide III shifts from 1265 cm^{-1} to 1270 cm^{-1} when the potential changes from 0.0 V to –1.0 V (Table 3). However, even when enhanced, the bands of Amide I/III are poorly resolved. In contrast to U-II in solid phase, which mainly exhibits type

II'β-turn peptide molecules (Fig. 13), the molecules adsorbed on the Ag surface at negative potential show a disordered structure [162].

A band at 506 cm^{-1} related to the stretching vibration ν (S–S) of the disulfide bond between Cys^5 and Cys^{10} (GGG-conformation) is very weak in the whole range of the applied potentials indicating that these residues do not reach the Ag electrode surface. The presence of the bands around 2920–2930 cm^{-1} which are assigned to the $\nu(CH_3)$ end chain and/or ν_{sym} (CH_3) may indicate the localization of Val and probably Thr relatively close to the electrode surface both under OCP conditions and applied negative potential with substantial enhancement at –l.0 V. The other residues (Glu, Pro, Asp) more likely do not reach the Ag surface.

In summary, the EC-SERS spectra show that the amino acid residues Phe, Trp, Tyr and Lys (depending on the applied potential) are localized approximately on the same side of the polypeptide backbone and are oriented towards the Ag electrode surface. The S–S bond between the Cys^5 and Cys^{10} residues maintains integrity and remains distant from the electrode surface in the whole range of the applied potentials. High relative intensities of the Trp, Phe and Tyr under OCP conditions indicate that, without the applied potential, the U–II peptide is anchored to the Ag surface mainly through the pyrrole ring of Trp and Phe with the angle orientation of the rings but without a strong interaction with the surface (Fig. 19). Under the applied negative potential Phe reaches the surface of the electrode, enhanced in-plane Phe modes and downshift of Phe ν_{12} suggests physical interaction of the Phe ring with the surface and its predominant vertical orientation, which is confirmed by the decreasing of the ν(=C–H) at 3063 cm^{-1}. Reorientation of Tyr occurs probably due to the phenolic hydroxyl group of the Tyr (O–H···Ag) attraction and is more likely oriented at an angle to the Ag surface allowing the enhancement of the ring breathing vibrations [149]. However, the formation of a strong hydrogen bond with the $–NH_3$ group of Lys could not be excluded. The Phe and Tyr reorientation favors the approach of the Lys motif to the surface. The approach of $–NH_3^+$ to the Ag electrode surface is also favored by the negative charge of the electrode, since the applied potential of –1.0 V is below the ZCP. It is reflected in the increase of the ν(CH) of the methylene groups ($–CH_2–$) at 2820–2830 cm^{-1} at –1.0 V. The close location of the aliphatic Lys side chain near the Trp motif is also proved by high values of the I_{1356}/I_{1344} ratio of Trp doublet indicating hydrophobic environment of Trp. The rearrangement of the Trp also occurs: the pyrrole coring at 0.0 V through $[C_2=C_3]$ changes to a strong interaction with Ag through both pyrrole $[N_1–H]$ and phenyl rings at –1.0 V.

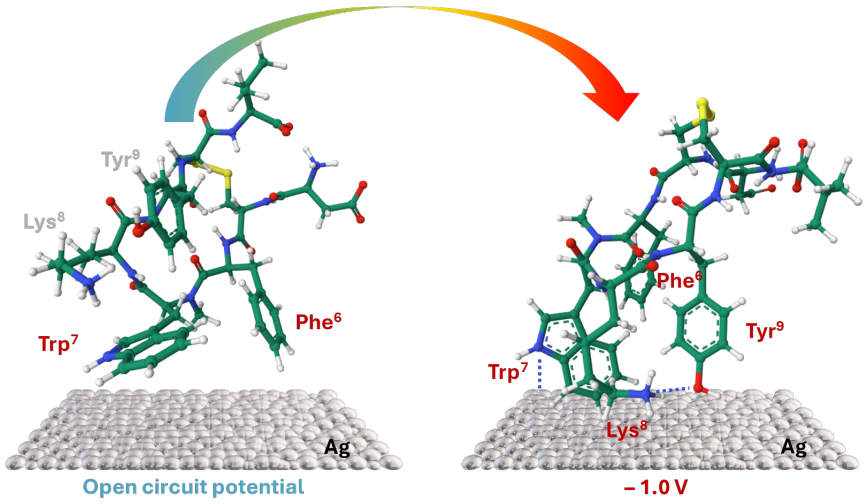

Figure 19. Scheme of the possible orientation and potential-induced changes in the interaction of the U-II peptide Asp–c[Cys–Phe–Trp–Lys–Tyr–Cys]–Val sequence with the roughened surface of the Ag electrode in the Na_2SO_4-containing solution. The possible conformations of the U-II Asp–c[Cys–Phe–Trp–Lys–Tyr–Cys]–Val were selected from the optimized geometries of this sequence simulated in a membrane-mimetic environment (images of the sequence geometries are from RSCB Protein Data Bank of PBD id 6HVB [163,164]).

3.3.2 EC-SERS measurements performed in a buffer containing $NaClO_4$

Figure 20 presents the EC-SERS spectra of U-II peptide in the concentration 10^{-5} M in solution containing 0.1 M $NaClO_4$ and 0.01 M NaH_2PO_4 at physiological pH. The replacement of Na_2SO_4 by $NaClO_4$ was done to avoid the overlapping of the Phe (1002 cm^{-1}), ν(C–C) and/or ν(C–N) (964 cm^{-1}) with SO_4^{2-} (982 cm^{-1}) bands in the range of 960–990 cm^{-1}, as the main characteristic band of the ClO_4^- anion in Raman spectrum is centered at 934 cm^{-1} [165,166].

Under OCP conditions (Fig. 20), the characteristic bands of Phe and Trp residues at 621 cm^{-1} (Phe, ν_{6b}), 758 cm^{-1} (Trp, ν_{18}), 1002 cm^{-1} (Phe, ν_{12}), 1031 cm^{-1} (Phe, ν_{18a}), 1174 cm^{-1} (Phe, ν_{9a}), 1207 cm^{-1} (Phe, ν_{7a}), 1239 cm^{-1} (Trp, ν_{10}), 1343/1357 cm^{-1} (Trp doublet), 1547 cm^{-1} (Trp, ν_{19b}), 1598 cm^{-1} (Phe, $\nu_{8a,b}$) are dominant in the SERS spectra. The bands arising from Cys^5–Cys^{10} at 505 cm^{-1} (S–S) and Tyr at 826/853 cm^{-1} (Tyr doublet) are clearly visible.

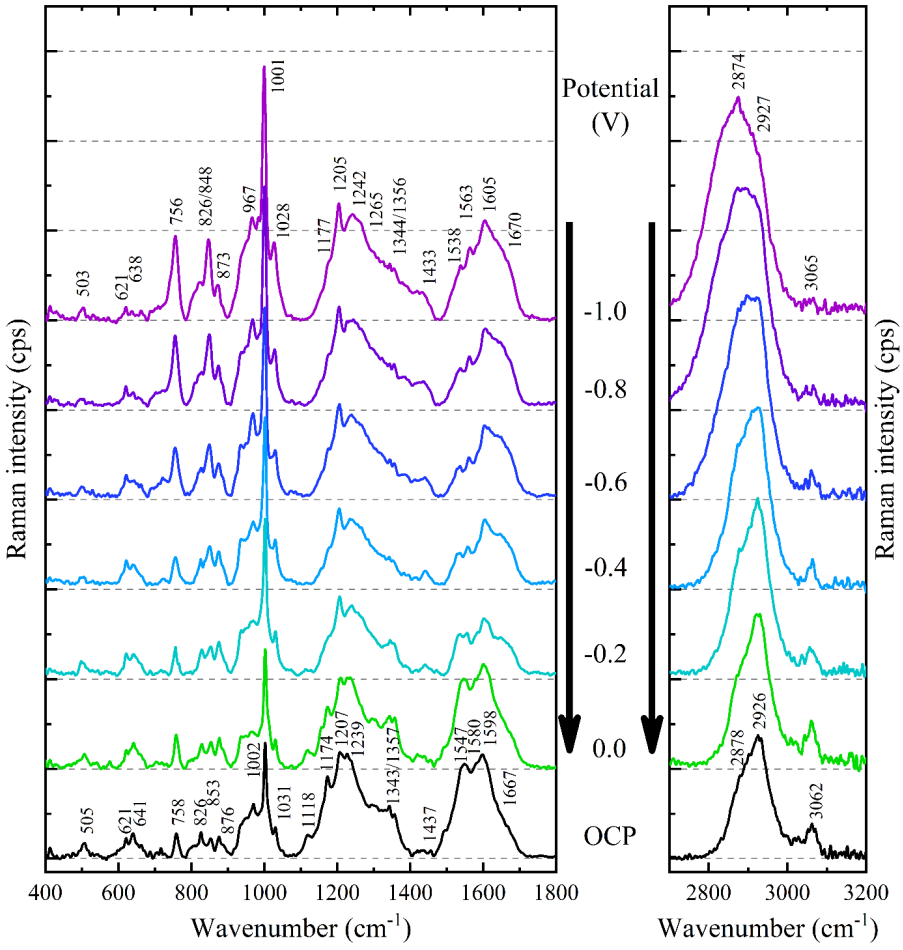

Figure 20. The dependence of the SERS spectra of the U-II solution on the Ag electrode, shown in the spectral ranges (A) 400–1800 cm^{-1} and (B) 2700–3200 cm^{-1}. The solution contains 0.1 M $NaClO_4$, 0.01 M NaH_2PO_4 (pH 7.0) and 10^{-5} M U-II peptide. Excitation wavelength 785 nm, laser power 60 mW, integration time 300 s.

In the range of 2800–3200 cm^{-1}, the characteristic bands of ν(CH/CH_2/CH_3) at 2850–2920 cm^{-1} and the stretching ν(=C–H) of the phenolic rings of Phe and Trp [135,137] at 3062 cm^{-1} are also present.

The weak band at 1495 cm^{-1} can be assigned to Tyr (disubstituted aromatic ring) [135,137], however, it overlaps with Trp modes at 1520–1550 cm^{-1} making it difficult to clearly distinguish between these two residues.

Under the conditions of applied potential and switching the potential from –1.0 V to 0.0 V, the characteristic bands of Phe (ν_{12}, ν_{18a}, ν_{7a}, ν_{8a}, ν_{8b}) have

similar behavior in solutions containing either SO_4^{2-} or ClO_4^- ions. The intensities of all main characteristic bands decrease up to a potential of –0.2 V, and, in the case of a solution containing perchlorate ions, show a clear increase in intensity on subsequent transition to a positive potential. Such a change could be associated with a closer approach of the Phe residue to the Ag electrode surface under positive potentials. The behavior of the normalized intensity of the band at 621 cm^{-1} shows a trend opposite to that of the other bands of Phe, with the maximum intensity reached at –0.4 V, consistent with the trend described in section 3.3.1. All the normalized intensities of characteristic bands of Phe are presented in Figure 21A.

In the case of the Tyr residue, the band of deformation vibrations δ(CCC) at 638 cm^{-1} (ν_{6b}) increases and bands of Tyr doublet at 826/848 cm^{-1} decrease significantly when the potential of the electrode in the solution containing ClO_4^- anions changes in the anodic direction. The change in the ratio of the Tyr doublet I_{848}/I_{826} is shown in Figure 22 (green curve). From the behavior of the doublet, it can be concluded that Tyr undergoes changes similar to those observed when the potential changes in a solution containing sulfate anions. It means that the phenolic hydroxyl group of the Tyr residue switches from acceptor state to the hydrogen donor for strong H-bonds. As mentioned above, the Tyr band at 1172 cm^{-1} (ν_{9a}) overlaps with the ν_{9a} vibration of Phe which makes it difficult to separate the two bands and probably explains the increase in the normalized intensity of this band when the potential changes from –0.2 V to the OCP conditions (Fig. 21B).

At –1.0 V, the normalized intensities of the main vibrations of the Trp residue demonstrate the same trend as in the solution with SO_4^{2-} anions. The normalized intensities of the bands at 756 cm^{-1} (ν_{18}, phenyl/pyrrole ring-breathing mode,) 873 cm^{-1} (ν_{17}, Fermi resonance between phenyl ring breathing and out-of-plane ring bending overtone), 1433 cm^{-1} (ν_6, pyrrole (ν_s(NCC) + δ(NH)) + phenyl δ(CH)) decrease monotonically when the potential changes to the anodic direction (see Fig. 21C). In the case of the Trp doublet at 1344/1356 cm^{-1} (Fermi resonance), the dependences of the normalized intensities of the bands at 1538 cm^{-1} (ν_{19b}) and 1563 cm^{-1} (ν_3) on the applied potential are described by the U-shaped curves with a minimum at –0.4 V and a maximum at 0.0 V and/or OCP (Fig. 21D). The ratio of the intensities of the characteristic doublet at 1344 cm^{-1} and 1356 cm^{-1} decreases when the potential changes in the anodic direction (Fig. 22, orange curve).

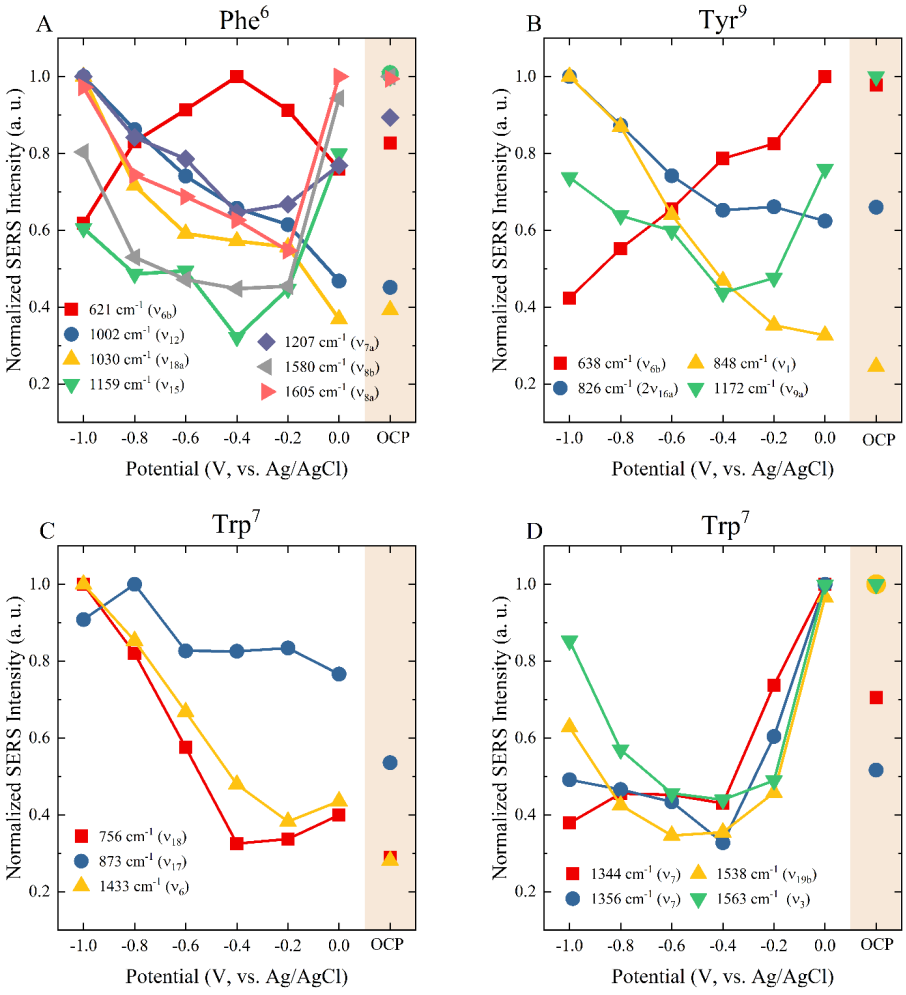

Figure 21. The dependencies of the normalized intensities of characteristic bands of (A) Phe, (B) Tyr and (C, D) Trp residues of U-II on the applied potential in the solution containing 0.1 M $NaClO_4$ and 0.01 M NaH_2PO_4 (pH 7.0).

According to [127,161], the intensity ratio at –1.0 V, which is about 1.8, indicates a hydrophobic environment of the Trp residue, while the ratio values around 1.06 and 1.02 at –0.4 V and under OCP (Fig. 22, orange curve), respectively, indicate a hydrophilic environment and the exposure of the residue to the solution but not to the non-polar side chains of AAs.

From the comparison with the results in section 3.3.1, we can conclude that the rearrangement of the indole ring relative to the Ag electrode surface occurs independently of the composition of the solution. The magnitude of the

Trp doublet in the SERS spectra increases locally at an electrode potential of 0.0 V. The corresponding maxima of the intensities of the ν_{19b} and ν_3 bands (see Fig. 21D) at 0.0 V and under OCP could indicate the small distance (minimum at the applied potentials of (–1.0; 0.0) V) between the indole ring and the Ag surface in the solution containing ClO_4^- anions.

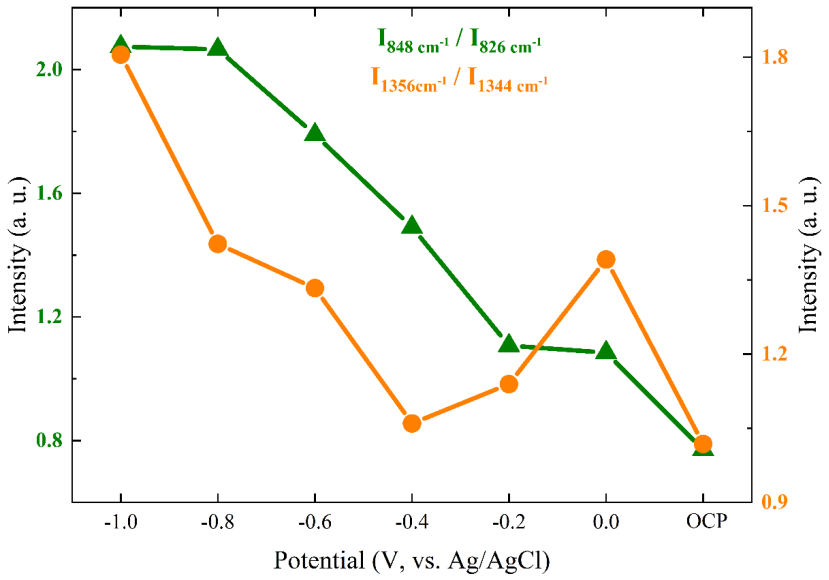

Figure 22. The dependence of the intensity ratios of Tyr (green) and Trp (orange) doublets on the applied potential in the solution containing 0.1 M $NaClO_4$ and 0.01 M NaH_2PO_4 (pH 7.0).

In comparison to the Na_2SO_4-containing solution, both Amide I and Amide III bands at 1670 and 1265 cm^{-1} are clearly visible in a $NaClO_4$-containing solution. Under OCP conditions, the Amide I band associated with the in-plane stretching vibration of C–N and the bending vibration of N–H may indicate that the peptide chain is located at a small distance from the Ag electrode surface. In contrast to Na_2SO_4-containing solution, both Amide I and Amide III are more intense and increase at negative potentials, indicating that the peptide is closer to the Ag electrode surface than in the solution with SO_4^{2-}. In the range of 2800–3200 cm^{-1}, the characteristic bands of $\nu_{as}(CH_2)$ at 2878 cm^{-1} and $\nu(CH_3)$ at 2926 cm^{-1} dominate. Moreover, both in Na_2SO_4-containing and $NaClO_4$-containing solutions, the weak band at 3062 cm^{-1}, assigned to ν(=C–H) of the phenolic ring of Phe and Trp [137] appears under OCP conditions and slightly negative potentials. The appearance of this band under these conditions possibly indicates the orientation of the Phe and Trp

residues at an angle to the Ag electrode surface creating the conditions for the enhancement of the band intensity.

From the comparison of the SERS spectra of the U-II peptide obtained by changing the potential in systems with different buffer solution compositions, it follows that the behavior of the peptide is similar and is related to the adsorption of the peptide molecule by the amino acid residues Phe, Trp and Tyr. The decrease of the normalized intensities of the characteristic bands is associated with the process of reorientation of the molecule near the Ag electrode surface when the potential changes from –0.4 to –0.2 V. As a result, the Lys and Val residues probably approach the Ag surface at more negative potentials, as the additional bands at 969 cm^{-1} (ν (C–C) and/or ν(C–N)), 2874 cm^{-1} ($\nu_s(CH_2)$) and 2927 cm^{-1} ($\nu(CH_3)$ end chain, $\nu_{as}(CH_3)$) are enhanced in the spectra. The possible orientation of the U-II peptide fragments near the Ag electrode surface in the $NaClO_4$-containing solution and the changes in their binding to the roughened Ag electrode associated with the change in the potential of the system are similar to those that occur in the Na_2SO_4-containing solution. The presumed U-II orientation in relation to the Ag electrode surface and corresponding potential-induced changes are shown in Figure 19.

Table 3. Assignment of the SERS characteristic bands of the U-II molecules (10^{-5} M) absorbed on the Ag electrode surface under –1.0 V, 0.0 V and OCP conditions. The solution contains 0.1M Na_2SO_4 or 0.1M $NaClO_4$ and 0.01 M NaH_2PO_4 (pH 7.0) [136,139,143,144,149–152].

Wavenumber, cm^{-1} **SERS**						Assignments
0.1M Na_2SO_4			0.1M $NaClO_4$			
–1.0 V	0.0 V	OCP	–1.0 V	0.0 V	OCP	
506	–	–	503	503	505	ν (S–S) GGG
529	529	–	530	530	528	ν (S–S) TGG
621	621	621	621	622	621	Phe (ν_{6b})
639	641	641	638	641	641	Tyr (ν_{6b}) [δ (CCC)]
–	651	651	651	651	–	ν (C–S)
661	661	661	663	661	662	
687	687	687	688	687	687	
–	–	702	701	704	704	
719	719	–	720	716	716	Trp (ν_{19})

						and/or Tyr (ν_4) [γ(CCC)]
756	757	757	756	758	758	Trp (ν_{18}) [phenyl/pyrrole in-phase ring breathing]
809	812	–	807	809	–	–
826	826	826	826	826	826	Tyr doublet ($2\nu_{16a}$), [γ (CCC), γ (C–H)] (ν_1), [δCCC]
850	853	853	848	853	853	
874	876	877	873	877	876	Trp (ν_{17}) [indole + δ(NH)] and Fermi resonance between phenyl ring breathing and oop ring bend overtone
949	949	950	949	949	950	ν (C–C=O)
964	964	964	967	966	969	Tyr (ν_{17a}) [γ (C–H)], ν (C–C) and/or ν (C–N)
1002	1003	1003	1001	1002	1002	Phe (ν_{12})
–	1012	1012	–	1013	1013	Trp (ν_{16}) [phenyl and pyrrole rings oop-breathing]
1030	1030	1030	1028	1030	1031	Phe (ν_{18a}) [δ (C–H)]
1077	1074	1074	1073	1075	1075	ν (C–C) alkyl chain
–	1117	1118	–	1118	1118	ν (C–C) Trp (ν_{13}) and/or Tyr (ν_{15}) [indole ring bending]
1159	1159	1159	1155	1158	1158	ν_{as}(CCN) and/or Trp δ (N–H)

1178	1178	1178	1177	1174	1174	Phe (ν_{9a}) and/or Tyr(ν_{9a}) [in-plane δ(C–H)]
1205	1207	1207	1205	1209	1207	Phe (ν_{7a}) [ν (C–C)] and/or Tyr [δ (C–H)], [ν (C_6H_5–C)]
1233	1233	1235	1242	1236	1239	Trp (ν_{10}) [(C–CH_2)]
1270	1266	1265	1265	1265	1266	Amide III
1344	1343	1343	1344	1343	1343	Trp doublet (ν_7) w (CH_2), indole ν (N_1–C_8)
1356	1358	1358	1356	1358	1357	
1438	1438	1439	1433	1439	1437	Trp (ν_6) [pyrrole (ν_s(NCC) + δ (NH)) + phenyl δ (C–H)]
–	1492	1491	–	1493	1495	Disubstituted aromatic ring
1538	1540	1538	1538	1547	1547	Trp (ν_{19b})
1563	1552	1552	1563	1555	1555	Trp (ν_3) [ν (C_2=C_3)] and/or AII
1583	1582	1582	1583	1578	1580	Phe (ν_{8b}) and/or Trp (ν_2) [ν (C=C)]
1606	1604	1605	1605	1601	1598	Phe (ν_{8a}) and/or Tyr ($\nu_{8a,b}$) [ν (C=C)]
1615	1615	1613	1620 sh	1614 sh	–	Trp (ν_1) [indole + ν (N–C)]
1660	1670	1672	1670	1675	1667	Amide I (mostly ν(C=O), small contribution from δ(N–H))
2823	–	–	2826	–	–	ν_s(CH) of CH_2 (soft mode)
2876	2873	2873	2874	2875	2878	ν_s(CH_2)

2922	2924	2928	2927 sh	2926	2926	ν (CH_3) end chain, $\nu_{as}(CH_3)$
3063	3061	3061	3065	3062	3062	Phe, Trp (ν (=C–H))

Abbreviations: ν – stretching; δ – bending; γ – nonplanar ring vibration; w – wagging; s – symmetric; as – asymmetric, oop – out of plane, sh – shoulder.

Summarize, the EC-SERS spectra of the U-II peptide presented in Figure 16 and Figure 20 show that the Phe, Trp and Tyr amino acid residues are mainly attached to the surface of the silver electrode. However, the application of a negative potential leads to a realignment of the molecule near the Ag surface and its additional anchoring by residues Lys and Tyr. This indicates that the adsorption of the peptide to the Ag surface is mainly through the cyclic hexapeptide sequence c–[Cys–Phe–Trp–Lys–Tyr–Cys], which presumably plays the main role in the regulatory activity of the peptide and determines the efficiency of peptide binding to its receptor. Although, the exchange of Na_2SO_4 for $NaClO_4$ in the content of the solution does not lead to significant differences in the mechanism of adsorption of the U-II peptide on the electrode surface, it still affects the degree of adsorption of the peptide on the surface and the interaction of the peptide with the Ag surface when the applied potential is changed in the anodic direction. In contrast to Na_2SO_4-containing solution, in $NaClO_4$-containing solution the intensities of Phe [ν_{8a}, ν_{8b}, ν_{7a}] and amide III (1264 cm^{-1}) are significantly higher under OCP and remain enhanced at negative potentials of the electrode, indicating a stronger interaction of the Phe ring with the Ag surface and a closer localization of the peptide backbone at the electrode in the whole range of applied potentials. The latter is also confirmed by the higher intensity of the ν(S–S) at 503 cm^{-1} of the Cys^5–Cys^{10} bridge (GGG), which is more pronounced in $NaClO_4$-containing solution. However, the general mechanism of U-II peptide adsorption is similar in both solutions: when the potential of the Ag electrode reaches the magnitude of –1.0 V, the Lys and Tyr residues also approach the Ag electrode surface. Under these conditions, the U-II peptide is firmly pressed to the surface by the direct contact of residues Phe and Trp with the surface and anchored by Lys and Tyr, which interact with the Ag surface via NH_3^+ and –OH groups, respectively. The latter conformational change is supported by the changes in the intensity ratio of the Trp and Tyr doublets, which indicate the transition of the Trp residue from the polar medium at (–0.8; –0.2) V to the nonpolar environment of the Lys side chain at –1.0 V and the reorientation of the Tyr residue due to the interaction of the phenolic hydroxyl group with the Ag surface.

This was summarized in the **third statement** of the thesis: As the system potential changes, the molecule reorients with respect to the electrode, and additional adsorption occurs via the Lys residue. When the potential of the Ag electrode becomes more negative, the distance between the U-II peptide and the electrode surface decreases. The replacement of anions in the system (from Na_2SO_4 to $NaClO_4$) does not significantly affect the U-II peptide adsorption mechanism.

The results presented in the Section 3.3 are summarized in scientific article: **A.Klimovich**, L.Golubewa, Y.Padrez, I.Matulaitienė. Characterization of Human Urotensin II Peptide Adsorbed on Silver Electrode by Surface-Enhanced Raman Scattering Spectroscopy. *Spectrochimica Acta Part A: Molecular and Biomolecular Spectroscopy, 2025, 329, 1386-1425.* DOI: 10.1016/j.saa.2024.125565.

3.4 Comparison of adsorption U-II peptide on Ag and Au substrate

In the study of new biomolecules, the use of various metals makes it possible not only to establish the SERS spectra of the molecules, but also to characterize the process of adsorption of the molecules on various types of surfaces (metals).

In the process of studying the peptide using classic versions of gold-based SERS surfaces some unexpectable problems occurred. Gold nanoparticles and the electrochemically prepared surface of the gold electrode didn't show sufficient amplification of the Raman spectra of the U-II peptide, as a result of which a silicon-based substrate with a nanometers-scaled gold layer was used as an alternative surface.

Figure 23 demonstrates the SERS spectra of U-II solution on Ag electrode in OCP condition (A) and on bSi/Au substrate (B) in the standard solution contains 0.1 M Na_2SO_4 and 0.01 M NaH_2PO_4 (pH 7.0).

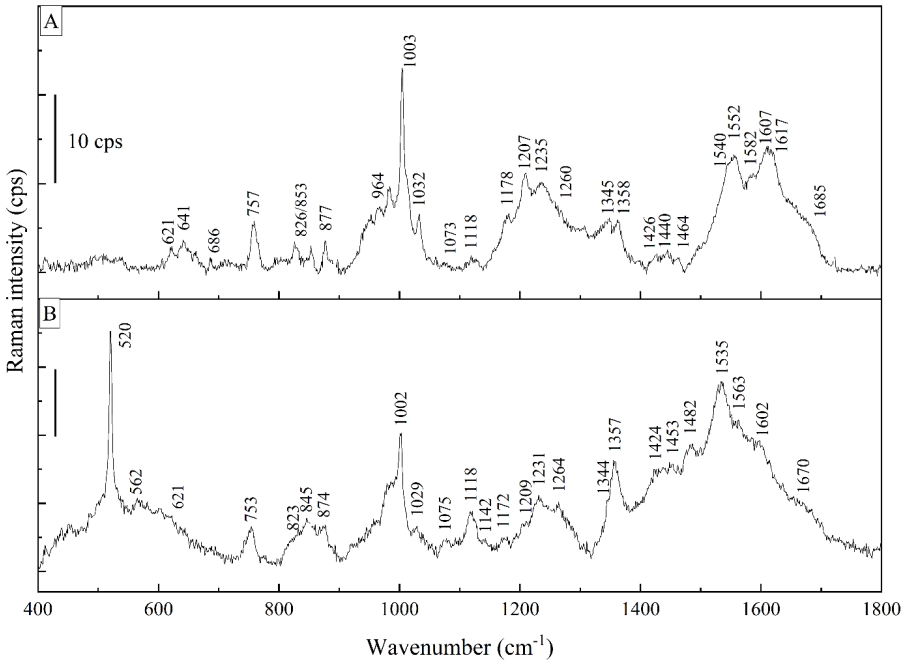

Figure 23. SERS spectrum of U-II peptide on (A) Ag electrode (OCP) and (B) bSi/Au substrate. The solution contains 0.1 M Na_2SO_4, 0.01 M NaH_2PO_4 (pH 7.0) and 10^{-5} M U-II peptide. Excitation wavelength 785 nm, laser power 30 mW, integration time 300 s.

The SERS spectrum of the U-II peptide on bSi/Au substrate contains the main bands from Phe, Trp and Tyr residue in full accordance with the previously presented Raman spectrum (see Fig. 13). Also, the most intense band at 520 cm^{-1} represents the main characteristic band of silicon [167]. The bands at 621 cm^{-1} (ν_{6b}), strong bands at 1005 cm^{-1} (ν_{12}, symmetric ring breathing), weak band at 1027 cm^{-1} (ν_{18a}, in-plane C–H bending) and shoulder at 1206 cm^{-1} (ν_{7a}) is characteristic bands of Phe. The bands from the Trp AA residue located at 752 cm^{-1} (ν_{18}, indole ring-breathing mode), 875 cm^{-1} (ν_{17}, Fermi resonance between phenyl ring breathing and out-of-plane ring bending overtone), doublet at 1343/1356 cm^{-1} are significantly enhanced in the SERS spectra. The bands at 1425 cm^{-1} and 1483 cm^{-1} (disubstituted aromatic ring) are more pronounced in the spectrum on Au substrate and indicate the approach of the U-II peptide mainly via the Trp residue. This hypothesis is also confirmed by the increased intensities at 1533 cm^{-1} (ν_{19b}, benzene ring) and 1561 cm^{-1} (ν(C=C)), shoulder at 1611 cm^{-1} ((ν_1) [indole + ν(N–C)]). The position of the band ν_{17} ($\delta(N_1–H)$) at 875 cm^{-1} indicates negligible H-bonding to the solvent molecules [127] and the strongly enhanced band at 1356 cm^{-1} from Trp doublet and the value of the I_{1356}/I_{1343} ratio above 1.2 indicate a hydrophobic environment around the U-II molecule.

The main bands from the Tyr residue are represented only by bands at 830/843 cm^{-1} (Tyr doublet), 1170 cm^{-1} (ν_{9a}, in-plane C–H bending), which can be overlapped with Phe band.

The Amide I and Amide III bands are presented in the SERS-spectra of U-II and characterize the not-destroyed structure of peptide. A weak shoulder of Amide I located at 1670 cm^{-1} and the band at 1264 cm^{-1} characterize the Amide III vibrations.

A detailed description of the SERS spectra of U-II on bSi/Au substrate shows that when the peptide is adsorbed on the Au surface, the bands characterizing the Trp AA residue are more prominent than the Phe band compared to the spectra from the Ag surface (see Fig 16, 19). Additionally, the bands characterizing stretching vibrations of (C–C) of alkyl chain at 1075 cm^{-1} and 1118 cm^{-1} (can also be coupled with other motions) may describe considerable adsorption of aliphatic Lys side chain and the main mechanism of adsorption through the indole ring of Trp.

Table 4 presents the assignment of the bands of U-II peptide adsorbed on bSi/Au substrate.

Table 4. Peak assignment of the main characteristic bands of Raman and SERS of U-II peptide on Ag electrode (OCP) and bSi/Au substrate. The solution contains 0.1M Na_2SO_4 and 0.01 M NaH_2PO_4 (pH 7.0) [136,139,143,144,149–152].

Wavenumber, cm^{-1} **Raman**	Wavenumber, cm^{-1} **SERS on Ag**	Wavenumber, cm^{-1} **SERS on Au**	Assignments
509	—	—	ν (S–S)
—	—	520	Si
—	—	562	—
621	621	621	Phe [in-plane ring deformation vibrations]
643	641	—	Tyr [δ (CCC)]
	686	—	ν (C–S), P_C–G
721	—	—	ν (C–S), P_C–T
758	757	753	Trp [phenyl/pyrrole in-phase ring breathing]
831 sh	826	823	Tyr doublet [ν (C–C)]
853	853	845	
878	877	874	Trp [δ (N–H) and Fermi resonance between phenyl ring breathing and oop ring bend overtone]
916	—	—	ν (C–C)
—	964	—	ν (C–COOH), d (C–C) of Asp/Glu
1003	1003	1002	Phe [ring breathing vibration]
1011 sh	1012 sh	—	Trp [phenyl and pyrrole ring out-of-phase breathing]
1032	1032	1029	Phe [in-phase motion of ν (C–C)]
1075	1073	1075	ν (C–C) alkyl chain

—	1118	1118	Trp/Phe, ν (C–C) alkyl chain
—	—	1142	ν_{as}(CCN) and/or Trp δ (N–H)
1177 sh	1178	1172	Tyr and/or Phe
1206	1207	1209	Phe (ν_{7a}) [ν (C–C)] and/or Tyr [δ (C–H)], [ν (C_6H_5–C)]
—	1235	1231	Amide III
1268 sh	1260 sh	1264	
1339	1345	1344	Trp doublet [pyrrole ring ν (N–C); Fermi resonance] w (CH_2)
1360 sh	1358	1357	
—	1426	1424	–
1436	1440	1443	Trp [pyrrole ν (N–C–C); δ (N–H)]
—	1464	1453	–
—	—	1482	Disubstituted aromatic ring
1549	1540	1535	Trp [ν_{19b}, pyrrole ν (C=C)]
—	1552	—	Trp (ν_3) [ν (C_2=C_3)] and/or AII
—	1582	1563	Phe [phenyl ring bond-stretching vibrations]
—	1607	1602	Phe (ν_{8a}) and/or Tyr ($\nu_{8a,b}$) [ν (C=C)]
1615	1617	—	Trp [pyrrole ν (N–C)]
1679	1685 sh	1670	Amide I [mostly ν (C=O), small contribution from δ (N–H)], β-sheet

Abbreviations: ν – stretching; δ – bending; d – deformation; w – wagging; oop – out of plane.

This was summarized in the **fourth statement** of the thesis: The nature of the metal does not have a significant influence on U-II peptide adsorption; on a gold surface, the molecule shows a stronger tendency to adsorb via Trp and Lys residues.

3.5 Black silicone nanostructured SERS substrate

The sharp vertically oriented lace-like silicon plates were produced by room-temperature ICP-RIE technique. The so-called "black" silicon surface also has a black color after the metal coating and demonstrates the enhancement factor (EF) up to 10^6. The SEM data of the lace-like Si substrate and bSi covered by Au layer presented on Figure 24. One can observe that the substrates consist of vertically oriented quasi-regular cone-like structures. The average height of cones is around 1 μm and a base diameter 100−200 nm. The sharp apexes of these plates serve as nuclei for spherical Au NP formation of averaged sizes 34,6 nm. To determine the enhancement factor, 4-mercaptobenzoic acid (4-MBA) was used as a model molecule. As a result of the calculations, the enhancement factor is estimated to be around 1.1×10^6 [119].

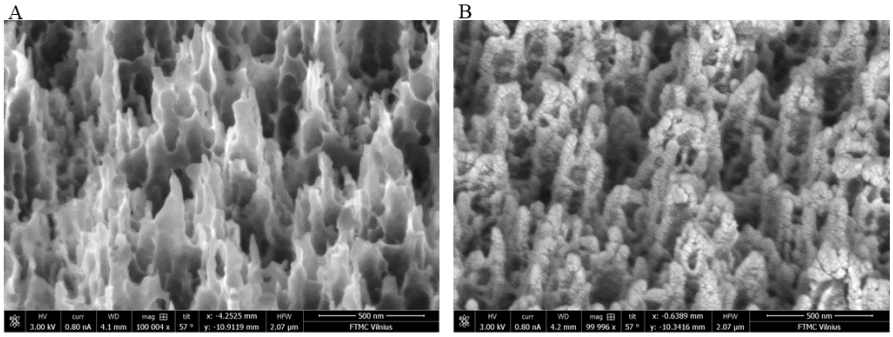

Figure 24. SEM images of bSi (A) and bSi sputtered with gold (B).

To determine the limit of detection (LOD) of bSi/Au for a molecule that does not form covalent bonds with the substrate, the Doxorubicin (DOX) was used as a test molecule. This drug is used in the fight against cancer and the determination of minimum doses is critically important in the treatment process. Figure 25 presents the SERS spectra of DOX in the concentration from 1 mM to 1 nM. SERS spectra are represented by structural fluctuations in the range of 1150−1700 cm^{-1}, and the relative intensity of this region suggests the possibility of detecting a molecule. With a further decrease in concentration to 10^{-10} M or increase upper 10^{-3} M, the description of the Raman spectrum is difficult. DOX concentration range detectable with bSi is between 10^{-9} and 10^{-4} M.

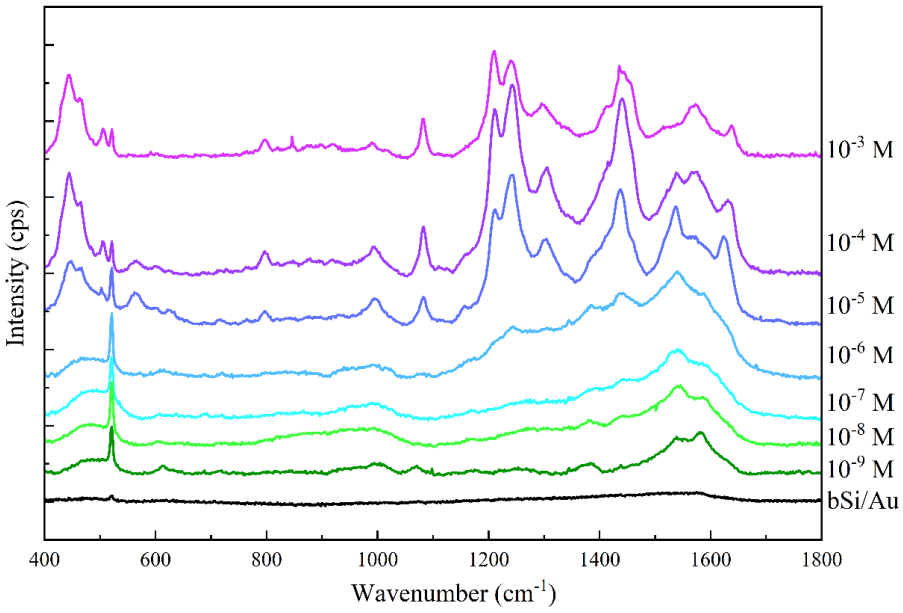

Figure 25. SERS spectra of Doxorubicin (1.0 nM to 1.0 mM). Excitation wavelength 785 nm, laser power 16,8 mW, integration time 300 s.

For the demonstration of the long-term stability of fabricated bSi/Au substrates, several freshly fabricated samples were individually packed in plastic Petri dishes, wrapped with a parafilm to avoid accidental contamination, and stored under ambient conditions. After storage for 1−20 months, these substrates were used to obtain 4-MBA SERS spectra in the same measurement setup. The results are summarized in Figure 26. The intensity of characteristic bands at 848, 1075, 1480 and 1587 cm^{-1} in the 4-MBA spectra and band at 520 cm^{-1} assigned to the Si decreased by less than 5% after 120 days of storage. After more than 20 months of storage, the signal intensity of the target molecule decreased by 40%.

In addition, a protocol for cleaning the substrate by oxygen plasma etching was developed in the course of the research, which made it possible to use the same substrate up to 10 times. This substrate demonstrates stable and reproducible signals after the procedure of cleaning by oxygen plasma for the covalent-bonded molecule – 4-MBA, and for the molecules that do not form covalent bonds with it – Doxorubicin (DOX) [119].

These results show that this substrate has potentially reusable applications for different types of molecules, have a high level of enhancement (up to 10^{-6}) and it's stable even under long-term storage conditions.

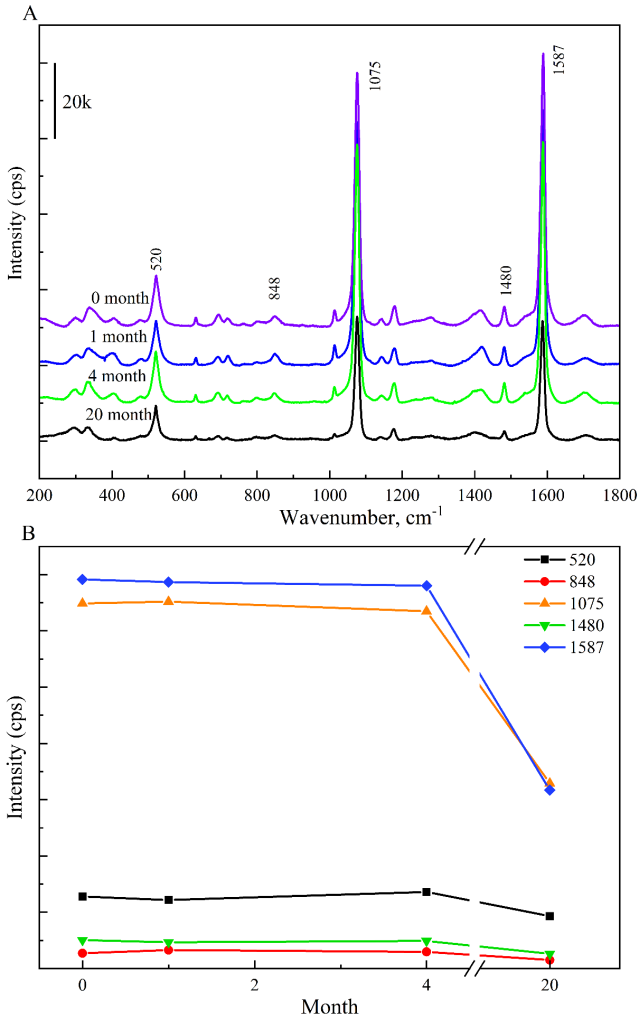

Figure 26. (A) SERS spectra of 4-MBA on the bSi/Au substrate and (B) diagram of intensity of main bands of 4-MBA on the freshly prepared surface (0 month), after 1, 4 and 20 months. Excitation wavelength 785 nm, laser power 16,8 mW, integration time 300 s.

The results presented in the Section 3.5 are summarized in scientific article: L.Golubewa, **A.Klimovich**, I.Timoshchenko, Y.Padrez, M.Fetisova, H.Rehman, P.Karvinen, A.Selskis, S.Adomavičiūtė-Grabusovė, I.Matulaitienė, A.Ramanavicius, R.Karpicz, T.Kulahava, Y.Svirko, P.Kuzhir. Stable and Reusable Lace-like Black Silicon Nanostructures Coated with Nanometer-Thick Gold Films for SERS-Based Sensing. *ACS Applied Nano Materials, 2023, 6, 6, 4770–4781*. DOI: 10.1021/acsanm.3c00281.

3.6 EC-SERS research of 4-MBA using bSi/Au substrate

After obtaining the SERS spectra on the bSi/Au substrate, the next step was the possibility to use this substrate as a substrate for EC-SERS spectroscopy. Due to the properties of silicon and the solid structure of the bSi substrate itself, this substrate can serve as a working electrode in a classical electrochemical cell which fully meets the requirements of EC-SERS.

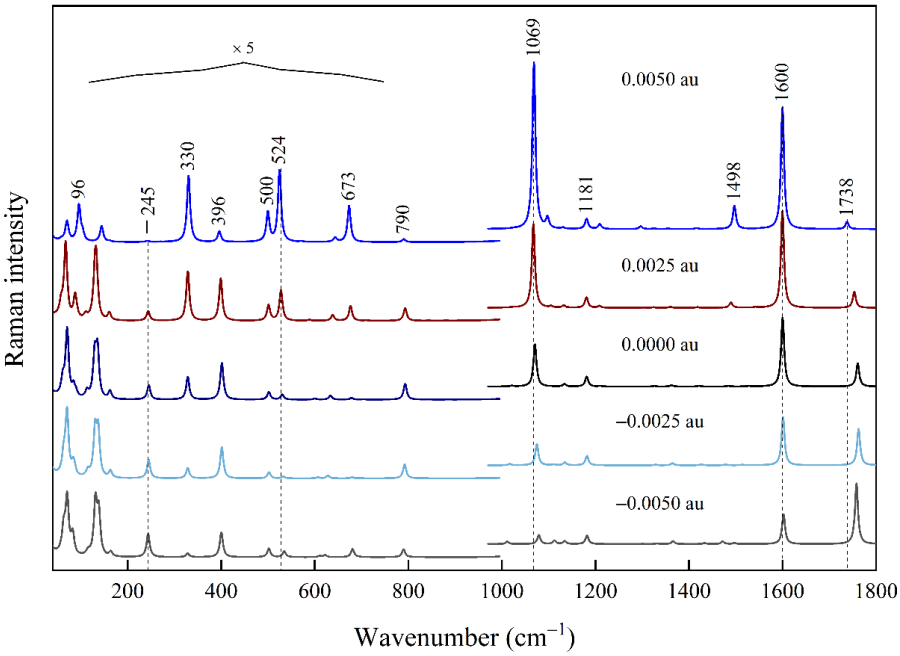

Figure 27. Theoretical Raman spectra of Au_4-4-MBA complex. The electric field direction was along the X-axis.

In the first step, the EC-SERS of the simple testing molecule – 4-MBA – was provided to demonstrate the possibility of using this substrate as a working electrode. Before the measurement, DFT simulations of behavior of 4-mercaptobenzoic acid molecule were performed using the Gaussian 09 program for a theoretical modeling of the Au_4-4-MBA complex (Figure 27). The electric field was oriented along the X-axis, which is tilted approximately 30° towards the Au–S bond of the 4-MBA molecule. A similar tilting with respect to the surface normal is known experimentally for Au and Ag-adsorbed alkanethiol molecules [168]. The electric field had little effect on 4-MBA tilting with respect to Au_4 cluster (Au–S–C angle changed only by 2.57 degrees), bond length of C–C and C–H (δ=2.3 pm), S–C bond (δ=5.5 pm) and

within the Au_4 cluster, whereas the C–O bonds changed by 1.1 and 1.6 pm. Selected parameters are presented in Table 5. The Au cluster vibrations at 71, 130, and 136 cm^{-1} are more presented in the low energy region (Fig. 27, F = 0.0000 a.u). The effect of the electric field on Raman intensities of specific spectral bands is presented in Figure 28, Tables 5–6.

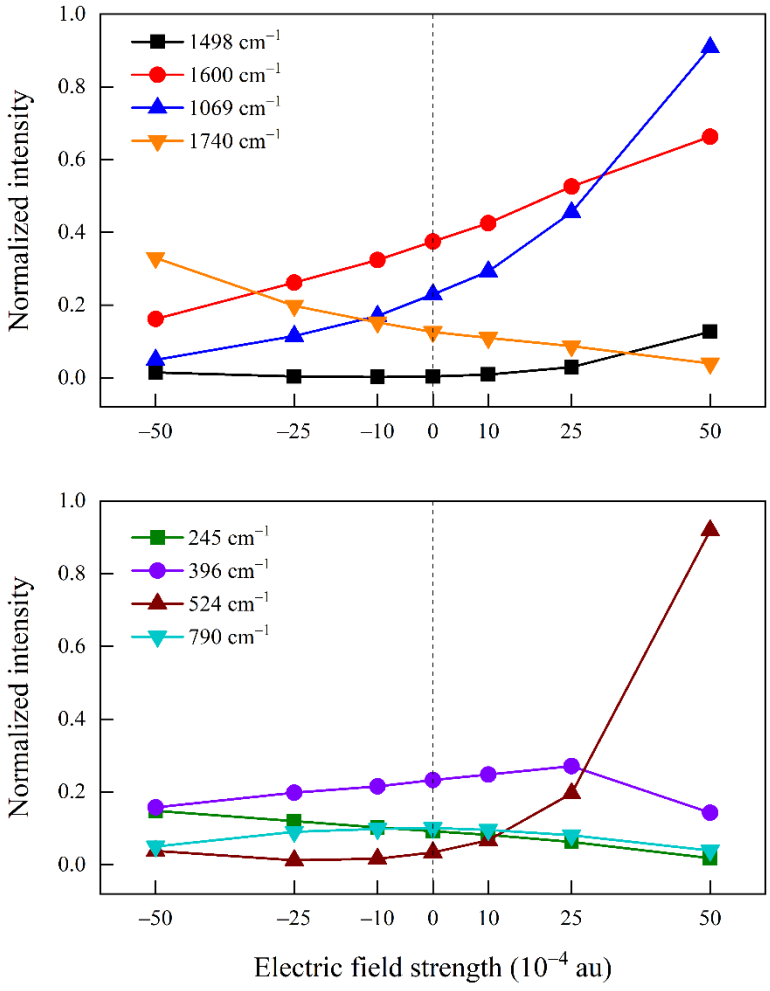

Figure 28. Normalized Raman intensities of Au_4-4-MBA complex.

Table 5. The theoretical bond length, angle, and charge dependencies of Au_4-4-MBA complex on electric field strength.

Electric field strength / au	S–C / pm	Au–S /pm	Au–S–C/ deg.	Au_4 charge	4-MBA charge
0.0050	176.7	229.8	114.9	0.19	0.81
0.0025	174.7	228.2	113.5	0.13	0.87
0.0010	173.9	227.8	113.1	0.07	0.93
0.0000	173.4	227.2	112.6	0.23	0.77
– 0.0010	172.9	227.6	112.6	– 0.02	1.02
– 0.0025	172.3	227.5	112.3	– 0.08	1.08
– 0.0050	171.2	227.7	112.3	– 0.19	1.19

Table 6. Variation in vibrational frequencies (cm^{-1}) of Au_4-4-MBA complex at various field strengths.

Electric field strength / au	ν (Au–S) + ν (C–S)	δ_{oop} (CCC)	ν_{12}	ν_{8a}	ν (C=O)
0.0050	242	525	1068	1600	1738
0.0025	242	525	1068	1600	1738
0.0010	245	530	1069	1600	1759
0.0000	245	531	1071	1600	1761
– 0.0010	245	532	1072	1601	1762
– 0.0025	245	533	1075	1601	1763
– 0.0050	244	535	1079	1602	1758

Since the influence of the 4-MBA molecule is not taken into account in the modeling, there are small changes in the position of the bands due to the vibrational Stark effect [169]. The main spectral peak at 245 cm^{-1} (Au–S)+(ν(S–C)), 530 cm^{-1} (δ_{oop}(CCC)), 1071 cm^{-1} (ν_{12}), 1600 cm^{-1} (ν_{8a}) and 1761 cm^{-1} (ν (C=O)) are redshifts by δ = 3, 6, 3, 0, and 23 cm^{-1} when the increasing of electric field intensity occurs (F = 0.0050 au). Whereas the potential of F = –0.0050 au affects peak position by δ = –1, 4, 8, 2, and –3 cm^{-1}, respectively. Figure 28 demonstrates normalized Raman intensities of the Au_4-4-MBA

complex. During the change of the electric field from negative to positive, the spectral mode intensities at 1600, 1498, 1069 and 524 cm^{-1} increase, and the peaks at 1740, 245 cm^{-1} demonstrate the opposite tendency. This leads to alterations in the polarizability characteristics and may be considered as a contribution to the chemical enhancement mechanism [170,171].

Theoretical models suggest that the impact of molecular structure and orientation on the surface is minimal, and the primary cause of changes in spectral mode intensities is the altered polarizability of molecular groups, driven by charge transfer between 4-MBA and Au_4.

On the next step the EC-SERS measurements of adsorbed 4-MBA on bSi/Au substrate was perfomed.

Figure 29 demonstrates EC-SERS spectra of 4-MBA on bSi substrate in 0.1M Na_2SO_4 solution in the range of potential from – 0.8 V to + 0.3 V. The vibrations of the aromatic ring of the 4-MBA molecule at 1077 cm^{-1} and 1590 cm^{-1} are dominant in the SERS spectra in all range of potential [172,173]. The successful functionalization of bSi/Au surface by S-Au covalent binding of 4-MBA can be characterized by the appearance of the band at 293 cm^{-1} and 343 cm^{-1} (gold-sulfur cluster vibration [174]) and disappearance of the band at 915 cm^{-1} and 2565 cm^{-1} (thiol S-H bending and stretching vibration) [175]. The band at 521 cm^{-1} and the small band at 982 cm^{-1} assigned to Si vibration and SO_4^{2-} anion respectively [165,176]. The experimental data of the spectra correlate with the calculated vibrational frequencies, and there is a slight shift relative to the simulation.

The changing of orientation of molecular structure on the surface can be characterized by the position and intensity of the main bands at 1077 cm^{-1} and 1590 cm^{-1}. All the SERS assignments of 4-MBA adsorber on bSi/Au substrate presented in Table 7.

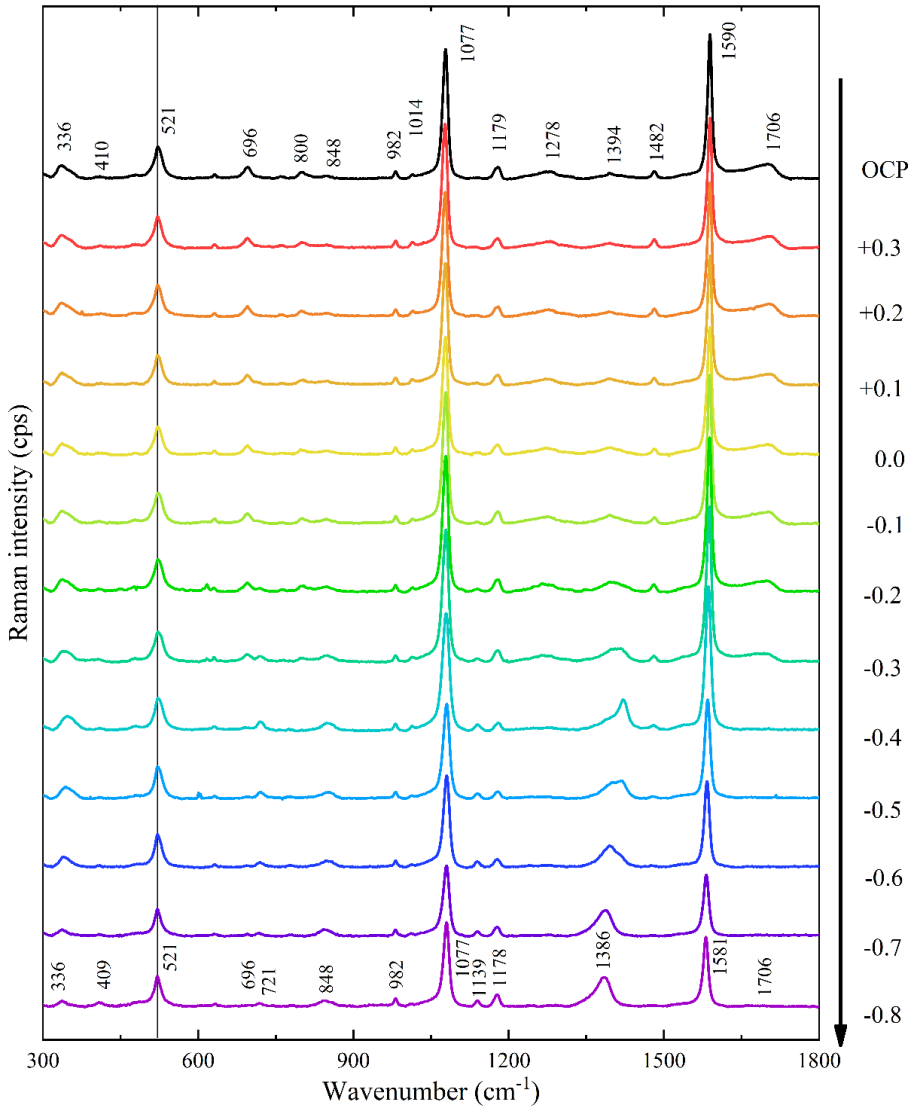

Figure 29. The dependence of the SERS spectra of the 4-MBA solution on the bSi/Au substrate. Excitation wavelength 785 nm, laser power 16,8 mW, integration time 300 s.

Table 7. SERS assignment of SAM of 4-MBA on bSi/Au substrate in 0.1M Na_2SO_4 solution. Excitation wavelength 785 nm, laser power 16,8 mW, integration time 300 s [172].

Wavenumber, cm^{-1} **SERS**		Assignments
OCP	–0.8 V	
296	294 sh	Au–S
336	336	Au–S cluster
410	409	C–S
521	521	Si
696	696	δ (OCO), ν (C–S), in-plane ring compression
–	721	oop w (CCC)
800	802	In-plane ring deformation, ν (C–COOH)
848	848	δ (COO^-)
982	982	$-SO_4^{2-}$
1014	1014 sh	In-plane ring breathing, b_2
1077	1080	aromatic ring breathing mode (ν_{12})
1138	1139	ν (C–COO^-), ν (C–S)
1179	1178	δ (C–H)
1278	1282	–
1394	1386	ν (COO^-)
1482	1482	In-plane δ (C–H)
1590	1581	totally symmetric aromatic ring vibration (ν_{8a})
1706	1705	ν (C=O) of –COOH

Abbreviations: ν – stretching; δ – bending; w – wagging; oop – out of plane; sh– shoulder.

Figure 30(A) presents the normalized intensity of these bands in the range –0.8: +0.3 V. The maximum of the bands in Figure 30(A) indicates the most perpendicular orientation of the benzene ring relative to the surface of the bSi/Au, and the red and blue shifts of the bands at 1590 cm^{-1} and 1077 cm^{-1} (shown in Fig. 30(B)) indicate a reorientation of the phenyl ring and a small change in the tilt angle of the molecule [172,177], which is in good agreement with the previous theoretical model.

According to the Lee.Y and co. [175], when the benzene ring occupies the perpendicular position on the surface, the in-plane modes should be relatively more enhanced than the out-of-plane ring modes. For the 4-MBA molecule the more characteristic bands are the in-plane ring deformation mode at 800 cm^{-1} and the C–H in-plane bending mode at 1482 cm^{-1}. The normalized intensity of this bands presented in Figure 30(A), blue and orange curves. Maximum of the intensity of ν(C–COOH) and δ(C–H) oscillations at –0.1:–0.2 V indicates the most perpendicular orientation of the 4-MBA molecule and changes in the tilt angle of the molecules occurs when the potential of the system changes in the cathodic direction.

The similar tendency observed for the C–S vibration at 410 cm^{-1}. The local maximum is observed at –0.1 V and the intensity is downshifted when the applied potential changes in the cathodic direction. It is also worth noting that at the minimum of the applied potential, the intensity of the 410 cm^{-1} band has another maximum which can indicate the approach of the molecule to the surface of the electrode.

When changing the potential of the system from +0.3 V to –0.8 V occurs, it is possible to observe a change in the intensity and ratio of the bands characterized by the protonated and deprotonated state of the carboxyl –COOH group of 4-MBA. In Figure 29, the main bands under OCP conditions are associated with the protonated state of the carboxyl group of the 4-MBA molecule, but the weak band at 1396 cm^{-1} assigned with the stretching vibration of COO^- indicates the presence of a small number of deprotonated molecules in the system, which can be associated with the low pH of the stock solution [178]. The intensity of the bands at 800 cm^{-1} (ν(C–COOH)) and 1706 cm^{-1} (ν(C=O) of COOH), assigned with a protonated state of 4-MBA molecule, decreases and disappears after –0.3 V. At the same time, the bands 848 cm^{-1}, which characterize the deformation vibrations of the deprotonated COO^- group, and 1138 cm^{-1}, which characterize the vibrations of (C–COO^-), appear at 0.0 V and significantly grow until the –0.8 V. Such an amplification of the bands indicates an increase in the number of deprotonated molecules in the system. The previous band at 1396 cm^{-1} significantly increases in mode intensity and at –0.4V in the 1390–1420 cm^{-1} region an additional band of ν(COO^-) at 1410 cm^{-1} appears [179]. The redshift of this band to 1386 cm^{-1} when the applied potential switches to –0.8 V indicating that 4-MBA molecules with COO^- groups additional adsorbed thought carboxyl groups and have more or less flat orientation to the bSi/Au surface [172].

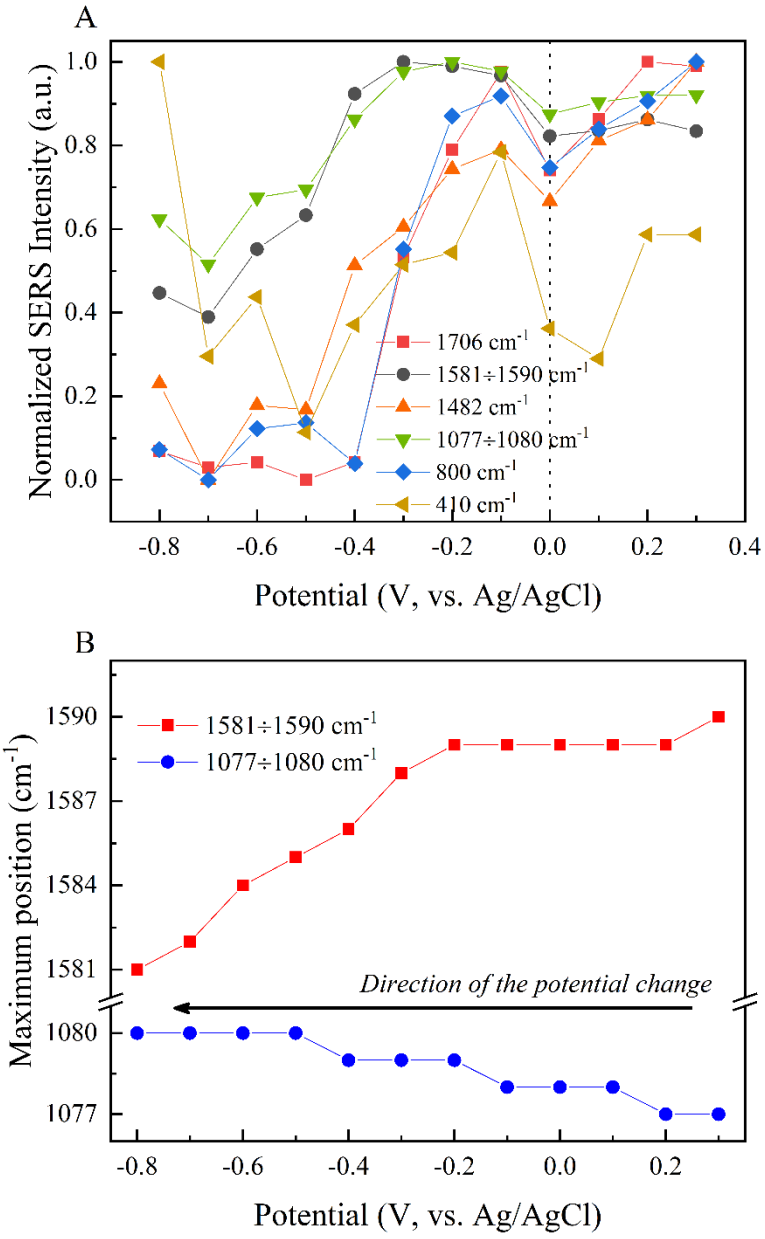

Figure 30. (A) normalized intensities of the characteristic bands of 4-MBA; (B) the position of the 1077 cm^{-1} and 1581 cm^{-1} peaks as a function of potential.

Its spectral behavior closely resembles that of the 1077 and 1590 cm^{-1} which characterizes the most perpendicular position of the molecule relative

to the SERS surface and suggesting that hydrogen bonding may be occurring in some 4-MBA molecules [178].

This tendency characterizes the deprotonation of –COOH group of 4-MBA with the applying potential and may characterize additional adsorption of molecules through the carboxyl group to the bSi/Au surface [172].

As far as the direct applicability of the investigated substrate as a surface for electrochemical experiments is concerned, it can be said with certainty that all changes in the spectrum are only due to changes in the potential. The limit of detection of bSi/Au substrate is 10^{-9} M (non-adsorbed molecule – Doxorubicin) and which makes it possible to detect deprotonated molecules even without applying potential. In the previous work [177,180] the 1396 cm^{-1} band was clearly observed in SERS spectra only in the range after pH 5,6 while the pH value of the stock solution in our experiment is pH 5.1. The reproducible, reliable and reusable bSi/Au substrate has potential to be used as a SERS substrate and working electrode for EC-SERS in the regular measurements.

This was summarized in the **fifth statement** of the thesis: Nanostructured silicon coated by gold can be used as reusable SERS platforms, exhibiting high sensitivity and long-term stability, with potential for practical use as a working electrode for EC-SERS measurements.

CONCLUSIONS

1. Raman and SERS studies of the cyclic Urotensin II (U-II) peptide have revealed a characteristic spectrum of the U-II molecule, which is represented by enhanced bands from aromatic amino acids and low intensity bands from the disulfide bridge and aliphatic part of the molecule.

2. The SERS spectra of U-II on Ag NPs show the interaction of the peptide with the metal surface through the Phe, Tyr and Trp amino acid residues. During adsorption, the disulfide bridge in the cyclic part of the U-II peptide does not break, and the molecule retains its native structure. Protocol of gentle cleaning allows to reduce the intensity of the bands of stabilizers, reducing agents and unstable sample/Ag NPs clusters. During the washing process, additional interactions of U-II peptide through the Asp and Glu amino acid residues occur.

3. The EC-SERS measurements of U-II at the Ag electrode suggest that the adsorption of the peptide occurs mainly through the Phe, Tyr and Trp residues of the cyclic part of the peptide. As the potential of the Ag electrode becomes more negative, the distance between the U-II peptide and the electrode surface decreases; the NH_3^+ group of Lys and –OH group of Tyr residue interact with the silver surface. The exchange of anions in the electrolyte solution (Na_2SO_4-containing solution to $NaClO_4$-containing solution) has no effect on the general mechanism of U-II peptide adsorption.

4. The replacement of metal on the SERS substrate showed a slight change in the mechanism of U-II adsorption on the surface. The SERS spectrum of U-II on the bSi/Au substrate is characterized by the main bands of Trp and Phe residues, and the intensity ratio between the Trp and Phe modes differ compared to the spectra on the Ag surface. The enhanced bands from vibrations of alkyl chains indicate additional adsorption through Lys residue on the bSi/Au surface.

5. Si/Au substrate shows the potential for reusability for various types of molecules (adsorbed and non-adsorbed), and long-term storage of freshly manufactured substrate up to 20 months. The DFT calculations and successful EC-SERS measurements of 4-MBA on bSi/Au substrate show the opportunity to use this substrate as an alternative to classical gold electrode in EC-SERS measurements.

BIBLIOGRAPHY

[1] V. Camarda, A. Rizzi, G. Calò, G. Gendron, S.I. Perron, E. Kostenis, P. Zamboni, F. Mascoli, D. Regoli, Effects of human urotensin II in isolated vessels of various species; comparison with other vasoactive agents, Naunyn-Schmied Arch Pharmacol 365 (2002) 141–149. https://doi.org/10.1007/s00210-001-0503-0.

[2] B. Ross, K. McKendy, A. Giaid, Role of urotensin II in health and disease, American Journal of Physiology-Regulatory, Integrative and Comparative Physiology 298 (2010) R1156–R1172. https://doi.org/10.1152/ajpregu.00706.2009.

[3] E. Haensele, N. Mele, M. Miljak, C.M. Read, D.C. Whitley, L. Banting, C. Delépée, J. Sopkova-de Oliveira Santos, A. Lepailleur, R. Bureau, J.W. Essex, T. Clark, Conformation and Dynamics of Human Urotensin II and Urotensin Related Peptide in Aqueous Solution, J. Chem. Inf. Model. 57 (2017) 298–310. https://doi.org/10.1021/acs.jcim.6b00706.

[4] H. Vaudry, J. Do Rego, J. Le Mevel, D. Chatenet, H. Tostivint, A. Fournier, M. Tonon, G. Pelletier, J. Michael Conlon, J. Leprince, Urotensin II, from fish to human, Annals of the New York Academy of Sciences 1200 (2010) 53–66. https://doi.org/10.1111/j.1749-6632.2010.05514.x.

[5] S.A. Douglas, L. Tayara, E.H. Ohlstein, N. Halawa, A. Giaid, Congestive heart failure and expression of myocardial urotensin II, Lancet 359 (2002) 1990–1997. https://doi.org/10.1016/S0140-6736(02)08831-1.

[6] P.P. Jani, H. Narayan, L.L. Ng, The differential extraction and immunoluminometric assay of Urotensin II and Urotensin-related peptide in heart failure, Peptides 40 (2013) 72–76. https://doi.org/10.1016/j.peptides.2012.12.014.

[7] B.M.Y. Cheung, R. Leung, Y.B. Man, L.Y.F. Wong, Plasma concentration of urotensin II is raised in hypertension, J Hypertens 22 (2004) 1341–1344. https://doi.org/10.1097/01.hjh.0000125452.28861.f1.

[8] A. Balat, M. Büyükçelik, Urotensin-II: More Than a Mediator for Kidney, International Journal of Nephrology 2012 (2012) 249790. https://doi.org/10.1155/2012/249790.

[9] R.A. Silvestre, E.M. Egido, R. Hernandez, J. Leprince, D. Chatenet, H. Tollemer, N. Chartrel, H. Vaudry, J. Marco, Urotensin-II is present in pancreatic extracts and inhibits insulin release in the perfused rat pancreas, European Journal of Endocrinology 151 (2004) 803–809. https://doi.org/10.1530/eje.0.1510803.

[10] S. Flohr, M. Kurz, E. Kostenis, A. Brkovich, A. Fournier, T. Klabunde, Identification of Nonpeptidic Urotensin II Receptor Antagonists by Virtual Screening Based on a Pharmacophore Model Derived from

Structure−Activity Relationships and Nuclear Magnetic Resonance Studies on Urotensin II, J. Med. Chem. 45 (2002) 1799–1805. https://doi.org/10.1021/jm0111043.
[11] E. Lescot, J. Sopkova-de Oliveira Santos, C. Dubessy, H. Oulyadi, A. Lesnard, H. Vaudry, R. Bureau, S. Rault, Definition of New Pharmacophores for Nonpeptide Antagonists of Human Urotensin-II. Comparison with the 3D-structure of Human Urotensin-II and URP, J. Chem. Inf. Model. 47 (2007) 602–612. https://doi.org/10.1021/ci6003948.
[12] K. Takahashi, K. Totsune, Urotensin Peptides, in: Handbook of Biologically Active Peptides, Elsevier, 2013: pp. 1437–1442. https://doi.org/10.1016/B978-0-12-385095-9.00195-0.
[13] E. Smith, G. Dent, Modern Raman spectroscopy: a practical approach, J. Wiley, Hoboken, NJ, 2005.
[14] F. Gaba, W.J. Tipping, M. Salji, K. Faulds, D. Graham, H.Y. Leung, Raman Spectroscopy in Prostate Cancer: Techniques, Applications and Advancements, Cancers 14 (2022) 1535. https://doi.org/10.3390/cancers14061535.
[15] M. de Veij, P. Vandenabeele, K.A. Hall, F.M. Fernandez, M.D. Green, N.J. White, A.M. Dondorp, P.N. Newton, L. Moens, Fast detection and identification of counterfeit antimalarial tablets by Raman spectroscopy, Journal of Raman Spectroscopy 38 (2007) 181–187. https://doi.org/10.1002/jrs.1621.
[16] K.S. Andrikopoulos, S. Daniilia, B. Roussel, K. Janssens, In vitro validation of a mobile Raman–XRF micro-analytical instrument's capabilities on the diagnosis of Byzantine icons, Journal of Raman Spectroscopy 37 (2006) 1026–1034. https://doi.org/10.1002/jrs.1612.
[17] J. Langer, D. Jimenez De Aberasturi, J. Aizpurua, R.A. Alvarez-Puebla, B. Auguié, J.J. Baumberg, G.C. Bazan, S.E.J. Bell, A. Boisen, A.G. Brolo, J. Choo, D. Cialla-May, V. Deckert, L. Fabris, K. Faulds, F.J. García De Abajo, R. Goodacre, D. Graham, A.J. Haes, C.L. Haynes, C. Huck, T. Itoh, M. Käll, J. Kneipp, N.A. Kotov, H. Kuang, E.C. Le Ru, H.K. Lee, J.-F. Li, X.Y. Ling, S.A. Maier, T. Mayerhöfer, M. Moskovits, K. Murakoshi, J.-M. Nam, S. Nie, Y. Ozaki, I. Pastoriza-Santos, J. Perez-Juste, J. Popp, A. Pucci, S. Reich, B. Ren, G.C. Schatz, T. Shegai, S. Schlücker, L.-L. Tay, K.G. Thomas, Z.-Q. Tian, R.P. Van Duyne, T. Vo-Dinh, Y. Wang, K.A. Willets, C. Xu, H. Xu, Y. Xu, Y.S. Yamamoto, B. Zhao, L.M. Liz-Marzán, Present and Future of Surface-Enhanced Raman Scattering, ACS Nano 14 (2020) 28–117. https://doi.org/10.1021/acsnano.9b04224.
[18] G. Niaura, Raman Spectroscopy in Analysis of Biomolecules, in: R.A. Meyers (Ed.), Encyclopedia of Analytical Chemistry, 1st ed., Wiley, 2008. https://doi.org/10.1002/9780470027318.a0212.pub2.
[19] S.R. Panikkanvalappil, M.A. Mahmoud, M.A. Mackey, M.A. El-Sayed, Surface-enhanced Raman spectroscopy for real-time

monitoring of reactive oxygen species-induced DNA damage and its prevention by platinum nanoparticles, ACS Nano 7 (2013) 7524–7533. https://doi.org/10.1021/nn403722x.
[20] M. Fleischmann, P.J. Hendra, A.J. McQuillan, Raman spectra of pyridine adsorbed at a silver electrode, Chemical Physics Letters 26 (1974) 163–166. https://doi.org/10.1016/0009-2614(74)85388-1.
[21] H. Gajera, S. Patel, B. Golakiya, Fundamentals of Biochemistry- A text book, 2008.
[22] L.P. Datta, S. Manchineella, T. Govindaraju, Biomolecules-derived biomaterials, Biomaterials 230 (2020) 119633. https://doi.org/10.1016/j.biomaterials.2019.119633.
[23] Molecules, in: Cell Biology, Elsevier, 2017: pp. 31–52. https://doi.org/10.1016/B978-0-323-34126-4.00003-7.
[24] File:Protein structure (1)-en.svg - Wikipedia, (2022). https://commons.wikimedia.org/wiki/File:Protein_structure_(1)-en.svg (accessed June 25, 2025).
[25] N. Davidenko, R. Cameron, S. Best, Natural Biopolymers for Biomedical Applications, (2019) 162–176. https://doi.org/10.1016/B978-0-12-801238-3.11026-8.
[26] E. Herman, B. Larkins, Protein storage bodies and vacuoles, Plant Cell 11 (1999) 601–614.
[27] J. Kumar, L.K. Narnoliya, A. Alok, Chapter 6 - A CRISPR Technology and Biomolecule Production by Synthetic Biology Approach, in: S.P. Singh, A. Pandey, G. Du, S. Kumar (Eds.), Current Developments in Biotechnology and Bioengineering, Elsevier, 2019: pp. 143–161. https://doi.org/10.1016/B978-0-444-64085-7.00006-X.
[28] D. Pearson, J.E. Shively, B.R. Clark, I.I. Geschwind, M. Barkley, R.S. Nishioka, H.A. Bern, Urotensin II: a somatostatin-like peptide in the caudal neurosecretory system of fishes., Proc. Natl. Acad. Sci. U.S.A. 77 (1980) 5021–5024. https://doi.org/10.1073/pnas.77.8.5021.
[29] H. Tostivint, F.B. Quan, M. Bougerol, N.B. Kenigfest, I. Lihrmann, Impact of gene/genome duplications on the evolution of the urotensin II and somatostatin families, Gen Comp Endocrinol 188 (2013) 110–117. https://doi.org/10.1016/j.ygcen.2012.12.015.
[30] J.M. Conlon, F. O'Harte, D.D. Smith, M.C. Tonon, H. Vaudry, Isolation and primary structure of urotensin II from the brain of a tetrapod, the frog Rana ridibunda, Biochem Biophys Res Commun 188 (1992) 578–583. https://doi.org/10.1016/0006-291x(92)91095-8.
[31] T. Sugo, Y. Murakami, Y. Shimomura, M. Harada, M. Abe, Y. Ishibashi, C. Kitada, N. Miyajima, N. Suzuki, M. Mori, M. Fujino, Identification of urotensin II-related peptide as the urotensin II-immunoreactive molecule in the rat brain, Biochem Biophys Res Commun 310 (2003) 860–868. https://doi.org/10.1016/j.bbrc.2003.09.102.

[32] M. Tal, D.A. Ammar, M. Karpuj, V. Krizhanovsky, M. Naim, D.A. Thompson, A novel putative neuropeptide receptor expressed in neural tissue, including sensory epithelia, Biochem Biophys Res Commun 209 (1995) 752–759. https://doi.org/10.1006/bbrc.1995.1563.

[33] R.S. Ames, H.M. Sarau, J.K. Chambers, R.N. Willette, N.V. Aiyar, A.M. Romanic, C.S. Louden, J.J. Foley, C.F. Sauermelch, R.W. Coatney, Z. Ao, J. Disa, S.D. Holmes, J.M. Stadel, J.D. Martin, W.-S. Liu, G.I. Glover, S. Wilson, D.E. McNulty, C.E. Ellis, N.A. Elshourbagy, U. Shabon, J.J. Trill, D.W.P. Hay, E.H. Ohlstein, D.J. Bergsma, S.A. Douglas, Human urotensin-II is a potent vasoconstrictor and agonist for the orphan receptor GPR14, Nature 401 (1999) 282–286. https://doi.org/10.1038/45809.

[34] H. Castel, L. Desrues, J.-E. Joubert, M.-C. Tonon, L. Prézeau, M. Chabbert, F. Morin, P. Gandolfo, The G Protein-Coupled Receptor UT of the Neuropeptide Urotensin II Displays Structural and Functional Chemokine Features, Front. Endocrinol. 8 (2017). https://doi.org/10.3389/fendo.2017.00076.

[35] F. Merlino, S. Di Maro, A. Munaim Yousif, M. Caraglia, P. Grieco, Urotensin-II Ligands: An Overview from Peptide to Nonpeptide Structures, J Amino Acids 2013 (2013) 979016. https://doi.org/10.1155/2013/979016.

[36] J. Leprince, D. Chatenet, C. Dubessy, A. Fournier, B. Pfeiffer, E. Scalbert, P. Renard, P. Pacaud, H. Oulyadi, I. Ségalas-Milazzo, L. Guilhaudis, D. Davoust, M.-C. Tonon, H. Vaudry, Structure-activity relationships of urotensin II and URP, Peptides 29 (2008) 658–673. https://doi.org/10.1016/j.peptides.2007.08.014.

[37] K. Takahashi, K. Totsune, O. Murakami, S. Shibahara, Expression of urotensin II and urotensin II receptor mRNAs in various human tumor cell lines and secretion of urotensin II-like immunoreactivity by SW-13 adrenocortical carcinoma cells, Peptides 22 (2001) 1175–1179. https://doi.org/10.1016/s0196-9781(01)00441-7.

[38] J.J. Maguire, A.P. Davenport, Is urotensin-II the new endothelin?, British Journal of Pharmacology 137 (2002) 579–588. https://doi.org/10.1038/sj.bjp.0704924.

[39] W.-Y. He, Q. Bai, L.-T. A, C.-S. Tang, A.-H. Zhang, Irisin levels are associated with urotensin II levels in diabetic patients, J Diabetes Investig 6 (2015) 571–576. https://doi.org/10.1111/jdi.12331.

[40] A. Balat, M. Karakök, K. Yılmaz, Y. Kibar, Urotensin-II Immunoreactivity in Children with Chronic Glomerulonephritis, Renal Failure 29 (2007) 573–578. https://doi.org/10.1080/08860220701392108.

[41] J.-C. Do Rego, J. Leprince, E. Scalbert, H. Vaudry, J. Costentin, Behavioral actions of urotensin-II, Peptides 29 (2008) 838–844. https://doi.org/10.1016/j.peptides.2007.12.016.

[42] W. Song, A.E.S. Abdel-Razik, W. Lu, Z. Ao, D.G. Johns, S.A. Douglas, R.J. Balment, N. Ashton, Urotensin II and renal function in the rat, Kidney International 69 (2006) 1360–1368. https://doi.org/10.1038/sj.ki.5000290.
[43] A.Y. Zhang, Y.-F. Chen, D.X. Zhang, F.-X. Yi, J. Qi, P. Andrade-Gordon, L. de Garavilla, P.-L. Li, A.-P. Zou, Urotensin II is a nitric oxide-dependent vasodilator and natriuretic peptide in the rat kidney, Am J Physiol Renal Physiol 285 (2003) F792-798. https://doi.org/10.1152/ajprenal.00342.2002.
[44] J.R. Ferraro, K. Nakamoto, C.W. Brown, Introductory Raman spectroscopy, 2nd ed, Academic Press, Amsterdam ; Boston, 2003.
[45] A. Smekal, Zur Quantentheorie der Dispersion, Naturwissenschaften 11 (1923) 873–875. https://doi.org/10.1007/BF01576902.
[46] C.V. Raman, K.S. Krishnan, A New Type of Secondary Radiation, Nature 121 (1928) 501–502. https://doi.org/10.1038/121501c0.
[47] H.A. Szymanski, ed., Raman Spectroscopy, Springer US, Boston, MA, 1970. https://doi.org/10.1007/978-1-4684-3027-1.
[48] T.H. Maiman, Stimulated Optical Radiation in Ruby, Nature 187 (1960) 493–494. https://doi.org/10.1038/187493a0.
[49] W.J. Tipping, M. Lee, A. Serrels, V.G. Brunton, A.N. Hulme, Stimulated Raman scattering microscopy: an emerging tool for drug discovery, Chem. Soc. Rev. 45 (2016) 2075–2089. https://doi.org/10.1039/C5CS00693G.
[50] S.E.J. Bell, D.T. Burns, A.C. Dennis, L.J. Matchett, J.S. Speers, Composition profiling of seized ecstasy tablets by Raman spectroscopy, Analyst 125 (2000) 1811–1815. https://doi.org/10.1039/B005662F.
[51] D. Bersani, P.P. Lottici, Raman spectroscopy of minerals and mineral pigments in archaeometry, Journal of Raman Spectroscopy 47 (2016) 499–530. https://doi.org/10.1002/jrs.4914.
[52] S. Reitzenstein, P. Rösch, M.A. Strehle, D. Berg, M. Baranska, H. Schulz, E. Rudloff, J. Popp, Nondestructive analysis of single rapeseeds by means of Raman spectroscopy, Journal of Raman Spectroscopy 38 (2007) 301–308. https://doi.org/10.1002/jrs.1643.
[53] M. Baranska, H. Schulz, P. Rösch, M.A. Strehle, J. Popp, Identification of secondary metabolites in medicinal and spice plants by NIR-FT-Raman microspectroscopic mapping, Analyst 129 (2004) 926–930. https://doi.org/10.1039/B408933M.
[54] K.R. Ward, R.W. Barbee, P.S. Reynolds, I.P. Torres Filho, M.H. Tiba, L. Torres, R.N. Pittman, J. Terner, Oxygenation monitoring of tissue vasculature by resonance Raman spectroscopy, Anal Chem 79 (2007) 1514–1518. https://doi.org/10.1021/ac061072x.
[55] P. Rostron, D. Gerber, Raman Spectroscopy, a review, International Journal of Engineering and Technical Research 6 (2016) 50–64.

[56] F. Kuhl, H. Lu, M. Becker, L. Chen, Y. Zheng, A. Polity, Z. Zhang, Y. He, P.J. Klar, Raman scattering of TiV1-O2 thin films on (110) rutile TiO2 in the low and high temperature phase adjacent to the metal–insulator transition, Journal of Raman Spectroscopy 55 (2024) 923–938. https://doi.org/10.1002/jrs.6684.

[57] I. Weber, S.G. Pavlov, U. Böttger, M.P. Reitze, Alteration in the Raman spectra of characteristic rock-forming silicate mixtures due to micrometeorite bombardment, Journal of Raman Spectroscopy 55 (2024) 901–913. https://doi.org/10.1002/jrs.6676.

[58] M.A. Fikiet, S.R. Khandasammy, E. Mistek, Y. Ahmed, L. Halámková, J. Bueno, I.K. Lednev, Surface enhanced Raman spectroscopy: A review of recent applications in forensic science, Spectrochimica Acta Part A: Molecular and Biomolecular Spectroscopy 197 (2018) 255–260. https://doi.org/10.1016/j.saa.2018.02.046.

[59] H.J. Butler, L. Ashton, B. Bird, G. Cinque, K. Curtis, J. Dorney, K. Esmonde-White, N.J. Fullwood, B. Gardner, P.L. Martin-Hirsch, M.J. Walsh, M.R. McAinsh, N. Stone, F.L. Martin, Using Raman spectroscopy to characterize biological materials, Nat Protoc 11 (2016) 664–687. https://doi.org/10.1038/nprot.2016.036.

[60] S. Laing, L.E. Jamieson, K. Faulds, D. Graham, Surface-enhanced Raman spectroscopy for in vivo biosensing, Nat Rev Chem 1 (2017) 1–19. https://doi.org/10.1038/s41570-017-0060.

[61] A. Kudelski, Analytical applications of Raman spectroscopy, Talanta 76 (2008) 1–8. https://doi.org/10.1016/j.talanta.2008.02.042.

[62] U.A. Jayasooriya, R.D. Jenkins, Introduction to Raman Spectroscopy, in: D.L. Andrews, A.A. Demidov (Eds.), An Introduction to Laser Spectroscopy: Second Edition, Springer US, Boston, MA, 2002: pp. 77–104. https://doi.org/10.1007/978-1-4615-0727-7_3.

[63] F. Nicolson, M.F. Kircher, N. Stone, P. Matousek, Spatially offset Raman spectroscopy for biomedical applications, Chem. Soc. Rev. 50 (2021) 556–568. https://doi.org/10.1039/D0CS00855A.

[64] J.C. Tsang, J.R. Kirtley, T.N. Theis, Surface plasmon polariton contributions to strokes emission from molecular monolayers on periodic Ag surfaces, Solid State Communications 35 (1980) 667–670. https://doi.org/10.1016/0038-1098(80)90870-4.

[65] J.A. Creighton, C.G. Blatchford, M.G. Albrecht, Plasma resonance enhancement of Raman scattering by pyridine adsorbed on silver or gold sol particles of size comparable to the excitation wavelength, J. Chem. Soc., Faraday Trans. 2 75 (1979) 790–798. https://doi.org/10.1039/F29797500790.

[66] M. Moskovits, Surface roughness and the enhanced intensity of Raman scattering by molecules adsorbed on metals, The Journal of Chemical Physics 69 (1978) 4159–4161. https://doi.org/10.1063/1.437095.

[67] M.G. Albrecht, J.A. Creighton, Anomalously intense Raman spectra of pyridine at a silver electrode, J. Am. Chem. Soc. 99 (1977) 5215–5217. https://doi.org/10.1021/ja00457a071.
[68] K. Kneipp, Y. Wang, H. Kneipp, L.T. Perelman, I. Itzkan, R.R. Dasari, M.S. Feld, Single Molecule Detection Using Surface-Enhanced Raman Scattering (SERS), Phys. Rev. Lett. 78 (1997) 1667–1670. https://doi.org/10.1103/PhysRevLett.78.1667.
[69] S. Nie, S.R. Emory, Probing Single Molecules and Single Nanoparticles by Surface-Enhanced Raman Scattering, Science 275 (1997) 1102–1106. https://doi.org/10.1126/science.275.5303.1102.
[70] B. Barbiellini, Enhancement of Raman scattering from molecules placed near metal nanoparticles, Low Temperature Physics 43 (2017) 159–161. https://doi.org/10.1063/1.4974193.
[71] M. Mehta, M. Waterland, Ultrasensitive surface-enhanced Raman scattering detection of biological pollutants by controlled evaporation on omniphobic substrates, Heliyon 6 (2020) e04317. https://doi.org/10.1016/j.heliyon.2020.e04317.
[72] J.R. Lombardi, R.L. Birke, T. Lu, J. Xu, Charge-transfer theory of surface enhanced Raman spectroscopy: Herzberg–Teller contributions, The Journal of Chemical Physics 84 (1986) 4174–4180. https://doi.org/10.1063/1.450037.
[73] A. Campion, J.E.I. Ivanecky, C.M. Child, M. Foster, On the Mechanism of Chemical Enhancement in Surface-Enhanced Raman Scattering, J. Am. Chem. Soc. 117 (1995) 11807–11808. https://doi.org/10.1021/ja00152a024.
[74] A. Otto, The 'chemical' (electronic) contribution to surface-enhanced Raman scattering, Journal of Raman Spectroscopy 36 (2005) 497–509. https://doi.org/10.1002/jrs.1355.
[75] R. Pilot, R. Signorini, C. Durante, L. Orian, M. Bhamidipati, L. Fabris, A Review on Surface-Enhanced Raman Scattering, Biosensors 9 (2019) 57. https://doi.org/10.3390/bios9020057.
[76] N. Guillot, M.L. De La Chapelle, The electromagnetic effect in surface enhanced Raman scattering: Enhancement optimization using precisely controlled nanostructures, Journal of Quantitative Spectroscopy and Radiative Transfer 113 (2012) 2321–2333. https://doi.org/10.1016/j.jqsrt.2012.04.025.
[77] P.L. Stiles, J.A. Dieringer, N.C. Shah, R.P.V. Duyne, Surface-Enhanced Raman Spectroscopy, Annual Review of Analytical Chemistry 1 (2008) 601–626. https://doi.org/10.1146/annurev.anchem.1.031207.112814.
[78] S. Cong, X. Liu, Y. Jiang, W. Zhang, Z. Zhao, Surface Enhanced Raman Scattering Revealed by Interfacial Charge-Transfer Transitions, The Innovation 1 (2020) 100051. https://doi.org/10.1016/j.xinn.2020.100051.

[79] A. Falamas, D. Cuibus, N. Tosa, I. Brezestean, C.M. Muntean, K. Milenko, E. Vereshchagina, R. Moldovan, E. Bodoki, C. Farcau, Toward microfluidic SERS and EC-SERS applications via tunable gold films over nanospheres, Discover Nano 18 (2023) 73. https://doi.org/10.1186/s11671-023-03851-3.
[80] I. Pastoriza-Santos, L.M. Liz-Marzán, Colloidal silver nanoplates. State of the art and future challenges, J. Mater. Chem. 18 (2008) 1724–1737. https://doi.org/10.1039/B716538B.
[81] T.T.H. Pham, X.H. Vu, N.D. Dien, T.T. Trang, N.V. Truong, T.D. Thanh, P.M. Tan, N.X. Ca, The structural transition of bimetallic Ag–Au from core/shell to alloy and SERS application, RSC Adv. 10 (2020) 24577–24594. https://doi.org/10.1039/D0RA04132G.
[82] P. Marcus, ed., Corrosion Mechanisms in Theory and Practice, 3rd edition, CRC Press, 2017.
[83] D.-Y. Wu, J.-F. Li, B. Ren, Z.-Q. Tian, Electrochemical surface-enhanced Raman spectroscopy of nanostructures, Chem. Soc. Rev. 37 (2008) 1025–1041. https://doi.org/10.1039/B707872M.
[84] H. Yamada, Y. Yamamoto, N. Tani, Surface-enhanced raman scattering (SERS) of adsorbed molecules on smooth surfaces of metals and a metal oxide, Chemical Physics Letters 86 (1982) 397–400. https://doi.org/10.1016/0009-2614(82)83531-8.
[85] Y. Chen, Y. Hu, G. Li, A Review on Non-Noble Metal Substrates for Surface-Enhanced Raman Scattering Detection, Chemosensors 11 (2023) 427. https://doi.org/10.3390/chemosensors11080427.
[86] P. Miao, J. Wu, Y. Du, Y. Sun, P. Xu, Phase transition induced Raman enhancement on vanadium dioxide (VO2) nanosheets, J. Mater. Chem. C 6 (2018) 10855–10860. https://doi.org/10.1039/C8TC04269A.
[87] J. Chen, K. Sun, Y. Zhang, D. Wu, Z. Jin, F. Xie, X. Zhao, X. Wang, Plasmonic MoO2 nanospheres assembled on graphene oxide for highly sensitive SERS detection of organic pollutants, Anal Bioanal Chem 411 (2019) 2781–2791. https://doi.org/10.1007/s00216-019-01751-z.
[88] X. Ling, W. Fang, Y.-H. Lee, P.T. Araujo, X. Zhang, J.F. Rodriguez-Nieva, Y. Lin, J. Zhang, J. Kong, M.S. Dresselhaus, Raman Enhancement Effect on Two-Dimensional Layered Materials: Graphene, h-BN and MoS2, Nano Lett. 14 (2014) 3033–3040. https://doi.org/10.1021/nl404610c.
[89] X. Tang, Q. Hao, X. Hou, L. Lan, M. Li, L. Yao, X. Zhao, Z. Ni, X. Fan, T. Qiu, Exploring and Engineering 2D Transition Metal Dichalcogenides toward Ultimate SERS Performance, Advanced Materials 36 (2024) 2312348. https://doi.org/10.1002/adma.202312348.
[90] C. Liang, K. Sun, M. Chen, P. Xu, Crystal-Phase Engineering of Two-Dimensional Transition-Metal Dichalcogenides for Surface-Enhanced Raman Scattering: A Perspective, Langmuir 39 (2023) 11946–11953. https://doi.org/10.1021/acs.langmuir.3c01479.

[91] A. Sarycheva, T. Makaryan, K. Maleski, E. Satheeshkumar, A. Melikyan, H. Minassian, M. Yoshimura, Y. Gogotsi, Two-Dimensional Titanium Carbide (MXene) as Surface-Enhanced Raman Scattering Substrate, J. Phys. Chem. C 121 (2017) 19983–19988. https://doi.org/10.1021/acs.jpcc.7b08180.

[92] T.-H. Yu, C.-H. Ho, C.-Y. Wu, C.-H. Chien, C.-H. Lin, S. Lee, Metal–organic frameworks: a novel SERS substrate, Journal of Raman Spectroscopy 44 (2013) 1506–1511. https://doi.org/10.1002/jrs.4378.

[93] X. Liang, N. Li, R. Zhang, P. Yin, C. Zhang, N. Yang, K. Liang, B. Kong, Carbon-based SERS biosensor: from substrate design to sensing and bioapplication, NPG Asia Mater 13 (2021) 1–36. https://doi.org/10.1038/s41427-020-00278-5.

[94] X. Ling, L. Xie, Y. Fang, H. Xu, H. Zhang, J. Kong, M.S. Dresselhaus, J. Zhang, Z. Liu, Can Graphene be used as a Substrate for Raman Enhancement?, Nano Lett. 10 (2010) 553–561. https://doi.org/10.1021/nl903414x.

[95] S. Feng, M.C. dos Santos, B.R. Carvalho, R. Lv, Q. Li, K. Fujisawa, A.L. Elías, Y. Lei, N. Perea-López, M. Endo, M. Pan, M.A. Pimenta, M. Terrones, Ultrasensitive molecular sensor using N-doped graphene through enhanced Raman scattering, Science Advances 2 (2016) e1600322. https://doi.org/10.1126/sciadv.1600322.

[96] W.-J. Ong, L.-L. Tan, Y.H. Ng, S.-T. Yong, S.-P. Chai, Graphitic Carbon Nitride (g-C3N4)-Based Photocatalysts for Artificial Photosynthesis and Environmental Remediation: Are We a Step Closer To Achieving Sustainability?, Chem Rev 116 (2016) 7159–7329. https://doi.org/10.1021/acs.chemrev.6b00075.

[97] D.-Y. Lin, C.-Y. Yu, C.-A. Ku, C.-K. Chung, Design, Fabrication, and Applications of SERS Substrates for Food Safety Detection: Review, Micromachines 14 (2023) 1343. https://doi.org/10.3390/mi14071343.

[98] M.J. Styles, R.S. Rodriguez, V.M. Szlag, S. Bryson, Z. Gao, S. Jung, T.M. Reineke, C.L. Haynes, Optimization of film over nanosphere substrate fabrication for SERS sensing of the allergen soybean agglutinin, Journal of Raman Spectroscopy 52 (2021) 482–490. https://doi.org/10.1002/jrs.6019.

[99] M. Tahghighi, D. Janner, J. Ignés-Mullol, Optimizing Gold Nanoparticle Size and Shape for the Fabrication of SERS Substrates by Means of the Langmuir–Blodgett Technique, Nanomaterials 10 (2020) 2264. https://doi.org/10.3390/nano10112264.

[100] J.C. Hulteen, R.P. Van Duyne, Nanosphere lithography: A materials general fabrication process for periodic particle array surfaces, Journal of Vacuum Science & Technology A 13 (1995) 1553–1558. https://doi.org/10.1116/1.579726.

[101] F. Tian, F. Bonnier, A. Casey, A.E. Shanahan, H.J. Byrne, Surface enhanced Raman scattering with gold nanoparticles: effect of particle

shape, Anal. Methods 6 (2014) 9116–9123. https://doi.org/10.1039/C4AY02112F.
[102] F. Hao, C.L. Nehl, J.H. Hafner, P. Nordlander, Plasmon Resonances of a Gold Nanostar, Nano Lett. 7 (2007) 729–732. https://doi.org/10.1021/nl062969c.
[103] R. Kodiyath, S.T. Malak, Z.A. Combs, T. Koenig, M.A. Mahmoud, M.A. El-Sayed, V.V. Tsukruk, Assemblies of silver nanocubes for highly sensitive SERS chemical vapor detection, J. Mater. Chem. A 1 (2013) 2777–2788. https://doi.org/10.1039/C2TA00867J.
[104] V.S. Tiwari, T. Oleg, G.K. Darbha, W. Hardy, J.P. Singh, P.C. Ray, Non-resonance SERS effects of silver colloids with different shapes, Chemical Physics Letters 446 (2007) 77–82. https://doi.org/10.1016/j.cplett.2007.07.106.
[105] J.F. Li, Y.F. Huang, Y. Ding, Z.L. Yang, S.B. Li, X.S. Zhou, F.R. Fan, W. Zhang, Z.Y. Zhou, D.Y. Wu, B. Ren, Z.L. Wang, Z.Q. Tian, Shell-isolated nanoparticle-enhanced Raman spectroscopy, Nature 464 (2010) 392–395. https://doi.org/10.1038/nature08907.
[106] R. Kattumenu, C.H. Lee, L. Tian, M.E. McConney, S. Singamaneni, Nanorod decorated nanowires as highly efficient SERS-active hybrids, J. Mater. Chem. 21 (2011) 15218–15223. https://doi.org/10.1039/C1JM12426A.
[107] M.K. Francis, B.K. Sahu, P.B. Bhargav, B. C, N. Ahmed, A. Das, S. Dhara, Ag nanowires based SERS substrates with very high enhancement factor, Physica E: Low-Dimensional Systems and Nanostructures 137 (2022) 115080. https://doi.org/10.1016/j.physe.2021.115080.
[108] L. Vigderman, E.R. Zubarev, Starfruit-Shaped Gold Nanorods and Nanowires: Synthesis and SERS Characterization, Langmuir 28 (2012) 9034–9040. https://doi.org/10.1021/la300218z.
[109] R. Aroca, Surface-Enhanced Vibrational Spectroscopy, 1st ed., Wiley, 2006. https://doi.org/10.1002/9780470035641.
[110] G. Niaura, A.K. Gaigalas, V.L. Vilker, Surface-Enhanced Raman Spectroscopy of Phosphate Anions: Adsorption on Silver, Gold, and Copper Electrodes, J. Phys. Chem. B 101 (1997) 9250–9262. https://doi.org/10.1021/jp970097k.
[111] E. Podstawka, Structural properties of bombesin-like peptides revealed by surface-enhanced Raman scattering on roughened silver electrodes, Biopolymers 89 (2008) 980–992. https://doi.org/10.1002/bip.21047.
[112] A. Brewer, K. von Haeften, In situ passivation and blue luminescence of silicon clusters using a cluster beam/H2O codeposition production method, Applied Physics Letters 94 (2009) 261102. https://doi.org/10.1063/1.3167355.
[113] Y. Qu, H. Zhou, X. Duan, Porous silicon nanowires, Nanoscale 3 (2011) 4060–4068. https://doi.org/10.1039/C1NR10668F.

[114] M.S. Schmidt, J. Hübner, A. Boisen, Large area fabrication of leaning silicon nanopillars for surface enhanced Raman spectroscopy, Adv Mater 24 (2012) OP11-18. https://doi.org/10.1002/adma.201103496.
[115] Z. Kang, Y. Liu, S.-T. Lee, Small-sized silicon nanoparticles: new nanolights and nanocatalysts, Nanoscale 3 (2011) 777–791. https://doi.org/10.1039/C0NR00559B.
[116] Z. Zhang, M. Zhang, Y. Wang, Q. Tan, X. Lv, Z. Zhong, H. Li, F. Su, Amorphous silicon–carbon nanospheres synthesized by chemical vapor deposition using cheap methyltrichlorosilane as improved anode materials for Li-ion batteries, Nanoscale 5 (2013). https://doi.org/10.1039/c3nr00635b.
[117] A. Javey, S. Nam, R.S. Friedman, H. Yan, C.M. Lieber, Layer-by-layer assembly of nanowires for three-dimensional, multifunctional electronics, Nano Lett 7 (2007) 773–777. https://doi.org/10.1021/nl063056l.
[118] I. Talian, K. Mogensen, A. Orinak, D. Kaniansky, J. Hübner, Surface-enhanced Raman spectroscopy on novel black silicon-based nanostructured surfaces, Journal of Raman Spectroscopy 40 (2009) 982–986. https://doi.org/10.1002/jrs.2213.
[119] L. Golubewa, A. Klimovich, I. Timoshchenko, Y. Padrez, M. Fetisova, H. Rehman, P. Karvinen, A. Selskis, S. Adomavičiūtė-Grabusovė, I. Matulaitienė, A. Ramanavicius, R. Karpicz, T. Kulahava, Y. Svirko, P. Kuzhir, Stable and Reusable Lace-like Black Silicon Nanostructures Coated with Nanometer-Thick Gold Films for SERS-Based Sensing, ACS Appl. Nano Mater. 6 (2023) 4770–4781. https://doi.org/10.1021/acsanm.3c00281.
[120] R.W. Williams, [14] Protein secondary structure analysis using Raman amide I and amide III spectra, in: Methods in Enzymology, Academic Press, 1986: pp. 311–331. https://doi.org/10.1016/0076-6879(86)30016-8.
[121] N.C. Maiti, M.M. Apetri, M.G. Zagorski, P.R. Carey, V.E. Anderson, Raman spectroscopic characterization of secondary structure in natively unfolded proteins: alpha-synuclein, J Am Chem Soc 126 (2004) 2399–2408. https://doi.org/10.1021/ja0356176.
[122] N.S. Myshakina, Z. Ahmed, S.A. Asher, Dependence of Amide Vibrations on Hydrogen Bonding, J. Phys. Chem. B 112 (2008) 11873–11877. https://doi.org/10.1021/jp8057355.
[123] N. Kuhar, S. Sil, T. Verma, S. Umapathy, Challenges in application of Raman spectroscopy to biology and materials, RSC Adv. 8 (2018) 25888–25908. https://doi.org/10.1039/C8RA04491K.
[124] P. Bazylewski, R. Divigalpitiya, G. Fanchini, In situ Raman spectroscopy distinguishes between reversible and irreversible thiol modifications in l -cysteine, RSC Advances 7 (2017) 2964–2970. https://doi.org/10.1039/C6RA25879D.

[125] H.E. Van Wart, A. Lewis, H.A. Scheraga, F.D. Saeva, Disulfide bond dihedral angles from Raman spectroscopy, Proc Natl Acad Sci U S A 70 (1973) 2619–2623. https://doi.org/10.1073/pnas.70.9.2619.
[126] D.E. Schlamadinger, J.E. Gable, J.E. Kim, Hydrogen Bonding and Solvent Polarity Markers in the UV Resonance Raman Spectrum of Tryptophan: Application to Membrane Proteins, J. Phys. Chem. B 113 (2009) 14769–14778. https://doi.org/10.1021/jp905473y.
[127] T. Miura, H. Takeuchi, I. Harada, Characterization of individual tryptophan side chains in proteins using Raman spectroscopy and hydrogen-deuterium exchange kinetics, Biochemistry 27 (1988) 88–94. https://doi.org/10.1021/bi00401a015.
[128] B. Hernández, Y.-M. Coïc, F. Pflüger, S.G. Kruglik, M. Ghomi, All characteristic Raman markers of tyrosine and tyrosinate originate from phenol ring fundamental vibrations, Journal of Raman Spectroscopy 47 (2016) 210–220. https://doi.org/10.1002/jrs.4776.
[129] E. Daublytė, M. Kalnaitytė, A. Klimovich, A. Drabavičius, T. Charkova, Synthesis of silver nanoparticles with polyols under reflux and microwave irradiation conditions, Chemija 34 (2023). https://doi.org/10.6001/chemija.2023.34.3.1.
[130] L. Golubewa, H. Rehman, Y. Padrez, A. Basharin, S. Sumit, I. Timoshchenko, R. Karpicz, Y. Svirko, P. Kuzhir, Black Silicon: Breaking through the Everlasting Cost vs. Effectivity Trade-Off for SERS Substrates, Materials 16 (2023) 1948. https://doi.org/10.3390/ma16051948.
[131] D. Whitaker, K. Hayes, A Simple Algorithm for Despiking Raman Spectra, (2018). https://doi.org/10.26434/chemrxiv.5993011.v2.
[132] M.J. Frisch, G.W. Trucks, H.B. Schlegel, G.E. Scuseria, M.A. Robb, J.R. Cheeseman, G. Scalmani, V. Barone, B. Mennucci, G.A. Petersson, H. Nakatsuji, M. Caricato, X. Li, H.P. Hratchian, A.F. Izmaylov, J. Bloino, G. Zheng, D.J. Sonnenb, Gaussian 09, Revision D.01; Gaussian Inc., Wallingford, CT., 2013., (n.d.). https://gaussian.com/g09citation/ (accessed March 20, 2025).
[133] M. Talaikis, O. Eicher-Lorka, G. Valincius, G. Niaura, Water-Induced Structural Changes in the Membrane-Anchoring Monolayers Revealed by Isotope-Edited SERS, J. Phys. Chem. C 120 (2016) 22489–22499. https://doi.org/10.1021/acs.jpcc.6b07686.
[134] A. Klimovich, L. Golubewa, Y. Padrez, I. Matulaitiene, Characterization of human Urotensin II peptide adsorbed on silver electrode by surface-enhanced Raman scattering spectroscopy, Spectrochimica Acta Part A: Molecular and Biomolecular Spectroscopy 329 (2025) 125565. https://doi.org/10.1016/j.saa.2024.125565.
[135] E. Podstawka-Proniewicz, G. Niaura, L.M. Proniewicz, Neuromedin C: Potential-Dependent Surface-Enhanced Raman Spectra in the Far-

Red Spectral Region on Silver, Gold, and Copper Surfaces, J. Phys. Chem. B 114 (2010) 5117–5124. https://doi.org/10.1021/jp910575f.
[136] E. Podstawka-Proniewicz, A. Kudelski, Y. Kim, L.M. Proniewicz, Adsorption of neurotensin-family peptides on SERS-active Ag substrates, Journal of Raman Spectroscopy 43 (2012) 1196–1203. https://doi.org/10.1002/jrs.4034.
[137] E. Podstawka, G. Niaura, L.M. Proniewicz, Potential-Dependent Studies on the Interaction between Phenylalanine-Substituted Bombesin Fragments and Roughened Ag, Au, and Cu Electrode Surfaces, J. Phys. Chem. B 114 (2010) 1010–1029. https://doi.org/10.1021/jp909268c.
[138] M.N. Siamwiza, R.C. Lord, M.C. Chen, T. Takamatsu, I. Harada, H. Matsuura, T. Shimanouchi, Interpretation of the doublet at 850 and 830 cm $^{-1}$ in the Raman spectra of tyrosyl residues in proteins and certain model compounds, Biochemistry 14 (1975) 4870–4876. https://doi.org/10.1021/bi00693a014.
[139] E. Podstawka, E. Sikorska, L.M. Proniewicz, B. Lammek, Raman and surface-enhanced Raman spectroscopy investigation of vasopressin analogues containing 1-aminocyclohexane-1-carboxylic acid residue, Biopolymers 83 (2006) 193–203. https://doi.org/10.1002/bip.20545.
[140] B. Hernández, Y.-M. Coïc, S.G. Kruglik, C. Carelli, R. Cohen, M. Ghomi, Octreotide Used for Probing the Type-II′ β-Turn CD and Raman Markers, J. Phys. Chem. B 116 (2012) 9337–9345. https://doi.org/10.1021/jp3036428.
[141] N.N. Brandt, A.Yu. Chikishev, A.V. Golovin, V.N. Kruzhilin, A.O. Zalevsky, Raman spectroscopy of disulfide bridges in thrombin, Biomedical Spectroscopy and Imaging 3 (2014) 287–292. https://doi.org/10.3233/BSI-140081.
[142] C.H. GÖRbitz, Conformational properties of disulphide bridges. 2. Rotational potentials of diethyl disulphide, J of Physical Organic Chem 7 (1994) 259–267. https://doi.org/10.1002/poc.610070508.
[143] I. Ignatjev, E. Podstawka-Proniewicz, G. Niaura, J.R. Lombardi, L.M. Proniewicz, Potential Induced Changes in Neuromedin B Adsorption on Ag, Au, and Cu Electrodes Monitored by Surface-Enhanced Raman Scattering, J. Phys. Chem. B 115 (2011) 10525–10536. https://doi.org/10.1021/jp2026863.
[144] S.L. Han, J.E. Rivier, H.A. Scheraga, Conformational studies of somatostatin and selected analogues by Raman spectroscopy, Int J Pept Protein Res 15 (1980) 355–364. https://doi.org/10.1111/j.1399-3011.1980.tb02912.x.
[145] K. Krishnan, R.S. Krishnan, Raman and infrared spectra of ethylene glycol, Proc. Indian Acad. Sci. 64 (1966) 111. https://doi.org/10.1007/BF03047675.
[146] L. Gontrani, P. Tagliatesta, A. Agresti, S. Pescetelli, M. Carbone, New Insights into the Structure of Glycols and Derivatives: A Comparative

X-Ray Diffraction, Raman and Molecular Dynamics Study of Ethane-1,2-Diol, 2-Methoxyethan-1-ol and 1,2-Dimethoxy Ethane, Crystals 10 (2020) 1011. https://doi.org/10.3390/cryst10111011.
[147] S. Pattanayak, A. Swarnkar, A. Priyam, G.M. Bhalerao, Citrate–hydrazine hydrogen-bonding driven single-step synthesis of tunable near-IR plasmonic, anisotropic silver nanocrystals: implications for SERS spectroscopy of inorganic oxoanions, Dalton Trans. 43 (2014) 11826–11833. https://doi.org/10.1039/C4DT01091D.
[148] O. Pandoli, R.D.S. Martins, E.C. Romani, S. Paciornik, M.H.D.P. Maurício, H.D.L. Alves, F.V. Pereira-Meirelles, E.L. Luz, S.M.L. Koller, H. Valiente, K. Ghavami, Colloidal silver nanoparticles: an effective nano-filler material to prevent fungal proliferation in bamboo, RSC Adv. 6 (2016) 98325–98336. https://doi.org/10.1039/C6RA12516F.
[149] E. Podstawka, Y. Ozaki, L.M. Proniewicz, Adsorption of S—S Containing Proteins on a Colloidal Silver Surface Studied by Surface-Enhanced Raman Spectroscopy, Appl Spectrosc 58 (2004) 1147–1156. https://doi.org/10.1366/0003702042336073.
[150] E. Podstawka, M. Andrzejak, P. Kafarski, L.M. Proniewicz, Comparison of adsorption mechanism on colloidal silver surface of alafosfalin and its analogs, Journal of Raman Spectroscopy 39 (2008) 1238–1249. https://doi.org/10.1002/jrs.1977.
[151] N. Nogami, H. Sugeta, T. Miyazawa, C–S Stretching Vibrations and Molecular Conformations of Isobutyl Methyl Sulfide and Related Alkyl Sulfides, Bulletin of the Chemical Society of Japan 48 (1975) 2417–2420. https://doi.org/10.1246/bcsj.48.2417.
[152] K.M. Sanchez, G. Kang, B. Wu, J.E. Kim, Tryptophan-Lipid Interactions in Membrane Protein Folding Probed by Ultraviolet Resonance Raman and Fluorescence Spectroscopy, Biophysical Journal 100 (2011) 2121–2130. https://doi.org/10.1016/j.bpj.2011.03.018.
[153] E. Podstawka-Proniewicz, I. Ignatjev, G. Niaura, L.M. Proniewicz, Phe-MetNH2 Terminal Bombesin Subfamily Peptides: Potential Induced Changes in Adsorption on Ag, Au, and Cu Electrodes Monitored by SERS, J. Phys. Chem. C 116 (2012) 4189–4200. https://doi.org/10.1021/jp2126027.
[154] P.G. Hildebrandt, R.A. Copeland, T.G. Spiro, J. Otlewski, M. Laskowski, F.G. Prendergast, Tyrosine hydrogen-bonding and environmental effects in proteins probed by ultraviolet resonance Raman spectroscopy, Biochemistry 27 (1988) 5426–5433. https://doi.org/10.1021/bi00415a007.
[155] M. Pazderková, L. Bednárová, H. Dlouhá, M. Flegel, M. Lebl, J. Hlaváček, V. Setnička, M. Urbanová, S. Hynie, V. Klenerová, V. Baumruk, P. Maloň, Electronic and vibrational optical activity of several peptides related to neurohypophyseal hormones: disulfide

group conformation, Biopolymers 97 (2012) 923–932. https://doi.org/10.1002/bip.22105.
[156] F. Madzharova, Z. Heiner, J. Kneipp, Surface Enhanced Hyper-Raman Scattering of the Amino Acids Tryptophan, Histidine, Phenylalanine, and Tyrosine, J. Phys. Chem. C 121 (2017) 1235–1242. https://doi.org/10.1021/acs.jpcc.6b10905.
[157] E. Proniewicz, D. Skołuba, I. Ignatjev, G. Niaura, D. Sobolewski, A. Prahl, L.M. Proniewicz, Influence of applied potential on bradykinin adsorption onto Ag, Au, and Cu electrodes, J Raman Spectroscopy 44 (2013) 655–664. https://doi.org/10.1002/jrs.4246.
[158] E. Podstawka, G. Niaura, Potential-Dependent Characterization of Bombesin Adsorbed States on Roughened Ag, Au, and Cu Electrode Surfaces at Physiological pH, J. Phys. Chem. B 113 (2009) 10974–10983. https://doi.org/10.1021/jp903847c.
[159] V. Reipa, A. Gaigalas, S. Abramowitz, Conformational alterations of bovine insulin adsorbed on a silver electrode, Journal of Electroanalytical Chemistry 348 (1993) 413–428. https://doi.org/10.1016/0022-0728(93)80147-A.
[160] C. Spedalieri, J. Plaickner, E. Speiser, N. Esser, J. Kneipp, Ultraviolet Resonance Raman Spectra of Serum Albumins, Appl Spectrosc 77 (2023) 1044–1052. https://doi.org/10.1177/00037028231183728.
[161] H. Takeuchi, Raman structural markers of tryptophan and histidine side chains in proteins, Biopolymers 72 (2003) 305–317. https://doi.org/10.1002/bip.10440.
[162] M. Foggia, P. Taddei, A. Torreggiani, M. Dettin, A. Tinti, Self-assembling peptides for biomedical applications: IR and Raman spectroscopies for the study of secondary structure, Proteomics Research Journal 2 (2012) 231–272.
[163] R.P.D. Bank, RCSB PDB - 6HVB: NMR structure of Urotensin Peptide Asp-c[Cys-Phe-(N-Me)Trp-Lys-Tyr-Cys]-Val in SDS solution, (n.d.). https://www.rcsb.org/structure/6hvb (accessed August 15, 2024).
[164] F. Merlino, É. Billard, A.M. Yousif, S. Di Maro, D. Brancaccio, L. Abate, A. Carotenuto, R. Bellavita, R. d'Emmanuele Di Villa Bianca, P. Santicioli, L. Marinelli, E. Novellino, T.E. Hébert, W.D. Lubell, D. Chatenet, P. Grieco, Functional Selectivity Revealed by N-Methylation Scanning of Human Urotensin II and Related Peptides, J. Med. Chem. 62 (2019) 1455–1467. https://doi.org/10.1021/acs.jmedchem.8b01601.
[165] W.W. Rudolph, G. Irmer, A Raman spectroscopic investigation of speciation in La2(SO4)3(aq), RSC Adv. 5 (2015) 84999–85008. https://doi.org/10.1039/C5RA16900C.
[166] A. Antić-Jovanović, M. Jeremić, M. Lalić, D.A. Long, Raman spectral study of the Mg(ClO4)2□NaNCS□H2O system at ambient and elevated temperatures, Journal of Raman Spectroscopy 20 (1989) 523–528. https://doi.org/10.1002/jrs.1250200808.

[167] T. Nikitin, L. Khriachtchev, Optical and Structural Properties of Si Nanocrystals in SiO2 Films, Nanomaterials 5 (2015) 614–655. https://doi.org/10.3390/nano5020614.
[168] P.E. Laibinis, C.D. Bain, R.G. Nuzzor, G.M. Whitesides, Structure and wetting Properties of w-Alkoxy-n-alkanethiolate Monolayers on Gold and Silver, Journal Of Physical Chemistry (1995) 7663–76.
[169] D.K. Lambert, Vibrational Stark effect of adsorbates at electrochemical interfaces, Electrochimica Acta 41 (1996) 623–630. https://doi.org/10.1016/0013-4686(95)00349-5.
[170] X. Zhao, M. Chen, DFT study on the influence of electric field on surface-enhanced Raman scattering from pyridine–metal complex, Journal of Raman Spectroscopy 45 (2014) 62–67. https://doi.org/10.1002/jrs.4422.
[171] Y. Zhang, Y. Shao, W. Zhang, Y. Feng, W. Lin, DFT studies of surface-enhanced Raman spectroscopy of 1,4-benzenedithiol–Au2 complex under the effect of static electric fields, Journal of Raman Spectroscopy 47 (2016) 310–315. https://doi.org/10.1002/jrs.4822.
[172] A. Michota, J. Bukowska, Surface-enhanced Raman scattering (SERS) of 4-mercaptobenzoic acid on silver and gold substrates, Journal of Raman Spectroscopy 34 (2003) 21–25. https://doi.org/10.1002/jrs.928.
[173] A. Capocefalo, D. Mammucari, F. Brasili, C. Fasolato, F. Bordi, P. Postorino, F. Domenici, Exploring the Potentiality of a SERS-Active pH Nano-Biosensor, Front. Chem. 7 (2019). https://doi.org/10.3389/fchem.2019.00413.
[174] B. Varnholt, P. Oulevey, S. Luber, C. Kumara, A. Dass, T. Bürgi, Structural Information on the Au–S Interface of Thiolate-Protected Gold Clusters: A Raman Spectroscopy Study, J. Phys. Chem. C 118 (2014) 9604–9611. https://doi.org/10.1021/jp502453q.
[175] S.B. Lee, K. Kim, M.S. Kim, Surface-enhanced Raman scattering of o-mercaptobenzoic acid in silver sol, Journal of Raman Spectroscopy 22 (1991) 811–817. https://doi.org/10.1002/jrs.1250221214.
[176] Y. Katharria, S. Kumar, F. Singh, J. Pivin, D. Kanjilal, Synthesis of buried SiC using an energetic ion beam, Journal of Physics D: Applied Physics 39 (2006) 3969. https://doi.org/10.1088/0022-3727/39/18/007.
[177] Y. Liu, H. Yuan, A.M. Fales, T. Vo-Dinh, pH-sensing nanostar probe using surface-enhanced Raman scattering (SERS): theoretical and experimental studies, Journal of Raman Spectroscopy 44 (2013) 980–986. https://doi.org/10.1002/jrs.4302.
[178] S.W. Bishnoi, C.J. Rozell, C.S. Levin, M.K. Gheith, B.R. Johnson, D.H. Johnson, N.J. Halas, All-optical nanoscale pH meter, Nano Lett 6 (2006) 1687–1692. https://doi.org/10.1021/nl060865w.
[179] A. Williams, K.J. Flynn, Z. Xia, P.R. Dunstan, Multivariate spectral analysis of pH SERS probes for improved sensing capabilities, Journal of Raman Spectroscopy 47 (2016) 819–827. https://doi.org/10.1002/jrs.4910.

[180] B.T. Scarpitti, A.M. Morrison, M. Buyanova, Z.D. Schultz, Comparison of 4-Mercaptobenzoic Acid Surface-Enhanced Raman Spectroscopy-Based Methods for pH Determination in Cells, Appl Spectrosc 74 (2020) 1423–1432. https://doi.org/10.1177/0003702820950768.

SANTRAUKA

ĮVADAS

Biologinių molekulių įvairovė – baltymų, nukleorūgščių, angliavandenių, lipidų – yra fundamentali gyvų organizmų pagrindo dalis. Šios molekulės atlieka įvairias funkcijas: nuo energijos tiekimo ir struktūrinės atramos iki genetinės informacijos kodavimo, taip pat dalyvauja cheminėse reakcijose. Technologijų ir biomolekulinių įrankių vystymasis, leido giliau suprasti vykstančius procesus, surinkti ir įsisavinti informaciją mikro ir makro lygiu. Biomolekulės dėl savo įvairovės ir atliekamų funkcijų yra svarbus taikinys moksliniams tyrimams leidžiantis suprasti: atskirų molekulių struktūrą; funkcijas; tarpusavio sąveikos mechanizmus. Taip atskirų biomolekulių tyrimai padėjo geriau suprasti daugelį procesų, vykstančių organizme, dalis jų tapo biomolekuliniais įrankiais, o dalis biologiniais vaistai.

Viena tokių molekulių – Urotensino II peptidas, pasižymintis kraujagysles sutraukiančiu poveikiu, panašiu į endotelino-1 [1]. Žmogaus Urotensino II peptidas (U-II) yra ciklinis neuropeptidas, pirmą kartą buvo išskirtas iš teleost žuvų *Gillichthys mirabilis* [2] ir ilgą laiką manyta, kad jįs sekretuojamas tik žuvų urofizėje. Jau yra nustatyta, kad visi U-II izopeptidai turi konservatyvią C-galinę dalį c-[Cys–Phe–Trp–Lys–Tyr–Cys], sudarytą iš šešių amino rūgščių sujungtų disulfidinių tilteliu ir kintančią N-galinę dalį [3], pasitaiko kelioms rūšims (žiurkėms, kiaulėms, gobiams, beždžionėms), įskaitant žmones [4]. Buvo pastebėta, kad U-II peptidas ir jo signalinė sistema pasižymi tiek neuromediatoriaus ir tiek neuromoduliatoriaus savybėmis, geba slopinti gliukozės sukeltą insulino sekreciją ir gali būti potencialus taikinys priešuždegiminių vaistų kūrimui [5-8]. Iki šiol yra daugiausia yra sukaupta žinių apie šio peptido biologinį aktyvumą, tačiau informacijos apie pačios molekulės fizines savybes nepakanka. ^{1}H-NMR spektroskopijos ir molekulinės dinamikos metodais [9,10] nustatytos žmogaus U-II peptido konformacijos vandeniniuose tirpaluose. Deja, molekulės unikalumas apsunkina jos struktūrinę analizės ir sąveikos su receptoriais tyrimus, kas komplikuoja U-II analogų paieškas farmacinėms ir medicininėms reikmėms [11].

Ramano spektroskopija yra vienas iš virpesinės spektroskopijos metodų, leidžiančių kokybiniu ir kiekybiniu lygiu tirti įvairias molekules [12,13]. Kaip kiekviena medžiaga turi savitą struktūrą, taip ir unikalų Ramano spektrą, kuris veikia kaip molekulės "piršto atspaudas" [14,15]. Naudojantis Ramano spektroskopija galima gauti daug informacijos apie biologines molekules, taip pat ir peptidus. Šis metodas gali suteikti informacija apie peptidų ir baltymų

antrinę struktūrą, ryšius molekulės viduje, funkcinės grupes, molekulių tarpusavio sąveiką ir kt. [16-18]. Tačiau, Ramano spektroskopija nėra jautrus metodas ir reikalauja didelių medžiagos koncentracijų dirbant vandeniniuose tirpaluose. Šią problemą išspendė atradimas, kad Ramano signalai gali būti sustiprinti sužadinant lokalizuotų paviršiaus plazmono rezonansus (LPPR) ant šiurkščių metalinių paviršių adsorbuotoms molekulėms, lėmė paviršiaus sustiprintos Ramano spektroskopijos (PSRS) metodo atsiradimą. Dėl paviršiaus stiprinimo šis metodas išplėtė molekulių aptikimo ribas nuo mažų koncentracijų [19] iki vienos molekulės tyrimų [20] ir perkėlė mokslinius tyrimus į kitą lygį. Tad PSRS kaip ir Ramano spektroskopija atrado savo nišą daugelyje pramonės ir mokslo sričių, taip pat imtas taikyti ir biomolekulių tyrimuose. Ramano spektroskopija ir jos metodai suteikia informacija apie pokyčius molekulėse molekuliniu lygiu, jos sąveiką su aplinka, orientacija, erdvinius pokyčius, aplinkos pokyčius. PSRS metodas apjungtas su elektrochemija dar labiau praplečia metodo galimybes, nes valdant elektrodo potencialą, parenkant tirpalo elementus atsiranda galimybė imituoti sąlygas ląstelėje ir eksperimentus atlikti *in situ*.

Disertacijos tikslas ir uždaviniai

Pagrindinis darbo tikslas – ištirti ciklinio peptido žmogaus Urotensino-II struktūrą molekuliniame lygmenyje, išsiaiškinti jo adsorbcijos ypatumus ant skirtingos prigimties ir struktūros metalų paviršių, taip pat išsiaiškinti jo sąveikos su skirtingos prigimties anijonais ypatumus.

Šiam tikslui pasiekti buvo iškeltos **5 užduotys**:
1. Užregistruoti ir išanalizuoti ciklinio peptido žmogaus Urotensino II (U-II) Ramano ir PSRS spektrus;
2. Ištirti peptido adsorbcijos mechanizmą ant sidabro nanodalelių (Ag NDs) ir įvertinti papildomo plovimo proceso poveikį;
3. Nustatyti elektrocheminio potencialo, anijono ir metalo prigimties įtaką U-II peptido adsorbcijos mechanizmui;
4. Įvertinti juodojo silicio/aukso (bSi/Au) substratų tinkamumą daugkartiniam naudojimui PSRS matavimuose;
5. Taikant kvantinės chemijos skaičiavimus, įvertinti galimybę naudoti bSi/Au substratą kaip darbinį elektrodą vietoj klasikinio aukso elektrodo.

Naujumas ir aktualumas

Šiame darbe pirmą kartą buvo užregistruoti ir priskirti ciklinio peptido žmogaus Urotensin-II Ramano ir PSRS virpesiniai spektrai. Ramano spektre dominuoja virpesinės juostos, kurios priskiriamos aromatinėms amino rūgščių liekanoms (fenilalanino, triptofano, tirozino), esančioms ciklinėje peptido dalyje, bei S-S tilteliui tarp dviejų cisteino radikalų. Nustatyta, kad peptido natyvioje būsenoje disulfidinio tiltelio –CSSC– fragmentuose dominuoja P_C–T konformacija.

Taip pat buvo užregistruoti U-II adsorbuoto ant Ag NP, struktūrizuoto Ag elektrodo, bSi / Au substrato PSRS spektrai ir palyginti. Nustatyta, kad peptidas su metalu linkęs sąveikauti per ciklinėje dalyje esančias, amino rūgščių liekanas, adsorbcijos metu disulfidinis tiltelis nenutrūksta, o jo konformacija išlieka ta pati kaip ir natyvioje būsenoje. Amido I ir Amido III virpesių buvimas patvirtina ciklinę peptido struktūrą. Pastebėta, kad lyginant su Ag paviršiumi ant Au peptidas linkęs adsorbuotis per Trp ir alkilines grupes, ypač Lys.

Elektrocheminiais matavimais buvo parodyta, kad neigiamėjant potencialui atstumas tarp elektrodo ir peptido mažėja, o keičiant elektrodo potencialą galimą keisti molekulės orientaciją. Kartu buvo atliktas anijono pakeitimas iš Na_2SO_4 į $NaClO_4$, kuris parodė, kad anijono prigimtis didelės įtakos adsorbcijos mechanizmui neturi. Ateityje šie EC-PSRS tyrimai gali būti išplėsti ir pritaikyti modeliuojant U-II molekulės sąveikos su jos receptoriumi mechanizmą.

Papildomai buvo atlikti eksperimentiniai tyrimai su modeliniais junginiais ant bSi / Au substratų, kurie parodė, kad šie substratai yra tinkami daugkartiniam naudojimui. Buvo nustatyta, kad biologinį modelinį junginį DOX galima aptikti 10^{-9}-10^{-4} M koncentracijų ribose, o pačių substratų PSRS signalų stiprinimas išlieka iki 20 mėnesių. Taip pat buvo atlikti DFT modeliavimas modeliniam junginiui 4-MBA ant Au paviršiaus elektriniame laukia ir sulyginti su eksperimentiniais duomenimis. Tai parodė, kad bSi / Au substratai tinkami EC-PSRS matavimams elektrocheminėse celėse.

Disertacijos ginamieji teiginiai

1. Urotensino II peptido adsorbrcijos metu ant metalo paviršiaus disulfidinis tiltelis tarp dviejų cisteinų nenutrūksta, o sąveika su metalo paviršiumi vyksta per ciklinėje dalyje esančias aromatines amino rūgščių liekanas;

2. Adsorbcijos metu U-II pakeičia citrato anijonus ant sidabro paviršiaus, o praplovimo proceso metu pilnai pakeičia išplautus citrato anijonus sąveikaudamas per Asp ir Glu amino rūgščių liekanas;

3. Keičiantis sistemos potencialui, molekulė persiorientuoja elektrodo atžvilgiu, ir vyksta papildoma Lys liekanos adsorbcija. Neigiamėjant Ag elektrodo potencialui, mažėja atstumas tarp U-II peptido ir elektrodo paviršiaus. Anijonų pakeitimas sistemoje (iš Na_2SO_4 į $NaClO_4$) didelės įtakos U-II peptido adsorbcijos mechanizmui neturi;

4. Metalo prigimtis didelės įtakos U-II peptido adsorbcijai neturi, ant aukso paviršiaus molekulė labiau linkusi adsorbuotis per Trp ir Lys

5. BSi/ Au substratai gali būti panaudojami kaip daugkartiniai PSRS padėklai, pasižymintys dideliu jautriu ir ilgaamžiškumu, rodo praktinio naudojimo kaip darbinio elektrodo EC-PSRS matavimams potencialą.

REZULTATAI

Urotensin II peptido Ramano spektrai

Žmogaus Urotensin II (U-II, NH–Glu–Thr–Pro–Asp–Cys–Phe–Trp–Lys–Tyr–Cys–Val–OH) yra ciklinė peptidas, turintis neurohormonams būdingą aktyvumą. Pirmą kartą buvo atrasta 1969 m. Gobio žuvyse, vėliau jis buvo aptiktas ir žinduoliuose, tarp jų ir žmoguje. Visi U-II peptidai sudaryti iš dviejų dalių iš C- galinės liekanos, kuri yra koncervatyvi ir N-galinės liekanos, kuri kinta savo amino rūgščių seka ir ilgiu. C-galą sudaro heksapeptidas CFWKYC, sujungtas disulfidiniu tilteliu tarp dviejų cisteinų. Dėl savo unikalios struktūros peptido ciklinėje dalyje susidaro viduvandenilinės jungtys ir jis gali turėti 11 konformerų. N-galas cilkinės dalies atžvilgiu gali būti dviejose konformacijoje.

Ramano spektruose vyrauja būdingos aromatinės AA virpesių juostos iš ciklinės molekulės dalies – Phe, Trp ir Tyr. Pagrindinės Phe virpesinės juostos yra fenilo žiedas, kvėpuojantis virpesys ties 1003 cm^{-1} (ν_{12}), –CH valentiniai virpesiai plokštumoje ties 1032 cm^{-1} (ν_{18a}), ν(C–C) šoninės grandinės virpesiai 1205 cm^{-1} (ν_{7a}). Intensyvios juostos padėtys prie 758 cm^{-1}, 1012 cm^{-1}, 1437 cm^{-1}, 1550 cm^{-1} ir 1605 cm^{-1} buvo priskirtos Trp pirolio žiedo (ν_{18}) kvėpavimo virpesių modai, fenilo ir pirolio žiedo neplokštuminiams kvėpavimo virpesiams, pirolio žiedo valentiniam ir benzeno deformaciniam virpesiui, pirolio žiedo valentiniam virpesiui (ν(C=C)), bei benzeno ir indolo žiedų valentinių virpesių modai. Dubletas ties 1340 ir 1357 cm^{-1} leidžia identifikuoti triptofaną. Kitos intensyvios Ramano juostos, ties 831 cm^{-1} ir 856 cm^{-1}, yra pagrindinės Tyr dubleto virpesines modas, kurios priskiriamos Fermi

rezonansui tarp žiedo lenkimo virpesių plokštumoje ($2\nu_{16a}$) para-pakeistame benzene ir žiedinės kvėpavimo modos (ν_1). Peptidų antrinę struktūrą nusakantys virpesiai stebimi 1240–1270 cm^{-1} ir 1660–1680 cm^{-1} Ramano spektrų ruožuose, kurie atitinka Amidą III ir Amidą I. Pagal virpesinių juostų buvimą šiuose ruožuose ne tik galimą nustatyti baltymų/peptidų buvimą bandiniuose, bet ir daug išsiaiškinti apie jo antrinę struktūrą. Natyvioje būsėnoje U-II peptide dominuoja II'β-klostys, tai galima stebėti iš Ramano spektre esančių juostų ties 1260 cm^{-1} ir 1680 cm^{-1}. 508 cm^{-1} moda buvo priskirta S-S disulfidinio tiltelio valentiniam virpesiui tarp Cys^5–Cys^{10} AA peptido molekulėje. Aukštų dažnių srityje ties 2800-3200 cm^{-1} virpesines modos ties 2882 cm^{-1}, 2932 cm^{-1}, 2975 cm^{-1} buvo priskirtos alifatinių molekulės dalių virpesiams $\nu(CH_2)$ ir $\nu(CH_3)$, o juosta ties 3064 cm^{-1} priskirta Phe ir Trp fenilo žiedo ν (=C–H) virpesiui. U-II peptide Ramano spektrai buvo priskirti remiantis ankstesniais Vazopresin/Neuromedin B superšeimos peptidų ir kitų mažų baltymų Ramano/PSRS tyrimais.

Žmogaus U-II peptido adsorbcijos tyrimai ant skirtingos prigimties ir struktūros metalų paviršių PSRS metodu

U-II peptido adsorbcijos tyrimai ant sidabro nanodalelių PSRS metodu

U-II peptido PSRS spektroskopiniams tyrimams buvo atrinkti du skirtingi metalai (Au ir Ag), kurie buvo skirtingai struktūrizuoti struktūrizuoti.

Pirmieji PSRS spektrai buvo gauti naudojant sidabro nanodaleles (Ag NDs), kurių dydis 65±5 nm [21]. Nanodalelės buvo sumaišytos su U-II peptidu santykiu 1:1, o gauta suspensija paskleista ant plieno paviršiaus ir išdžiovinta. PSRS spektruose stebimos pagrindinės juostos, kurios atitinka tiriamo peptido Ramano signalus, tačiau yra stebimos ir papildomos juostos. Šios virpesinės juostos pagrinde buvo priskirtos nanodalelių sintezėje naudojamiems redukcijos ir paviršių stabilizuojantiems junginiams: natrio citratui ir dietilenglikoliui.

Siekiant sumažinti minėtų molekulių juostų intensyvumą, buvo pasiūlyta "švelni" plovimo procedūra: plaunant išdžiovintą suspensijos lašą vandens srove 5–10 sekundžių. Dėl to sumažėjo juostų ties 721, 810, 1043, 1276, 1455 cm^{-1} intensyvumas, kas rodo, kad plovimo proceso metu citrato anijono ir dietilenglikolį galima dalinai pašalinti iš bandinių. Plovimo metu peptido molekulės labiau priartėja prie Ag paviršiaus ir pakeičia citrato anijono vietas sąveikaudamos su Ag paviršiumi per Asp ir Glu amino rūgščių liekanas. Pagrindinės U-II peptido virpesinės juostos, stebimos PSRS spektre, yra fenilalanino amino rūgšties liekanos fenilo žiedo svyravimai ties 621, 1002,

1032, 1177, 1591 cm^{-1}, triptofano amino rūgšties liekanos fenilo ir pirolo žiedų virpesiai 758, 878, 1369, 1539 cm^{-1}, ir tirozino virpesiai 643, 835, 850 cm^{-1}. Kaip ir natyvioje būsenoje sąveikos su metalo paviršiumi metu -CSSC- fragmentas išlaiko P_C–T konfirmacijoje, ka rodo juosta ties 508 cm^{-1}, priskirta ν(S–S) virpesiui.

Iš to galima daryti išvadą, kad adsorbcijos su metalo paviršiumi metu peptidas pakeičia citrato anijonus Asp ir Glu, disulfidinis tiltelis nenutrūksta, o pagrindinė adsorbcija vyksta per ciklinėje dalyje esančias aromatinių amino rūgščių liekanas.

U-II peptido adsorbcijos tyrimai ant sidabro elektrodo EC-PSRS metodu

Tam kad galėtume tirti ir modeliuoti procesus vykstančius gyvuose organizmuose savo eksperimentus perkėlėme į elektrocheminę celę. Eksperimento metu buvo skleidžiamas elektrodo potencialas, ir keičiama buferinio tirpalo sudėtis, tiksliau – vykdomas anijono pakeitimas (Na_2SO_4 ir $NaClO_4$), stebint, kaip sistemos pokyčiai lemia peptido adsorbciją ant Ag elektrodo paviršiaus. Esant stacionarioms sąlygoms sistemoje (0,1 M Na_2SO_4 ir 0,01 M NaH_2PO_4) molekulė su paviršiumi sąveikauja savo cikline dalimi, paviršiaus spektruose galima stebėti Phe, Trp ir Tyr būdingus virpesius, taip pat stebima disulfidinio tiltelio tarp Cys^5–Cys^{10} liekanų, Amido I bei Amido III virpesių modos.

Esant –1,0 V potencialui, U-II PSRS spektre stebimos Phe, Trp ir Tyr. būdingos intensyvios virpesių modos ties 757, 826/850, 874, 1003, 1030, 1205, 1344/1356, 1538, 1563 ir 1606 cm^{-1}. Šių virpesinių modų intensyvumas gali rodyti atstumą prie paviršiaus. Kai elektrodo potencialas yra –1,0 V, U-II molekulė yra labiausiai priartėjusi prie Ag paviršiaus. Skleidžiant elektrodo potencialą nuo –1,0 V iki 0,0 V, molekulė tolsta nuo paviršiaus ir persiorientuoja. Tai galima stebėti, nes virpesinių juostų intensyvumas sumažėja, ties –0,4 V pasiekia minimalias reikšmes ir pradeda augti. Tai patvirtina Trp dviejų virpesių modų intensyvumo santykio pokytis $I_{1344/1356}$, kuris yra aplinkos hidrofobiškumo žymuo. Jo dinamika su minimalia verte ties –0,4 V, patvirtina Trp indolo žiedo perorientavimą elektrodo paviršiaus atžvilgiu.

Elektrocheminėje sistemoje, pakeitus Na_2SO_4 į $NaClO_4$, pastebėjome, intensyvesnius ν (S–S) (503 cm^{-1}), Amido III (1265 cm^{-1}) ir Amido I (1670 cm^{-1}) virpesius, rodančius didesnį peptido afiniškumą metalui. Tad galima daryti išvadą, kad anijono pakeitimas iš Na_2SO_4 į $NaClO_4$ nesukelia

reikšmingų pokyčių U-II peptido adsorbcijos mechanizme ant elektrodo paviršiaus.

U-II peptido, DOX ir 4-MBA adsorbcijos tyrimai ant bSi/Au substrato EC-PSRS metodu

Paskutinis U-II peptido tyrimo etapas buvo palyginti jo sąveikos su sidabru ir aukso paviršiumi ypatumus. Tam tikslui buvo pasirinktas auksu dengti juodo silicio padėklas (bSi/Au) ir elektrochemiškai šiurkštintas sidabro elektrodas. Dar 2020 m. pristatė Golubewa ir kt. parodė [22], kad bSi/Au padėklai pasižymi aukštu stiprinimu (stiprinimo koeficientas 10^6) ir turi homogenišką paviršių.

Palyginus U-II peptido PSRS spektrus ant Au ir Ag metalų paviršių galima stebėti panašias tendencijas. Kaip ir sidabro atveju adsorbcijos, ant aukso paviršiaus metu disulfidinis tiltelis nenutrūksta. Peptidas sąveikauja su metalu per Phe, Trp ir Tyr, kurios yra ciklinėje peptido dalyje; tiesa sąveika per Trp yra stipresnė nei per Phe, ką rodo juostų intensyvumų skirtumai. Buvo pastebėta, kad padidėjo ν(C–C) virpesinių juostų intensyvumas ties 1075 cm^{-1} ir 1118 cm^{-1}, kuris rodo ne tik sąveiką per lizino šonines grandines, bet ir patvirtina stipresnę metalo sąveiką per Trp indolo žiedą.

Tolimesniam darbo etapui su bSi/Au substratais buvo pasirinkti du modeliniai junginiai: biologinė molekulė doksorubicinas (DOX) ir merkaptobenzoinė rūgštis (4-MBA). Buvo parodyta, kad bSi/Au substratų PSRS signalų stiprinimas išlieka iki 20 mėnesių, o jų paviršių galima atnaujinti deguonies plazma. Buvo nustatyta, kad DOX galima aptikti 10^{-9}-10^{-4} M koncentracijų ribose.

Papildomai buvo atlikti DFT modeliavimas modeliniam junginiui 4-MBA ant Au paviršiaus elektriniame laukia ir sulyginti su eksperimentiniais duomenimis. Remiantis teorinio modeliavimo duomenimis, galima teigti, kad virpesinių juostų intensyvumas priklauso nuo molekulinių grupių poliarizacijos, kurią lemia krūvio perdavimas tarp 4-MBA ir Au substrato, o molekulės struktūros ir orientacijos paviršiaus atžvilgiu pokytis yra minimalus.

Suformavus 4-MBA monosluoksį ant bSi/Au substrato, 4-MBA PSRS spektrams būdingi du stiprūs signalai, ties 1077 cm^{-1} ir 1590 cm^{-1}, kurie priskiriami aromatinio žiedo kvėpavimo virpesių modai (ν_{12}) ir visiškai simetriškai aromatinio žiedo (ν_{8a}) fenilo žiedo virpesių modai. Kai sistemos potencialas buvo pakeistas nuo +0,3 iki –0,8 V, pagrindiniai pokyčiai įvyko virpesių modose, apibūdinančiose 4-MBA karboksilo (–COOH) grupės protonuotą ir deprotonuotą būseną. 848 cm^{-1} ir 1138 cm^{-1} vipesių modos,

atitinkamai priskirtos deprotonuotos COO- grupės deformacinėms virpesių modoms ir (C–COO–) virpesiams, jos atsiranda ties 0,0 V ir žymiai sustiprėja iki –0,8 V. Protonuotą 4-MBA molekulės būseną apibūdinančių virpesinių modų ties 800 cm^{-1} (ν(C–COOH)) ir 1706 cm^{-1} (ν(C=O) COOH) intensyvumas mažėja, ir kai sistemos potencialas yra –0,3 V, jos išnyksta. alentinių virpesių COO– modos intensyvumas padidėja, o kai elektrodo potencialas pasiekia –0,8 V, jos dažnis pasislenka į raudonąją sritį iki 1386 cm^{-1}, ta rodo, kad 4-MBA molekulės su COO^- grupėmis papildomai adsorbuojasi ant paviršiaus ir įgauna horizontalesnę orientaciją bSi/Au paviršiaus atžvilgiu. Iš to galima daryti išvadą, kad ant bSi/Au substrato paviršiaus galima formuoti stabilius savitvarkius monosluoksnius, o pačius substratus taikyti EC-PSRS matavimams.

IŠVADOS

1. Ramano ir PSRS spektroskopijos būdu buvo nustatyta, kad ciklinio peptido Urotensino II (U-II) virpesiniuose spektruose dominuoja aromatinių aminorūgščių virpesinės juostos, o mažesnio intensyvumo juostos atitinka disulfidinį tiltelį ir alifatinę molekulės dalį.

2. U-II PSRS spektrai ant sidabro nanodalelių (Ag NDs) rodo, kad peptidas sąveikauja su metalo paviršiumi per fenilalanino (Phe), tirozino (Tyr) ir triptofano (Trp) aminorūgščių liekanas. Adsorbcijos metu disulfidinis tiltelis ciklinėje U-II peptido dalyje nenutrūksta, o molekulė išlaiko natyvią struktūrą. Švelnus valymo protokolas sumažina stabilizatorių, redukuojančių medžiagų ir nestabilių mėginio/Ag NDs klasterių juostų intensyvumą. Plovimo metu atsiranda papildoma U-II sąveika per asparto (Asp) ir glutamo (Glu) rūgščių liekanas.

3. EC-PSRS nustatyta, kad U-II su Ag elektrodo paviršiumi pagrindinė adsorbcija vyksta per ciklinės dalies Phe, Tyr ir Trp liekanas. Neigiamėjant Ag elektrodo potencialui, mažėja atstumas tarp U-II peptido ir elektrodo paviršiaus, Lizino (Lys) NH_3^+ grupė ir Tirozino –OH grupė sąveikauja su sidabro paviršiumi. Anijonų pakeitimas (iš Na_2SO_4 į $NaClO_4$) elektrolito tirpale neturi reikšmingo poveikio bendrai U-II peptido adsorbcijos mechanizmui.

4. Nustatyta, kad pakeitus metalą PSRS padėkle, U-II adsorbcijos mechanizmui didelės įtakos neturi. U-II PSRS spektras ant bSi/Au pagrindo pasižymi pagrindinėmis Trp ir Phe liekanų juostomis, o Trp ir Phe modų intensyvumo santykis skiriasi, palyginti su spektrais ant sidabro paviršiaus. Sustiprintos alkilo grandinių virpesinės juostos rodo papildomą adsorbciją per Lys liekaną ant Au paviršiaus.

5. BSi/Au substratas rodo įvairių tipų molekulių (adsorbuotų ir neadsorbuotų) pakartotinio naudojimo potencialą ir ilgalaikį šviežiai pagaminto substrato laikymą iki 20 mėnesių. DFT skaičiavimai ir sėkmingi 4-MBA EC-PSRS matavimai bSi/Au substrate rodo galimybę naudoti šį substratą kaip alternatyvą klasikiniam aukso elektrodui atliekant EC-PSRS matavimus.

BIBLIOGRAFIJA

[1] V. Camarda, A. Rizzi, G. Calò, G. Gendron, S. I. Perron, E. Kostenis, P. Zamboni, F. Mascoli, D. Regoli. Effects of human urotensin II in isolated vessels of various species; comparison with other vasoactive agents. Naunyn-Schmied Arch Pharmacol 365, 141–149 (2002). https://doi.org/10.1007/s00210-001-0503-0.

[2] A. Balat, M. Büyükçelik, Urotensin-II: More Than a Mediator for Kidney, International Journal of Nephrology 2012 (2012) 249790. https://doi.org/10.1155/2012/249790.

[3] R.A. Silvestre, E.M. Egido, R. Hernandez, J. Leprince, D. Chatenet, H. Tollemer, N. Chartrel, H. Vaudry, J. Marco, Urotensin-II is present in pancreatic extracts and inhibits insulin release in the perfused rat pancreas, European Journal of Endocrinology 151 (2004) 803–809. https://doi.org/10.1530/eje.0.1510803.

[4] H. Vaudry, J. Do Rego, J. Le Mevel, D. Chatenet, H. Tostivint, A. Fournier, M. Tonon, G. Pelletier, J. Michael Conlon, J. Leprince, Urotensin II, from fish to human, Annals of the New York Academy of Sciences 1200 (2010) 53–66. https://doi.org/10.1111/j.1749-6632.2010.05514.x.

[5] A. Douglas, L. Tayara, E.H. Ohlstein, N. Halawa, A. Giaid, Congestive heart failure and expression of myocardial urotensin II, Lancet 359 (2002) 1990–1997. https://doi.org/10.1016/S0140-6736(02)08831-1.

[6] P.P. Jani, H. Narayan, L.L. Ng, The differential extraction and immunoluminometric assay of Urotensin II and Urotensin-related peptide in heart failure, Peptides 40 (2013) 72–76. https://doi.org/10.1016/j.peptides.2012.12.014.

[7] B.M.Y. Cheung, R. Leung, Y.B. Man, L.Y.F. Wong, Plasma concentration of urotensin II is raised in hypertension, J Hypertens 22 (2004) 1341–1344. https://doi.org/10.1097/01.hjh.0000125452.28861.f1.

[8] A. Balat, M. Büyükçelik, Urotensin-II: More Than a Mediator for Kidney, International Journal of Nephrology 2012 (2012) 249790. https://doi.org/10.1155/2012/249790.

[9] E. Haensele, N. Mele, M. Miljak, C.M. Read, D.C. Whitley, L. Banting, C. Delépée, J. Sopkova-de Oliveira Santos, A. Lepailleur, R. Bureau, J.W. Essex, T. Clark, Conformation and Dynamics of Human Urotensin II and Urotensin Related Peptide in Aqueous Solution, J. Chem. Inf. Model. 57 (2017) 298–310. https://doi.org/10.1021/acs.jcim.6b00706.

[10] E. Lescot, J. Sopkova-de Oliveira Santos, C. Dubessy, H. Oulyadi, A. Lesnard, H. Vaudry, R. Bureau, S. Rault, Definition of New Pharmacophores for Nonpeptide Antagonists of Human Urotensin-II. Comparison with the 3D-structure of Human Urotensin-II and URP, J. Chem. Inf. Model. 47 (2007) 602–612. https://doi.org/10.1021/ci6003948.

[11] K. Takahashi, K. Totsune, Urotensin Peptides, in: Handbook of Biologically Active Peptides, Elsevier, 2013: pp. 1437–1442. https://doi.org/10.1016/B978-0-12-385095-9.00195-0.

[12] E. Smith, G. Dent, Modern Raman spectroscopy: a practical approach, J. Wiley, Hoboken, NJ, 2005.

[13] F. Gaba, W.J. Tipping, M. Salji, K. Faulds, D. Graham, H.Y. Leung, Raman Spectroscopy in Prostate Cancer: Techniques, Applications and Advancements, Cancers 14 (2022) 1535. https://doi.org/10.3390/cancers14061535.

[14] M. de Veij, P. Vandenabeele, K.A. Hall, F.M. Fernandez, M.D. Green, N.J. White, A.M. Dondorp, P.N. Newton, L. Moens, Fast detection and identification of counterfeit antimalarial tablets by Raman spectroscopy, Journal of Raman Spectroscopy 38 (2007) 181–187. https://doi.org/10.1002/jrs.1621.

[15] K.S. Andrikopoulos, S. Daniilia, B. Roussel, K. Janssens, In vitro validation of a mobile Raman–XRF micro-analytical instrument's capabilities on the diagnosis of Byzantine icons, Journal of Raman Spectroscopy 37 (2006) 1026–1034. https://doi.org/10.1002/jrs.1612.

[16] J. Langer, D. Jimenez De Aberasturi, J. Aizpurua, R.A. Alvarez-Puebla, B. Auguié, J.J. Baumberg, G.C. Bazan, S.E.J. Bell, A. Boisen, A.G. Brolo, J. Choo, D. Cialla-May, V. Deckert, L. Fabris, K. Faulds, F.J. García De Abajo, R. Goodacre, D. Graham, A.J. Haes, C.L. Haynes, C. Huck, T. Itoh, M. Käll, J. Kneipp, N.A. Kotov, H. Kuang, E.C. Le Ru, H.K. Lee, J.-F. Li, X.Y. Ling, S.A. Maier, T. Mayerhöfer, M. Moskovits, K. Murakoshi, J.-M. Nam, S. Nie, Y. Ozaki, I. Pastoriza-Santos, J. Perez-Juste, J. Popp, A. Pucci, S. Reich, B. Ren, G.C. Schatz, T. Shegai, S. Schlücker, L.-L. Tay, K.G. Thomas, Z.-Q. Tian, R.P. Van Duyne, T. Vo-Dinh, Y. Wang, K.A. Willets, C. Xu, H. Xu, Y. Xu, Y.S. Yamamoto, B. Zhao, L.M. Liz-Marzán, Present and Future of Surface-Enhanced Raman Scattering, ACS Nano 14 (2020) 28–117. https://doi.org/10.1021/acsnano.9b04224.

[17] G. Niaura, Raman Spectroscopy in Analysis of Biomolecules, in: R.A. Meyers (Ed.), Encyclopedia of Analytical Chemistry, 1st ed., Wiley, 2008. https://doi.org/10.1002/9780470027318.a0212.pub2.

[18] S.R. Panikkanvalappil, M.A. Mahmoud, M.A. Mackey, M.A. El-Sayed, Surface-enhanced Raman spectroscopy for real-time monitoring of reactive oxygen species-induced DNA damage and its prevention by platinum nanoparticles, ACS Nano 7 (2013) 7524–7533. https://doi.org/10.1021/nn403722x.

[19] M. Fleischmann, P.J. Hendra, A.J. McQuillan, Raman spectra of pyridine adsorbed at a silver electrode, Chemical Physics Letters 26 (1974) 163–166. https://doi.org/10.1016/0009-2614(74)85388-1.

[20] K. Kneipp, Y. Wang, H. Kneipp, L.T. Perelman, I. Itzkan, R.R. Dasari, M.S. Feld, Single Molecule Detection Using Surface-Enhanced Raman Scattering (SERS), Phys. Rev. Lett. 78 (1997) 1667–1670. https://doi.org/10.1103/PhysRevLett.78.1667.

[21] E. Daublytė, M. Kalnaitytė, A. Klimovich, A. Drabavičius, T. Charkova, Synthesis of silver nanoparticles with polyols under reflux and microwave irradiation conditions, Chemija 34 (2023). https://doi.org/10.6001/chemija.2023.34.3.1.

[22] L. Golubewa, A. Klimovich, I. Timoshchenko, Y. Padrez, M. Fetisova, H. Rehman, P. Karvinen, A. Selskis, S. Adomavičiūtė-Grabusovė, I. Matulaitienė, A. Ramanavicius, R. Karpicz, T. Kulahava, Y. Svirko, P. Kuzhir, Stable and Reusable Lace-like Black Silicon Nanostructures Coated with Nanometer-Thick Gold Films for SERS-Based Sensing, ACS Appl. Nano Mater. 6 (2023) 4770–4781. https://doi.org/10.1021/acsanm.3c00281.

LIST OF CONFERENCES AND PUBLICATIONS

PUBLICATIONS INCLUDED IN THE THESIS

1. L.Golubewa, **A.Klimovich**, I.Timoshchenko, Y.Padrez, M.Fetisova, H.Rehman, P.Karvinen, A.Selskis, S.Adomavičiūtė-Grabusovė, I.Matulaitienė, A.Ramanavicius, R.Karpicz, T.Kulahava, Y.Svirko, P.Kuzhir. Stable and Reusable Lace-like Black Silicon Nanostructures Coated with Nanometer-Thick Gold Films for SERS-Based Sensing. *ACS Applied Nano Materials, 2023, 6, 6, 4770–4781*. DOI: 10.1021/acsanm.3c00281

Author's contribution: Experimental study, Raman and SERS measurements, analysis of SERS data.

2. E.Daublytė, M.Kalnaitytė, **A.Klimovich**, A. Drabavičius, T. Charkova. Synthesis of silver nanoparticles with polyols under reflux and microwave irradiation conditions**.** *Chemija, 2023, 34, 3, 113–122*. DOI: 10.6001/chemija.2023.34.3.1

Author's contribution: Raman measurements, analysis of SERS data.

3. **A.Klimovich**, L.Golubewa, Y.Padrez, I.Matulaitienė. Characterization of Human Urotensin II Peptide Adsorbed on Silver Electrode by Surface-Enhanced Raman Scattering Spectroscopy. *Spectrochimica Acta Part A: Molecular and Biomolecular Spectroscopy, 2025, 329, 1386-1425.* DOI: 10.1016/j.saa.2024.125565

Author's contribution: EC-SERS measurements, analysis of EC-SERS data, evaluation and interpretation of data, writing the article.

4. **A.Klimovich**, T.Charkova, I.Matulaitienė. Characterization of the Urotensin II peptide by SERS using silver nanoparticles. *Journal of Raman Spectroscopy, 2025,* DOI: 10.1002/jrs.6800

Author's contribution: Raman/SERS measurements, analysis of Raman/SERS data, evaluation and interpretation of data, writing the article.

LIST OF CONFERENCES

1. **A.Klimovich**, L.Golubewa, M.Fetisova, I.Matulaitienė, R.Karpicz, P.Karvinen, P.Kuzhir. Stable and uniform black silicon-based SERS-active substrates for the detection of analytes with a high potential for reusability. ADVANCED MATERIALS AND TECHNOLOGIES 2021 (Poster), August 2021, Palanga, Lithuania.

2. L.Golubewa, **A.Klimovich**, M.Fetisova, T.Kulahava, I.Matulaitienė, R.Karpicz, P.Karvinen, P.Kuzhir. Graphene quantum dot characterization using black silicon-based SERS substrate. CCT-2021 (Poster), September 2021, Vilnius, Lithuania.

3. **A.Klimovich**, L.Golubewa, M.Fetisova, I.Matulaitienė, R.Karpicz, P.Karvinen, P.Kuzhir. SERS-active substrates based on black silicon for the detection of analytes with a high potential for reusability and storage. FizTech-2021 (Poster)**,** October 2021, Vilnius, Lithuania.

4. **A.Klimovich**, S.Adomavičiūtė-Grabusovė, H.Rehman, P.Kuzhir, I.Matulaitienė. Surface-Enhanced Raman Spectroscopy of potential induced changes in human Urotensin II. CCT-2022 (Poster), September 2022, Kaunas, Lithuania.

5. **A.Klimovich**, S.Adomavičiūtė-Grabusovė, H.Rehman, P.Kuzhir, I.Matulaitienė. Human Urotensin II: Surface-Enhanced Raman Spectroscopy of potentially induced changes. FizTech-2022 (Oral presentation), October 2022, Vilnius, Lithuania.

6. **A.Klimovich**, T.Charkova, I.Matulaitiene. Characterization of the Urotensin-II peptide by nanoparticle-enhanced Raman spectroscopy. ADVANCED MATERIALS AND TECHNOLOGIES 2023 (Poster), August 2023, Palanga, Lithuania.

7. **A.Klimovich**, T.Charkova, I.Matulaitiene. Characterization of the Urotensin-II peptide by SERS using silver nanoparticles. FizTech-2023 (Oral presentation), October 2023, Vilnius, Lithuania.

PUBLICATION NOT INCLUDED IN THE THESIS

1. L.Golubewa, T.Kulahava, **A.Klimovich**, D.Rutkauskas, I.Matulaitiene, R.Karpicz, N.Belko, D. Mogilevtsev, A.Kavalenka, M.Fetisova, P.Karvinen, Y.Svirko, P.Kuzhir. Visualizing hypochlorous acid production by human neutrophils with fluorescent graphene quantum dots. *Nanotechnology, 2022, 33, 9, 0951.* DOI: 10.1088/1361-6528/ac3ce4

Brief information about the author

Aliona Klimovich
Republic of Belarus, Orsha city

Education

High school №1 Orsha city, Republic of Belarus / **2000 – 2013**
Certificate with honors

Belorussian State University, Chemical faculty / **2013 – 2018**
Bachelor. Specialty – radiation chemistry;
Topic of the thesis: Cytoprotective action of acyl produced space-screened aminophenol under conditions of halogenating stress (head of PhD, docent Professor Semenkova G. N.)
From the 3rd year A. Klimovich worked on a research project at the Department of radiation chemistry and chemical and pharmaceutical technologies. Topic: Influence of acyl derivatives of spatially shielded aminophenol on neutrophil functions.

Center for Physical Sciences and Technology, Department of Organic Chemistry, Laboratory of Spectroelectrochemistry / **2020 – 2024**
Doctoral studies

Work experience

Chemist, Production company “Effective systems of packaging” / **2018 – 2019**

Engineer, Online-school “World of Math” / **2019 – 2020**

Junior researcher, Center for Physical Sciences and Technology / **2020 – 2025**

ACKNOWLEDGEMENTS

In conclusion, I would like to thank my supervisor dr. Ieva Matulaitienė and all my colleagues at the Department of Organic Chemistry, FTMC. Thanks to your support and expert opinions, many ideas and hypotheses were turned into whole experiments and scientific articles.

Thanks to dr. Tatjana Charkova for guiding me on the right track and taking care of many aspects of my life.

I would like to say a thanks to my colleagues and friends from the Department of Molecular Compound Physics, dr. Lena Golubewa, and dr. Yaraslau Padrez, for your knowledge, experience and determination even to the most adventurous proposals.

I would also like to thank my first scientific supervisors, dr. Semenkova Galina Nikolaevna and dr. Zholnerevich Ivan Ivanovich, who helped me to embark on the path of science and made all this possible.

Vilniaus universiteto leidykla
Saulėtekio al. 9, III rūmai, LT-10222 Vilnius
El. p. info@leidykla.vu.lt, www.leidykla.vu.lt
bookshop.vu.lt, journals.vu.lt
Tiražas 20 egz.